



HAL
open science

Fluid circulation along an oceanic detachment fault: insights from fluid inclusions in silicified brecciated fault rocks (Mid-Atlantic Ridge at 13°20'N)

Anne Verlaguet, D. Bonnemains, C. Mével, J. Escartin, M. Andreani, F.
Bourdelle, M-C Boiron, V. Chavagnac

► To cite this version:

Anne Verlaguet, D. Bonnemains, C. Mével, J. Escartin, M. Andreani, et al.. Fluid circulation along an oceanic detachment fault: insights from fluid inclusions in silicified brecciated fault rocks (Mid-Atlantic Ridge at 13°20'N). *Geochemistry, Geophysics, Geosystems*, 2021, 22 (1), 10.1029/2020GC009235 . hal-03152490

HAL Id: hal-03152490

<https://hal.sorbonne-universite.fr/hal-03152490>

Submitted on 25 Feb 2021

HAL is a multi-disciplinary open access archive for the deposit and dissemination of scientific research documents, whether they are published or not. The documents may come from teaching and research institutions in France or abroad, or from public or private research centers.

L'archive ouverte pluridisciplinaire **HAL**, est destinée au dépôt et à la diffusion de documents scientifiques de niveau recherche, publiés ou non, émanant des établissements d'enseignement et de recherche français ou étrangers, des laboratoires publics ou privés.

1 **Fluid circulation along an oceanic detachment fault: insights from fluid**
2 **inclusions in silicified brecciated fault rocks (Mid-Atlantic Ridge at 13°20'N)**

3
4 A. Verlaquet^{1*}, D. Bonnemaïn², C. Mével², J. Escartín^{2,3}, M. Andreani⁴, F.
5 Bourdelle⁵, M-C. Boiron⁶, V. Chavagnac⁷

6
7 ¹ Sorbonne Université, CNRS-INSU, Institut des Sciences de la Terre, IStEP UMR 7193, F 75005 Paris,
8 France

9 ² Marine Geosciences Group, IPGP CNRS UMR 7154, Paris, France

10 ³ Laboratoire de Géologie, UMR 8538, Paris, France

11 ⁴ Laboratoire de Géologie, Université de Lyon, Lyon, France

12 ⁵ Univ. Lille, IMT Lille Douai, Univ. Artois, Yncrea Hauts-de-France, ULR 4515 - LGCgE,
13 Laboratoire de Génie Civil et géo-Environnement, F-59000 Lille, France

14 ⁶ Université de Lorraine, CNRS, GeoRessources, F-54000 Nancy, France

15 ⁷ Géosciences Environnement Toulouse (GET), Université Paul Sabatier Toulouse 3, CNRS UMR 5563,
16 IRD, Toulouse, France

17
18
19 * Corresponding author: anne.verlaquet@sorbonne-universite.fr

20
21
22 **Keypoints**

- 23 • MAR 13°20'N corrugated detachment fault is composed of pervasively silicified mafic
24 breccias overlated from hangingwall diabases
- 25 • Quartz fluid inclusions record mixing of hangingwall silica-rich brines with footwall
26 serpentinite-derived fluids (H₂+CH₄) in detachment
- 27 • This heterogeneous fluid circulation in shallow detachment fault is inconsistent with
28 models of detachments channeling deep fluid flow

30 **Abstract**

31 The MAR 13°20'N corrugated detachment fault is composed of pervasively silicified mafic
32 cataclastic breccias, instead of ultramafics and gabbros commonly found at other detachments.
33 These breccias record overplating of hangingwall diabases, with syntectonic silicification due to
34 important influx of silica-iron-rich fluids, able to leach alkalis and calcium. Fluids trapped in quartz
35 inclusions show important salinity variations (2.1-10 wt.% NaCl eq.) indicating supercritical phase
36 separation. Fluid inclusions also contain minor amounts of $H_2 \pm CO_2 \pm CH_4 \pm H_2S$, with high H_2/CO_2
37 and H_2/H_2S ratios, signatures typical of ultramafic-hosted vent fluids. We propose that seawater
38 infiltrated the hangingwall upper crust at the axis adjacent to the active detachment, reaching a
39 reaction zone at the dyke complex base (~2 km). At >500°C, fluids become Si-rich during diabase
40 alteration (amphibolite-facies alteration in clasts), and undergo phase-separation. Brines,
41 preferentially released in the nearby detachment fault during diabase brecciation, mix with
42 serpentinite-derived fluids bearing H_2 and CH_4 . Cooling during detachment deformation and fluid
43 upward migration triggers silica precipitation at greenschist-facies conditions (quartz+Fe-rich-
44 chlorite+pyrite). Important variations in fluid inclusion salinity and gas composition at both sample
45 and grain scales record heterogeneous fluid circulation at small spatial and short temporal scales.
46 This heterogeneous fluid circulation operating at <2 km depth, extending both along-axis and over
47 time, is inconsistent with models of fluids channeled along detachments from heat sources at the
48 base of the crust at the fault root. Present-day venting at detachment footwall, including Irinovskoe,
49 is instead likely underlain by fluid circulation within the footwall, with outflow crossing the
50 inactive detachment fault near-surface.

51

52 **Keywords**

53 MAR 13°20'N, silicified detachment, fluid inclusions, mafic breccias, phase separation,
54 hangingwall overplating

55

56

57

58

59 **Plain language summary**

60 Here we present constraints on fluid circulation along the 13°20'N oceanic detachment fault
61 along the Mid-Atlantic Ridge. Rocks recovered in situ with a deep-sea robot yield mafic breccias,
62 instead of serpentinized mantle rocks commonly found at other detachments. They likely originate
63 from the base of the hangingwall dyke complex, brecciated during fault exhumation. These rocks
64 are intensely silicified (quartz mineralization), resulting from upflow circulation of silica-rich
65 fluids derived from reactions with mafic rocks in a reaction zone. Fluid inclusion (micrometric
66 cavities in quartz crystals that trapped circulating fluid) analyses reveal highly-saline fluids likely
67 formed by phase separation, while traces of hydrogen and methane likely record serpentinization.
68 We thus propose that seawater infiltrated the crust down to a reaction zone at its base (2 km depth),
69 where it became silica-rich by rock hydrothermal alteration. Upon brecciation, these silica-rich
70 brines were released in the detachment where they mixed with fluids coming from footwall rock
71 alteration. Temperature and pressure drops during fluid upflow promoted intense quartz
72 crystallization. The active Irinovskoe hydrothermal site, sitting on the detachment fault ~5 km off-
73 axis, is unrelated to fluid circulation in the detachment plane, and likely linked to a heat source
74 within the footwall and directly below it.

75 **1. Introduction**

76 Low-angle detachment faults are common along slow- and ultra-slow spreading ridges, forming
77 primarily at ridge sections with reduced melt supply (Buck et al., 2005; Cannat et al., 2006; Escartín
78 et al., 2008; Tucholke et al., 2008). Rooting deep below the rift valley floor, detachments can
79 operate over long periods of time (up to a few Myrs), exhume deep-seated materials from the
80 oceanic lithosphere, and lead to the formation of oceanic core complexes (OCCs). OCCs are often
81 capped by a fault surface displaying corrugations parallel to spreading. Ridge sections hosting
82 OCCs tend to be associated with high seismicity rates relative to magma-rich, symmetrical ridge
83 sections, and often display active hydrothermal venting (Escartín et al., 2008; Son et al., 2014).
84 The microseismicity along the Northern Atlantic and the Southwest Indian Ridge detachments
85 (deMartin et al., 2007; Parnell-Turner et al., 2017; Tao et al., 2020) reaches sub-Moho depths
86 (between ~8 and ~13 km bsf). These results suggest that detachments are associated to a thick
87 lithosphere, and that brittle deformation may provide potential pathways for fluid circulation
88 reaching deep levels. Indeed, fault zone rocks from various OCCs along the MAR display evidence
89 for fluid-rock interactions coeval with deformation. In most cases, the fault zone is characterized
90 by deformed ultramafics and gabbros recrystallized into talcschists and amphibolites, respectively
91 (Boschi et al., 2006; Escartín et al., 2003, 2017; Karson et al., 2006; MacLeod et al., 2002; McCaig
92 et al., 2007; Schroeder & John, 2004). Moreover, active hydrothermal fields are often found on the
93 OCC surface, with hydrothermal circulation crosscutting pre-existing and/or inactive fault zones,
94 as observed at Rainbow (Andreani et al., 2014), Ashadze (Ondréas et al., 2012), Logatchev
95 (Petersen et al., 2009), Lost City (Fruh-Green et al., 2003) or Von Damm (Hogkinson et al., 2015).
96 To date, however, there is still limited information regarding fluid sources and pathways along the
97 detachment fault zone at depth, the location and nature of heat sources animating this hydrothermal
98 circulation, and the possible links between the hydrothermal activity observed at the surface of
99 these OCCs and the flow along the detachment.

100 The 13°20'N detachment fault, located on the western flank of the Mid-Atlantic Ridge (MAR),
101 exposes a structurally continuous and corrugated detachment fault surface (e.g, Escartín et al.,
102 2017; MacLeod et al., 2009; Smith et al., 2006). While morphology is similar to OCCs elsewhere
103 (Parnell-Turner et al., 2018), sampling of the detachment fault zone reveals unique characteristics.
104 Indeed, while other detachment faults are composed of deformed and hydrated footwall ultramafics
105 and gabbros (Boschi et al. 2006; Escartín et al., 2003, 2016; Karson et al., 2006; MacLeod et al.,

106 2002; McCaig et al., 2007; Schroeder & John, 2004), the well-preserved and corrugated 13°20'N
107 detachment fault zone is composed essentially of highly silicified mafic cataclastic breccias
108 (Bonnemains et al., 2017; Escartín et al., 2017). These silicified fault breccias likely result from
109 the overplating of mafic material from the base of the hangingwall dyke complex into the footwall
110 during fault exhumation (Bonnemains et al., 2017); these rock types have not been reported from
111 any other studied OCC. The silicified fault zone is ~70 m or thicker, and the mechanisms of strain
112 localization and fault development leading to a corrugated structure seem to operate independently
113 of lithologies within the fault zone (e.g., Parnell-Turner et al., 2018). Fault zone silicification is
114 evidenced by massive quartz precipitation that may result from elevated fluxes of silica-rich fluids,
115 possibly syntectonic (Bonnemains et al., 2017). This detachment fault surface also hosts the active
116 Irinovskoe hydrothermal site, where several black smokers discharge high temperature fluids
117 (Escartín et al., 2017; MacLeod et al., 2009).

118 The 13°20'N silicified fault rocks, and the fluid inclusions trapped in quartz crystals, provide a
119 unique opportunity to investigate the nature, sources and pathways of fluids circulating within an
120 active detachment fault zone, and to compare them to fluid circulation feeding the active footwall
121 Irinovskoe hydrothermal site. Indeed, to date geochemical and fluid inclusion studies have been
122 conducted on hydrothermally altered rocks from both hangingwall (e.g., Delaney et al., 1987;
123 Humphris et al., 1998; McCaig et al., 2007, 2010; Tivey et al., 1998; Vanko et al., 2004) and
124 footwall of detachments (e.g., Andreani et al., 2014; Boschi et al., 2006; Castelain et al., 2014).
125 However, in these either the link to detachment fault deformation is not established, or the
126 associated hydrothermal systems post-date detachment activity, as in active and inactive systems
127 preserved at the footwall of oceanic detachments (e.g., Andreani et al., 2014; Escartín et al., 2017;
128 Hodgkinson et al., 2015; Ondréas et al., 2012). Thus, studies addressing syntectonic fluid flow at
129 detachments are scarce, and rely on geochemical data from rock samples, (e.g., McCaig et al.,
130 2007, 2010), not from fluids.

131 To constrain fluid-rock interactions within an active detachment fault zone, here we present a
132 study of fluid inclusions trapped in quartz crystals from silicified fault rocks of the 13°20'N OCC.
133 A microthermometric study was conducted on >100 fluid inclusions from four representative fault
134 rock samples collected *in situ* at different outcrops throughout the 13°20'N fault zone, and with
135 varying degrees of silicification. Fluid inclusion composition was also investigated by Raman
136 spectroscopy. Whole-rock geochemical analyses were performed to constrain nature and

137 composition of the host rocks, and chlorite analyses to constrain the temperature of quartz-chlorite
138 crystallization. With these results and available geological constraints, we propose a model of
139 hydrothermal fluid circulation within an active oceanic detachment fault.

140

141 **2. Geological background of 13°20'N OCC and sampling**

142 **2.1. Geological setting**

143 The 13°20'N oceanic detachment displays a structurally continuous fault surface with prominent
144 extension-parallel corrugations, exposed at the seafloor, and that roots at the rift valley floor. This
145 OCC develops on the western flank of the MAR, which spreads at a full rate of 24.6 mm/yr
146 (MacLeod et al., 2009; Smith et al., 2008), and is likely active based on its morphology, the absence
147 of late tectonic disruption (Escartín et al., 2017; MacLeod et al., 2009; Mallows & Searle, 2012),
148 and seismic activity. Microseismicity defines a curved fault plane reaching >10 km below the ridge
149 axis (Parnell-Turner et al., 2017), reminiscent of that of other detachments such as TAG (deMartin
150 et al., 2007) or Longqi (Tao et al., 2020). This OCC and its detachment fault were extensively
151 investigated and sampled during the ODEMAR cruise, using deep-sea vehicles
152 (<http://www.doi.org/10.17600/13030070>). Main cruise results, geological context, details of fault
153 rocks are provided elsewhere (Escartín et al., 2017; Bonnemains et al., 2017).

154 The exposed, corrugated detachment fault extends ~7 km in the spreading direction (East-West),
155 and ~5.5 km perpendicular to the extension (North-South), respectively (Figure 1a; Olive et al.,
156 2019). The microbathymetric corrugations (Figure 1b) have a relief of up to ~10-20 m, and along-
157 extension lengths of a few hundred meters to a maximum of 2 km (Parnell-Turner et al., 2018).
158 While the detachment fault surface is heavily blanketed by sediment and rubble, fault planes crop
159 out on the flank of these corrugations, showing subhorizontal striations parallel to extension
160 (Escartín et al., 2017). During the ODEMAR cruise, in situ fault rocks were sampled at seven
161 outcrops distributed both along- and across-extension throughout the corrugated detachment fault
162 surface (see numbered circles in Figure 1b). Among these outcrops, Outcrop #1 (Figure 1b) was in
163 a ~70 m deep structural low within the detachment fault surface, which shows corrugations
164 throughout. From these observations it was inferred that the fault zone is composed of
165 anastomosing fault planes developing over a thickness of ~70 m or more (Bonnemains et al., 2017;
166 Escartín et al., 2017; Parnell-Turner et al., 2018).

167 The activity of the Irinovskoe hydrothermal field was confirmed during the ODEMAR cruise
168 (Escartín et al., 2017), ~1.8 km from the footwall cutoff (black circle in Figure 1b), at a location
169 where samples of sulfides indicated recent or active hydrothermalism (Cherkashev et al., 2013;
170 MacLeod et al., 2009; Pertsev et al., 2012). This site displays two black smoker vents at the summit
171 of hydrothermal mounds (Active Pot and Pinnacle Ridge) venting fluids at ~365°C, in addition to
172 several inactive mounds and chimneys (Escartín et al., 2017).

173

174 **2.2. Detachment fault rocks: lithology and silicification**

175 A total of 36 fault rocks were recovered in situ from the seven outcrops throughout the 13°20'N
176 corrugated detachment fault using ROV Victor 6000, and are described in detail by Bonnemains et
177 al. (2017). All the rocks are cataclastic breccias, with significant heterogeneity in clast abundance
178 and size, and clast/matrix ratios, even at sample-scale (Figure 2). Most breccias contain solely
179 mafic clasts (basalt/diabase; Figure 2a-d), and only 2 of the 36 samples display a mixed lithology,
180 with coexisting mafic and ultramafic clasts (see Figures 1b and 2e-f). Several fault rock samples
181 display highly localized deformation with striated slip plane surfaces (Figures 2c-e), as well as
182 complex internal deformation textures, with cataclastic slip zones. Textures record, at the sample
183 scale, several phases of both localized and distributed, penetrative deformation (Bonnemains et al.,
184 2017).

185 Fault rocks are variably silicified indicating that (1) silica-rich fluids percolated through the fault
186 rocks, and that (2) this silicification (and associated fluid flow) was likely heterogeneous at small
187 spatial (outcrop) scale (Bonnemains et al., 2017). Moderately silicified mafic samples are clast-
188 supported breccias, and contain clasts of hydrothermally altered mafic rocks with still identifiable
189 magmatic textures. Most clasts display a relatively coarse doleritic texture underlined by fresh
190 plagioclase laths (Figure 3b; see Bonnemains et al., 2017 for additional micrographs) indicating a
191 diabase protolith. We have identified a single sample with a clast showing vesicular texture,
192 corresponding to extrusive basalt (Figure 3a). Hence, the bulk of the fault material is incorporated
193 from a dyke complex (Bonnemains et al., 2017), with limited reworking of shallow basalts, and
194 consistent with an efficient exhumation (Olive et al., 2019).

195 The least silicified diabase clasts show rare relict clinopyroxene, largely replaced by amphibole
196 of hornblende composition, associated to fresh plagioclase of labradorite composition, and no

197 associated chlorite (detailed mineral compositions in Bonnemains et al., 2017). This secondary
198 mineral assemblage thus records hydrothermal recrystallization initiated under amphibolite facies
199 conditions (≥ 500 °C). With increasing silicification, amphibole in clasts turns to actinolite,
200 plagioclase becomes more albitic while chlorite crystallizes in clasts too, indicating greenschist
201 facies conditions (~ 300 °- 500 °C). Clasts in these low to moderately silicified samples are
202 surrounded by a matrix of finely crushed material, with newly formed chlorite and scattered quartz
203 grains (<10 vol.% quartz). Highly silicified mafic samples are matrix-supported breccias with
204 highly recrystallized clasts whose primary texture is largely obliterated. These breccia clasts are
205 made up almost exclusively of chlorite and quartz, and are surrounded by a quartz-dominated (>90
206 vol.% quartz) matrix that also contains chlorite. Of the two samples bearing ultramafic clasts, only
207 one has been silicified. Abundant sulfides associated with quartz are found in three silicified fault
208 rocks.

209 Cathodoluminescence imaging of selected samples also shows that quartz grains record
210 successive fracturing and recrystallization episodes (Bonnemains et al., 2017), thus consistent with
211 syntectonic quartz crystallization. Silicification and chloritization are closely associated during the
212 alteration of the $13^{\circ}20'N$ detachment fault mafic breccias. Indeed, chlorite is absent from the
213 freshest diabase clasts (Bonnemains et al., 2017), chlorite content is low in moderately silicified
214 samples and increases significantly with degree of silicification. Chlorite crystals imbricate quartz
215 ones, or are included within quartz crystals, demonstrating co-crystallization in both clasts and
216 matrix. Coeval quartz and chlorite crystallization is also unequivocal within late chlorite-filled
217 veins crosscutting mafic samples. Thus, these microtextures record coeval formation of both
218 minerals during detachment exhumation, and indicate that silicification occurred at greenschist-
219 facies conditions (Bonnemains et al., 2017).

220

221 **2.3. Samples selected for fluid inclusion and geochemical study**

222 This study is based on a set of 6 representative detachment fault rocks that have been selected
223 in order to (1) obtain a spatial coverage throughout the $13^{\circ}20'N$ corrugated surface, and (2) cover
224 various degrees of alteration and silicification (Table 1; Figure 1). These rocks were sampled in
225 situ from five fault surface outcrops that are described in detail by Bonnemains et al. (2017; Figure
226 1b). All silicified samples contain abundant albeit very small fluid inclusions in quartz crystals.

227 Fluid inclusions suitable for this study were identified in 4 samples: three variably silicified
228 breccias with only mafic clasts (ODM195, ODM155 and ODM218), and one silicified breccia with
229 mixed mafic-ultramafic clasts (ODM173). We benchmarked geochemical analyses with two
230 additional unsilicified samples of mafic and mixed mafic-ultramafic material (ODM115 and
231 ODM217, respectively). Sample texture and mineralogy are summarized in Table 1. These samples
232 are heterogeneous, showing a complex history with several deformation phases (Bonnemains et
233 al., 2017), thus subsamples were also taken in some cases at varying distances from slip surfaces,
234 as indicated below. Furthermore, to obtain representative whole-rock chemical analyses, larger
235 subsamples were taken for three samples (i.e., ODM218, ODM173 and ODM217), labeled wr
236 (whole rock) in Tables 2 and S1.

237 ODM115 is a basaltic clast from an unsilicified breccia (Figure 2a). It displays a typical pillow
238 lava microtexture, with skeletal olivine microphenocrysts, radiating dendritic plagioclase, very
239 fine-grained clinopyroxene crystals and vesicles (Figure 3a). Vesicles are filled with chlorite, veins
240 with epidote, and the ground mass contains chlorite and pumpellyite. This quartz-free clast of
241 extrusive basalt is considered as a reference for mafic material incorporated into the fault zone. It
242 is the sole unsilicified mafic sample recovered from the fault outcrops.

243 ODM195 is a moderately silicified clast-supported breccia (Figure 2b) with clasts composed of
244 either chlorite only, or actinolite + plagioclase ± chlorite displaying relict doleritic textures (Figure
245 3b). The matrix contains crushed sub-millimetric clast fragments surrounded by newly formed
246 chlorite and 5-10 vol.% of quartz (Figure 3b). Anhedral quartz crystals, typically ~100 µm in
247 length, are either scattered or in local aggregates in the matrix.

248 ODM155 and ODM218 are two highly silicified, matrix-supported fault breccias (Figures 2c-
249 d). Both display a striated surface (slip plane) and an underlying well-developed slip zone
250 (penetrative deformation). No primary mineral is preserved in any of the clasts, which contain
251 either chlorite + titanite or chlorite + quartz (Figures 3c-d). Rare clasts preserve a primary doleritic
252 texture (Figure 3c) despite pervasive alteration and mineral replacement, thus indicating a diabase
253 protolith. Anhedral and subhedral quartz grains surrounded by interstitial chlorite represent >90
254 vol.% of the matrix. Both samples contain abundant sulfides, ODM155 containing only pyrite,
255 whereas ODM218 contains pyrite with minor pyrrhotite and chalcopyrite.

256 Three subsamples were taken from ODM218, at varying distance from the slip surface, to
257 investigate relationships between sample geochemistry and distance to slip planes, which may act
258 as preferential fluid flow zones. ODM218a is located within 1 cm from the striated slip surface
259 (Figure 2d), and contains only rare and submillimetric sulfide grains and clasts embedded in a
260 quartz-rich matrix. When present, clasts are mostly silicified. ODM218b is ~4-5 cm away from the
261 slip plane, and displays clasts either silicified or quartz-free up to 1 cm in size, in addition to
262 disseminated quartz grains in the matrix. ODM218c is a fragment dislodged from the lower surface
263 of the sample and away (~12 cm) from the slip plane, and contains quartz-free clasts surrounded
264 by a silicified matrix with sulfides. In this set of samples, matrix quartz grain sizes increase with
265 the distance to the slip plane, and thus ODM218c contains the largest matrix quartz grains.

266 ODM217 is a quartz-free, brecciated talc-amphibole schist displaying a slip surface on one side
267 and several internal slip zones (Figure 2e). Clasts are either made up of talc and amphibole or
268 chlorite \pm titanite (Figure 3e). Matrix mineralogy varies among slip zones, and is made of talc,
269 serpentine or chlorite (Figure 3e), with disseminated spinels. To account for sample heterogeneity,
270 two subsamples were taken (Figure 2e). Subsample ODM217a is a chlorite-rich slip zone adjacent
271 to a striated slip surface, whereas subsample ODM217b is a talc-rich zone a few cm away from
272 this same slip surface. For whole-rock geochemical analyses, we thus consider the unsilicified
273 breccia ODM217 as a reference, as it contains both ultramafic and mafic clasts.

274 ODM173 is a matrix-supported breccia (Figure 2f) containing both mafic and ultramafic clasts,
275 made of talc or chlorite \pm titanite (Figure 3f). The matrix is made of chlorite and talc, with variable
276 amounts of quartz at the sample scale, and scattered spinel and sulfides (chalcopyrite + pyrite;
277 Figure 3f). As for ODM217, we selected two sub-samples to investigate this heterogeneity.
278 ODM173a displays few small clasts (< 1 mm) surrounded by a silicified matrix made of chlorite
279 and talc associated with anhedral quartz crystals (<60 vol.% quartz, Figure 3f), whereas clasts in
280 ODM173b are more abundant and larger (up to 1-2 cm), with only rare quartz grains and minor
281 chlorite in the matrix. Sulfides are more abundant in ODM173b than in ODM173a.

282

283 **3. Methods**

284 To investigate the composition of fluids circulating through the detachment fault zone, and that
285 are responsible for pervasive silicification, a study of fluid inclusions trapped in quartz crystals was

286 coupled to whole-rock and mineral geochemical analyses (major and trace element). Fluid
287 inclusion analyses included microthermometry, Raman spectroscopy, and LA-ICP-MS. We also
288 used SEM-cathodoluminescence to study the growth history of quartz crystals hosting fluid
289 inclusions. Microthermometric measurements of fluid inclusions determined isochoric
290 relationships that, coupled with geologically constrained pressure intervals, provided estimates of
291 fluid inclusion entrapment temperatures. These temperatures were then compared to silicification
292 temperatures inferred from the composition of chlorite co-crystallized with quartz, using the
293 geothermometer of Bourdelle et al. (2013).

294

295 **3.1. Whole-rock and mineral chemical analyses**

296 Whole rock chemical analyses were performed at the SARM-CRPG (Nancy, France). Major
297 elements were analyzed by inductively coupled plasma optical emission spectroscopy (ICP-OES)
298 after fusion with LiBO_3 and dissolution in HNO_3 . Trace elements were quantified by inductively
299 coupled plasma mass spectrometry (ICP-MS) following the procedure described by Carignan et al.
300 (2001). To account for sample heterogeneity, subsamples were analyzed for ODM218, ODM173
301 and ODM217 (see section 2.3).

302 Major element composition of chlorite was analyzed by EPMA (CAMECA SX-FIVE,
303 CAMPARIS, Sorbonne Université, Paris, France). Analytical conditions were 15 kV-10 nA in
304 WDS mode, for analysis of major elements. Fe_2O_3 (Fe), MnTiO_3 (Mn, Ti), diopside (Mg, Si), Cr_2O_3
305 (Cr), orthoclase (Al, K), anorthite (Ca) and albite (Na) were used as standards for elements in
306 parentheses. Only chlorite analysis with oxide sum in the 86-89 wt.% range and $\text{Na}_2\text{O} + \text{K}_2\text{O} +$
307 $\text{CaO} < 1$ wt.% were considered. Structural formulas were derived on a 14-oxygen basis. Chlorite
308 analyses with $\text{Si} \leq 4$ atoms per formula unit, cation sum ≤ 10.1 apfu and vacancies >0.01 pfu were
309 considered. In situ trace element analyses were carried out on 22 chlorites at GeoRessources
310 (Nancy, France) using LA-ICP-MS. Technical details can be found with results in Table S3.

311

312 **3.2. Fluid inclusion analyses**

313 Fluid inclusions analyses were performed on 100 μm thick double-polished sections. Successive
314 generations of fluid inclusions trapped during quartz crystal growth were first characterized using

315 an Olympus BX-50 transmitted light microscope at IPGP. Inclusions either isolated or clustered
316 (i.e., distant less than five times their length; Figure 4a) are considered as primary according to the
317 criteria of Roedder (1984) and Van den Kerkhof and Hein (2001), whereas those located along
318 trails crosscutting quartz grains are considered as secondary (Figure 4b). The location of the
319 different generations of fluid inclusions within individual quartz crystals was compared to crystal
320 growth history as revealed by SEM-cathodoluminescence observations (as in Boiron et al., 1992),
321 conducted at IStEP - Sorbonne Université (Paris, France) on a Scanning Electron Microscope Zeiss
322 Supra 55 equipped with an EDS system and an Oxford Instruments cathodoluminescence system.

323 Microthermometric fluid inclusion measurements were carried out at IStEP - Sorbonne
324 Université under an optical microscope equipped with a Linkam THMSG 600 heating-freezing
325 stage with temperatures ranging from -196 °C to +600 °C. The stage is controlled by a Linkam
326 TMS 93 programmer via LinkSys software v.2.15.

327 Cycles of repeated homogenization and ice melting temperature measurements were conducted
328 on 176 individual inclusions to measure the temperature of phase changes for the gas-to-liquid
329 homogenization (temperature of homogenization, T_h) and for the ice melting point (temperature of
330 final ice melting, $T_{m_{ice}}$), respectively. Several cycles performed to test reproducibility show that
331 ice melting and homogenization temperatures were reproducible within 0.1 °C (~0.2 wt.% eq.
332 NaCl) and 1 °C, respectively. Inclusions yielding non-reproducible measurements systematically
333 showed complex morphologies and were thus discarded, yielding 119 fluid inclusions for this
334 study. We performed temperature cycles in the potential range of hydrate melting temperatures,
335 following Raimbourg et al. (2014), but no gas hydrate was detected. Salinity was estimated from
336 $T_{m_{ice}}$ using the equation in Bodnar (1993), assuming that the entrapped fluid is a pure H₂O-NaCl
337 solution. Isochoric P-T relationships followed by fluid inclusions were derived from T_h and NaCl
338 molality, following the equation of Zhang and Frantz (1987), suitable for our P-T and salinity
339 range.

340 Gas content of fluid inclusions was analyzed with a Dilor-Labram Raman microspectrometer at
341 GeoRessources (Nancy, France) on a representative set of 83 inclusions. As all studied inclusions
342 are two-phase, we focused the laser on the gas bubble to determine gas proportions. In these
343 dominantly aqueous inclusions, H₂O vapor is by far the dominant gaseous phase. The relative molar
344 proportions of the remaining minor gases (H₂, CO₂, CH₄, H₂S) were calculated with accuracy better

345 than 5% (Pasteris et al., 1988) following the procedure described in Dubessy et al. (1989). This
346 involves band area integration at wavenumbers of each gas and gas specific volume, i.e., Raman
347 scattering cross-section for each gas and instrument efficiency at the specific wavenumbers
348 (Frezzotti et al., 2012). To subtract the air signal for N₂, we conducted blank analyses in the quartz
349 immediately adjacent to each inclusion.

350 Fluid inclusion chemical composition was analyzed on all inclusions larger than 8 μm (i.e., 24
351 inclusions) with a LA-ICP-MS at GeoRessources (Nancy, France; see technical details in Table
352 S3). We analyzed Na, K, Li, Mg, Fe, Mn, Cr, Co, Ni, and calculated absolute concentrations and
353 limits of detection following Leisen et al. (2012), using Na content derived from
354 microthermometric T_{m,ice} measurements (and calculated salinity) as internal standard. However,
355 due to the low signal intensity for most measured elements, it was impossible to calculate accurate
356 fluid inclusion element concentrations; these fluid inclusions were very small, with fluid released
357 after 1-2 laser shots, and contained low salinity fluids that are therefore very diluted in metallic
358 elements. While Na is likely the most concentrated cation, it was systematically difficult to detect
359 by LA-ICP-MS due to ionization problems.

360

361 **4. Results**

362 **4.1. Chemistry**

363 ***4.1.1. Whole rock analyses***

364 Major element compositions and selected trace element contents for samples described in
365 Section 2.3 are presented in Table 2 (see Table S1 for full trace element analysis). Chemical data
366 are compared with published data of mafic and ultramafic rocks recovered at the 13°20'N OCC
367 (Wilson et al., 2013), and at the 15°20'N Fracture Zone (Godard et al., 2008; Paulick et al., 2006),
368 although such comparison must be done with care as 13°20'N fault rocks are breccias, and differ
369 from those at other sites, as presented above.

370 The unsilicified basaltic fault rock clast fragment (ODM115) has a composition similar to that
371 of MAR basalts. In silicified mafic samples, the concentration of alkalis, Ca and Al (CaO in Figure
372 5a; Na₂O and Al₂O₃ in Figures S1a-b) decreases sharply with increasing Si content, with almost
373 complete depletion in the highly-silicified samples ODM155 and ODM218. Mg# for basaltic

374 ODM115 and moderately silicified diabase ODM195 are in the range of MAR basalt and diabase
375 values (Figure 5b). In contrast, Mg# clearly decreases in highly silicified samples ODM155 and
376 ODM218 (Mg# < 45). Mixed mafic-ultramafic breccias show compositions that are intermediate
377 between MAR mafic and ultramafic compositions, resulting from mafic and ultramafic material
378 mixed in variable amounts (Figures 5a-b and S1a-b). As in mafic samples, CaO, Na₂O and Al₂O₃
379 contents, as well as Mg#, are significantly lower in the silicified sample ODM173 compared to
380 unsilicified ODM217 (Figures 5a-b and S1a-b). Their SiO₂ content is higher than that of ultramafic
381 rocks for both the silicified ODM173 and the unsilicified ODM217, which is talc-rich.

382 Cr and Ni concentrations (Figure 5c) in most mafic samples are similar to those of MAR basalts
383 and diabases, with subsample ODM218b showing slightly higher contents in both Cr and Ni. For
384 the two samples with both mafic and ultramafic clasts, Cr and Ni contents are intermediate between
385 those of MAR mafic and ultramafic compositions, reflecting again their mixed lithologies. The
386 REE patterns (Figure S1c) for all mafic breccias are flat, as observed for MAR basalt and diabase
387 patterns (Wilson et al., 2013). While the unsilicified basaltic clast ODM115 displays REE-
388 normalized values consistent with those of MAR mafic rocks, REE concentrations progressively
389 decrease as silicification increases, but without any pattern modification, likely due to dilution by
390 quartz crystallization. The two mafic-ultramafic fault rocks display REE patterns between those of
391 mafic and ultramafic signatures, reflecting their mixed lithologies (Figure S1c).

392 Hence, bulk rock analyses reflect significant heterogeneity of breccia samples, controlled by
393 both the degree of silicification and the nature of the clasts. However, such analysis only reveals
394 relative elemental enrichment or depletion. We combine these chemical analyses to textural and
395 mineralogical observations to constrain effective mass transfer, and to determine if silicification
396 resulted from significant silica enrichment only, or was associated to efficient leaching of other
397 elements. Several arguments indicate massive silica influx rather than an important leaching: (1)
398 dilution effect observed for most trace elements (Figure S1c), (2) preferential preservation of initial
399 textures with well-defined clast borders, which would have been erased by massive leaching, (3)
400 the fact that the most silicified breccias are matrix supported (while less silicified ones are clast-
401 supported), and (4) the preferential crystallization of quartz in the matrix. However, calcium and
402 alkalis (and part of the aluminum) were almost completely leached from silicified mafic and mixed
403 mafic-ultramafic samples, and this important decrease with increasing silicification cannot be
404 explained solely by passive depletion due to quartz crystallization (grey arrows, Figures 5a and

405 S1a-b). Almost complete alkali leaching is also supported by mineralogical composition of all
406 mafic fault rocks from the seven outcrops (Bonnemains et al., 2017). Indeed, highly silicified
407 samples contain mainly chlorite and quartz, lacking mineral phases able to host alkalis (i.e., no
408 plagioclase or amphibole in highly silicified samples ODM218 and ODM155). The decrease in
409 Mg# for silicified samples (ODM155, ODM218 and ODM173) compared to unsilicified ones
410 likely reflects iron enrichment, as Mg# would be unaffected by quartz crystallization (Figure 5b).
411 This is supported by the growth of iron-rich sulfides, essentially pyrite, as confirmed by the low
412 Cu and Zn content (Table 2).

413

414 **4.1.2. Chlorite composition**

415 Microprobe analyses show that chlorites from both mafic and mixed mafic-ultramafic samples
416 contain 40-50 wt.% of FeO+MgO, 30-40 wt.% SiO₂ and 15-25 wt.% Al₂O₃ (Figure 6a). There is
417 no systematic difference in chlorite composition between clasts and matrix for each sample (Figure
418 6a). Chlorites in moderately silicified ODM195 show slightly lower FeO+MgO and higher SiO₂
419 contents than highly silicified ODM218, while chlorite composition of highly silicified ODM155
420 overlaps both samples.

421 Chlorites contain Si apfu in the range 2.7-3.5, Al apfu is 1.5-2.6 and Mg# between 43 and 85
422 (Table S2). While Si and Al contents are clearly anticorrelated for all chlorites, Si content and Mg#
423 are roughly correlated in each sample, although more scattered (Figure 6b). The unsilicified basalt
424 sample (ODM115) has chlorite compositions similar to those from MAR basalts (Alt et al., 1985;
425 Gillis & Thompson, 1993; Humphris & Thompson, 1978). Chlorite composition in moderately
426 silicified breccia (ODM195), in both clast and matrix, is comparable to that in diabases
427 (amphibolite facies; Castelain et al., 2014; Escartín et al., 2003; Figure 6b). For highly silicified
428 samples (ODM155 and ODM218), chlorites clearly have a lower Mg# compared to ODM195, with
429 a wider range (about 80-40), although most of them remain comparable to oceanic basalt chlorites
430 (Figure 6b). Increasing silicification is obviously associated with iron enrichment and silica
431 depletion in chlorites, a trend also observed by Saccocia and Gillis (1995) and Delaney et al. (1987)
432 in the MARK area, and by Castelain et al. (2014) in diabase chlorite-quartz veins at the footwall
433 of the Atlantis Massif detachment (Figure 6b). Indeed, iron-rich chlorites have been described in
434 oceanic hydrothermal breccias and quartz veins associated with the dyke complex or the dyke-lava

435 transition (Alt et al., 1985; Delaney et al., 1987; Honorez et al., 1998; Humphris et al., 1998; Mottl,
436 1983; Saccocia & Gillis, 1995).

437 Concerning mixed mafic-ultramafic breccias, chlorites from the unsilicified sample ODM217
438 show the highest Mg# at ~80. This is expected in rocks containing fragments of ultramafic rocks,
439 and are mostly comparable to chlorites from other oceanic detachment talcschists and amphibolite
440 schists (e.g., 15°45'N, Escartín et al., 2003; South Atlantis massif, Boschi et al., 2006; Figure 6b).
441 Mg# for chlorites in the silicified mixed breccia (ODM173) presents a broader range and lower
442 values (Mg#~50-80) than those of talcschists (Mg#~80, Figure 6b), similar to the decrease in Mg#
443 and Si with increasing silicification observed for mafic samples.

444 Concerning trace elements, chlorites from mixed mafic-ultramafic fault rocks are generally
445 enriched in Cr, Ni, Co, but depleted in Ti, V, Mn compared to chlorites from mafic breccias (Tables
446 S2 and S3), in line with literature data (e.g., chlorites from diabases and talcschists, Boschi et al.,
447 2006; Escartín et al., 2003). We note that a few chlorites from highly silicified mafic samples
448 (ODM155 and ODM218) also show enrichments in Cr, Co, and slight enrichments in Ni (Tables
449 S2 and S3).

450

451 ***4.1.3. Calculated temperature of chlorite formation***

452 Several chlorite thermometers exist in the literature, based on empirical, semi-empirical, or
453 thermodynamic approaches. Empirical thermometers cannot be used here as their application is
454 restricted to the chlorite compositional space used for their calibration (Bourdelle & Cathelineau,
455 2015). Furthermore, their applicability is questionable as they only consider one substitution, do
456 not take into account the bulk rock composition, and have no thermodynamic basis (Bourdelle &
457 Cathelineau, 2015). Thermobarometric models (e.g., Vidal & Parra, 2000; Vidal et al., 2001, 2005,
458 2006; Walshe, 1986), widely used in metamorphic environments, lack of thermodynamic data for
459 the Si-rich Al-free chlorite end-member (Figure 6c), therefore precluding their use for our samples.
460 Indeed, chlorites formed in the fault breccias (Figures 6b-c) have a relatively high Si content (2.7-
461 3.5 apfu) and some chlorites plot in the clinocllore-sudoite-Al-free chlorite field (Figure 6c). We
462 thus used the semi-empirical geothermometer of Bourdelle et al. (2013), suitable for all
463 compositions of chlorite in equilibrium with quartz. This choice is also comforted by the quartz

464 and chlorite co-crystallization in both matrix and clasts during silicification (see 2.2 and
465 Bonnemains et al., 2017).

466 The geothermometer of Bourdelle et al. (2013) is specifically calibrated for low-temperature
467 contexts (i.e., $T < 350$ °C), through a linear equation linking the chlorite + quartz equilibrium
468 constant to the temperature of crystallization, taking into account cationic substitutions involving
469 Si and R^{2+} contents. For higher-grade contexts, several thermodynamic parameters (as the non-
470 ideal contribution of the site mixing) cannot be linearized, and a quadratic correction (Bourdelle et
471 al., 2013) is proposed instead (“Tcorrected” in Table S2). While these “Tcorrected” results should
472 be cautiously considered (Bourdelle et al., 2013), this involves a small portion of our analyses.

473 Temperatures obtained with this thermometer mostly span the 150-400 °C range (except for a
474 few outliers which are not considered). We find median temperatures of ~250 °C for the moderately
475 silicified samples ODM173 and ODM195, and ~275 and ~300 °C for the highly silicified samples
476 ODM155 and ODM218 respectively (Figure 6d; Tables S2 and S4).

477

478 **4.2. Fluid inclusion results**

479 *4.2.1. Distribution and morphology of fluid inclusions*

480 Fluid inclusions are common in quartz from the 13°20'N detachment fault rocks. Those in quartz
481 crystals from clasts in highly silicified breccias are bigger and better preserved than those in quartz
482 grains within the matrix, which shows abundant decrepitated inclusions. All inclusions contain
483 aqueous fluid that is two-phase (liquid-vapor; Figure 4) at room temperature, with a vapor to total
484 volume ratio ranging from 0.1 to 0.5 (Figure S2). In quartz grains distant from slip planes (>1 cm),
485 fluid inclusions are abundant and mostly range in size from 8 to 12 μm (Figure 4a). The contour of
486 primary fluid inclusions is spherical to elongated, sometimes approaching negative crystal shapes
487 (Figures 4a, d, e, i). No sign of decrepitation (e.g., Roedder, 1984; Touret, 2001) is noticeable,
488 except in samples within ~1 cm from a slip plane (sample ODM218a), in which inclusions are
489 small (<5 μm), very irregular in shape, and often empty and probably decrepitated (e.g., Roedder,
490 1984). Inclusions in this sub-sample ODM218a were therefore discarded for microthermometric
491 measurements.

492 Small and elongated fluid inclusions, a few microns thick and a few tens of micron long, are
493 regularly distributed, defining trails. Their elongation is often slightly oblique to the trail direction
494 (Figures 4b, c, f, g, h), but their vapor ratio is similar to that of primary inclusions (Figure S2).
495 These correspond to recrystallized microfractures, and thus postdate primary ones described above
496 (e.g., Roedder, 1984). These trails do not show any distinct orientation, neither relative to each
497 other nor at the sample scale (Figures 4f, g). Most of them are intra-grain trails, as they remain
498 within the limits of quartz grains (Van den Kerkhof & Hein, 2001), with few occurrences
499 crosscutting grain boundaries (Figures 4f, g). These trails are thus related to quartz fracturing
500 between successive quartz crystallization episodes as revealed by SEM cathodoluminescence
501 (Figures 7 and S3; Bonnemains et al., 2017). Therefore, this second set of inclusions can be
502 classified as “pseudo-secondary”, following the criteria of Roedder (1984).

503

504 **4.2.2. Microthermometry**

505 Ice melting temperature ($T_{m_{ice}}$) measurements indicate that all inclusions, primary and
506 secondary, contain moderately saline aqueous fluids. $T_{m_{ice}}$ ranges from -6°C to -1.5°C (Figure
507 S4), yielding equivalent salinities ranging from 2.1 to ~ 10 wt.% eq. NaCl. Most fluid inclusions
508 studied here thus have a salinity higher than that of seawater (3.2 wt.% eq. NaCl, blue line in Figure
509 8a; Table 3) with salinity restricted to the 4–6 wt.% eq. NaCl range for all samples but ODM218,
510 which displays a wider salinity range (2.1–10 wt.% eq. NaCl). We note that the salinity is higher
511 for subsample ODM218b (from 6.3 to 10 wt.% eq. NaCl) than for subsample ODM218c (from 2.1
512 to 6.1 wt.% eq. NaCl; Figure 8a).

513 Highly silicified mafic breccias (ODM155, ODM218) present higher homogenization
514 temperatures (180–350 $^{\circ}\text{C}$) than moderately silicified ones, either mafic (ODM195) or mixed
515 mafic-ultramafic (ODM173; 150–220 $^{\circ}\text{C}$; Figure 8a; Table 3). The highly-silicified sample
516 ODM155 shows a wide range of T_h values, spreading over $\sim 130^{\circ}\text{C}$, whereas the T_h for all other
517 samples show more restricted ranges of up to 90 $^{\circ}\text{C}$. We do not observe any systematic difference
518 in $T_{m_{ice}}$ and T_h between primary and secondary fluid inclusions in any of the samples (Figure 8a).

519 Intra-grain variations of fluid inclusion T_h and salinities are shown in Figure 8b, where sets of
520 inclusions from different quartz grains are shown with different colors. The strong variation of T_h
521 and salinity observed respectively for ODM155 and subsamples OM218b and ODM218c (highly

522 silicified mafic breccias) is thus observed not only at the sample scale, but also at the quartz grain
523 scale (Figure 8b). SEM-cathodoluminescence observations reveal core-to-rim variations in quartz
524 luminescence (Figures 7 and S3) that record successive steps of quartz crystallization (Bonnemains
525 et al., 2017). The location of fluid inclusions displaying scattered microthermometric values on
526 cathodoluminescence images (Figure 7b, d and S3b, e) suggests that fluid inclusions were trapped
527 in quartz of varying luminescence, and thus during different quartz grain crystallization phases,
528 between successive quartz fracturing episodes.

529

530 *4.2.3. Composition of fluid inclusions*

531 Fluid inclusions from the 4 fault rock samples studied here are mostly aqueous (i.e., H₂O-NaCl),
532 as shown by the absence of gas hydrate detection. Raman spectroscopy analyses of the vapor phase
533 (i.e., gas bubble) of aqueous fluid inclusions detected minor amounts of H₂, CO₂, CH₄ and H₂S (in
534 addition to H₂O) in the highly silicified mafic breccias (ODM155 and ODM218; Table 3; Figure
535 9). Conversely, only H₂O vapor was detected in the moderately silicified samples ODM173 and
536 ODM195, although the high fluorescence observed during Raman analyzes for the latter could have
537 hidden small gas signal.

538 In sample ODM155, only two out of 17 fluid inclusions (Table 3) were not purely aqueous and
539 contained traces of CO₂. On the other hand, 15 out of 28 inclusions from subsample ODM218b,
540 and the 21 analyzed inclusions of ODM218c, contained traces of gases (other than H₂O), and
541 dominated by H₂ (up to 100 mol.% of the H₂-CO₂-CH₄-H₂S content in 18 inclusions) in addition
542 to variable proportions of CO₂ (up to 80 mol.% of the H₂-CO₂-CH₄-H₂S content), CH₄ (up to 12
543 mol.% of the H₂-CO₂-CH₄-H₂S content) and H₂S (up to 12 mol.% of the H₂-CO₂-CH₄-H₂S content,
544 in 4 inclusions from ODM218c; Figure 9a). All inclusions display very low H₂S/H₂ ratios (Figure
545 9b), similar to those measured in ultramafic-derived hydrothermal vent fluids (Fouquet et al.,
546 2010), while mafic hosted vents rather show high H₂S/H₂ ratios. We do not observe any correlation
547 between gas compositions and microthermometric data (Figure S5).

548 LA-ICP-MS analyses were performed on a set of 24 fluid inclusions, but their small size
549 precludes calculating reliable concentrations (see 3.2). K +/- Na and Li were detected in 10
550 inclusions, and associated to the presence of Cr +/- Ni, Co, Mn, Fe, Mg in 7 of them. Despite these
551 limitations due to inclusion sizes, inclusion fluids in the 13°20'N detachment fault rocks appear to

552 be very diluted fluids. They can thus be assimilated to fluids in the H₂O-NaCl system, and hence
553 their salinity can be estimated from the ice melting temperature (Bodnar, 1993).

554

555 **5. Interpretation and discussion**

556 **5.1. Pressure and temperature conditions of silicification**

557 ***5.1.1. Pressure range deduced from the geological context***

558 Silicification occurred in the detachment plane, affecting cataclastic breccias of mainly mafic
559 composition. Preserved doleritic textures in moderately silicified breccias indicate that these
560 diabase rocks were part of the base of Layer 2 (dyke complex) at the hangingwall, underlying the
561 rift valley floor, and mechanically accreted into the fault zone (Bonnemains et al., 2017).
562 Geophysical observations along slow-spreading ridges suggest that Layer 2 thickness may vary
563 between 1 and 2 km (see discussion in Bonnemains et al., 2017 and references therein), while a
564 recent seismic experiment in this study area reports a Layer 2A thickness on-axis of ~2 km (Simão
565 et al., 2020). Assuming a rift valley floor depth of ~3000 m, and considering seawater and crustal
566 rocks densities of 1025 and 3000 kg.m⁻³ respectively, the pressure ranges for the base of Layer 2
567 can be estimated to 600-890 bars for lithostatic pressure, and 400-500 bars for hydrostatic pressure.
568 Therefore, silicification and coeval fluid entrapment in quartz crystals in the detachment fault zone
569 necessarily took place between the base of Layer 2 (400-890 bars) and the seafloor (300 bars;
570 Figure 10).

571

572 ***5.1.2. Temperature of fluid inclusion trapping during silicification***

573 Fluid inclusion isochores derived from microthermometric data (equation of Zhang & Frantz,
574 1987) represent the P-T relationship along which fluid inclusions were trapped (Figure 10), while
575 the measured homogenization temperature T_h (Figure 8) indicates the rooting temperature of the
576 isochore on the liquid-vapor curve (from Sourirajan & Kennedy, 1962). Intersection of fluid
577 pressure ranges (see above) with isochores provides an estimate of the temperature range of
578 silicification and subsequent fluid entrapment in quartz crystals (Figure 10). For samples ODM195
579 and ODM173, temperatures of fluid entrapment are in the 160-280 °C range, while for highly
580 silicified samples ODM155 and ODM218, entrapment temperatures are in the 200-400 °C and 275-

581 425 °C ranges respectively (Figure 10). As these fluid inclusions were trapped at various stages of
582 quartz syntectonic crystallization (Figures 7 and S3), fluid entrapment temperatures do represent
583 the temperature interval over which silicification occurred.

584 Significant scatter in isochores for ODM155 reflect Th variability. Indeed, ODM155 (and to
585 a lesser extent ODM195) exhibits a broad range of homogenization temperatures (~130 °C) at both
586 sample- and grain-scale, associated to homogeneous salinities (4-6 wt.% eq. NaCl; Figure 8). This
587 pattern is typical of post-entrapment deformation of fluid inclusions (Roedder, 1984), and is
588 common in most hydrothermal systems (Delaney et al., 1987; Kelley et al., 1993; Petersen et al.,
589 1998). This result suggests that some inclusion cavities (and therefore fluid density) underwent
590 later re-equilibration during penetrative deformation phases (i.e., slip zones and planes in both
591 samples), slightly modifying P-T isochoric relationships (Diamond et al., 2010; Tarantola et al.,
592 2010; 2012; Vityk & Bodnar, 1995). In contrast, ODM218 shows a very restricted Th range, thus
593 the isochore fan rather reflects its high variation in salinity (2-10 wt.% NaCl, Figure 8) and thus in
594 fluid density.

595

596 *5.1.3. Comparison with the temperature of chlorite formation*

597 The formation temperature of chlorite, which coevally crystallized with quartz in both matrix
598 and clasts during silicification (see 2.2 and Bonnemains et al., 2017), is calculated from chlorite
599 composition (see 4.1.3; Figure 6d; Tables S2 and S4), and is thus an independent estimate of
600 silicification temperature. The large range of chlorite crystallization temperatures (~150-400 °C,
601 Figure 6d) reflects continuous crystallization with quartz during breccia infiltration by
602 hydrothermal fluids and exhumation towards progressively lower P-T conditions in the detachment
603 plane. The temperature range of chlorite formation is coherent with the estimated trapping
604 temperatures for fluid inclusions, intersecting in all cases the isochores at realistic pressures (Figure
605 10). Interestingly, the chlorite temperature range intersects the isochores at higher pressures,
606 corresponding to lithostatic fluid pressures, for the moderately silicified samples (ODM173 in
607 particular), than for highly silicified samples (ODM218 in particular) for which the median chlorite
608 temperatures intersect the isochores at hydrostatic fluid pressures instead. Near hydrostatic fluid
609 pressures are coherent with the significant fluid amount required to explain pervasive silicification,
610 thus associated with an open system. In contrast, moderately silicified samples submitted to more

611 restricted fluid circulation may instead correspond to a system only transiently open. Silicification
612 is both static and linked to deformation episodes, as demonstrated by successive steps of quartz
613 growth-hydrofracturing-overgrowth (Figures 7 and S3). This complex system witnessed both
614 spatial and temporal fluid pressure variations, bounded by end-member lithostatic to hydrostatic
615 pressures, and linked to variations in rock permeability and fault zone connectivity, likely
616 modulated by both silica sealing and hydrofracturing episodes (Bonnemains et al., 2017).

617 We thus interpret this silicification as a long-lived, complex process along the detachment
618 plane during exhumation of the hangingwall-derived breccias (Bonnemains et al., 2017), consistent
619 with the large temperature ranges of both chlorite crystallization and fluid entrapment in quartz.
620 We also infer that silicification occurred mostly in the temperature range $\sim 200 - 400$ °C, the highest
621 temperatures corresponding to the highly silicified sample spanning the largest salinity variations
622 (2-10 wt.% NaCl, ODM218).

623

624 **5.2. Fluid compositions and potential fluid sources**

625 ***5.2.1. Insights from fluid inclusion salinity: phase separation***

626 Fluid inclusions contain an aqueous fluid with salinities generally higher than that of seawater.
627 Fluid inclusions from most samples (ODM155, ODM195, ODM173) present restricted salinity
628 ranges (4-6 wt.% eq. NaCl) corresponding to ~ 115 to 170% of seawater salinity (3.2 wt.% eq.
629 NaCl). This range is comparable to ranges of salinity (and Th) measured in fluid inclusions (Figure
630 8a) in rocks associated with hydrothermal fields both of mafic (TAG: Petersen et al., 1998; MARK:
631 Delaney et al., 1987; Saccocia & Gillis, 1995) and ultramafic nature (Rainbow, Logatchev,
632 Ashadze, Semenov, Irinovskoe; Bortnikov et al., 2011, 2014, 2015; Simonov et al., 2015). Fluid
633 inclusions from the highly silicified sample ODM218 display a large salinity range (2.1 to 10 wt.%
634 eq. NaCl, Figure 8a). At the grain scale, core-to-rim salinity variations are associated to
635 luminescence variations (Figures 7b, d, S3b, e and 8b) but do not show any systematic pattern,
636 rather suggesting that the fault zone witnessed pulses of fluids with variable salinity during
637 deformation.

638 Salinity in fluid inclusions from subsample ODM218b reaches up to 3 times seawater salinity
639 (i.e., 10 wt.% equiv. NaCl, Figure 8a). Similar values are also reported for MARK silicified
640 breccias (Delaney et al., 1987). In contrast, many fluid inclusions of subsample ODM218c cluster

641 at seawater-like salinities, while others in the same sample have salinities below that of seawater
642 (2.1 wt.% eq. NaCl, Figure 8a), as reported from TAG (Petersen et al., 1998). At least three
643 mechanisms have been proposed to explain salinities of fluid inclusions differing from that of
644 seawater: hydration reactions, chloride retention in secondary minerals, and phase separation:

645 (1) Hydration reactions consume water and, consequently, residual fluids may be enriched in
646 dissolved elements. These reactions increase salinity modestly, with +15% for basalt-seawater
647 equilibration at 350 °C (Wetzel & Shock, 2000), therefore clearly insufficient to explain the high
648 salinities recorded in sample ODM218b. This process is only efficient at low water-rock ratio
649 conditions and closed systems (Delaney et al., 1987). However, important fluid fluxes are required
650 to attain the observed high levels of silicification (up to ~90 vol.% quartz) in these matrix-supported
651 breccias (see 5.2.2). This precludes that hydration reactions alone may significantly change
652 salinities to values consistent with those observed here (Figure 8a).

653 (2) Chloride storage in transient phases (such as amphiboles, up to 4 wt.% chlorine; Vanko,
654 1988) can also modulate the salinity of the circulating hydrothermal fluids (Kelley & Robinson,
655 1990; Kelley et al., 1992). At 13°20'N OCC, hydrothermal amphiboles formed under amphibolite
656 facies conditions (i.e., in clasts, pre-dating silicification) are progressively replaced by chlorite
657 during silicification at lower temperatures (greenschist facies), and could therefore increase fluid
658 salinity. However, the low chloride content of these amphiboles (<0.29 wt.%; Bonnemains et al.,
659 2017) suggests that dissolution of these phases during silicification cannot account by itself for
660 salinities of fluid inclusions within mafic fault breccias, which are three times higher than those of
661 seawater.

662 (3) The only efficient mechanism to generate both high and low salinity fluids is the formation
663 of brine and vapor phases by supercritical phase separation of either seawater or magmatic fluids,
664 as invoked for high-temperature hydrothermal systems (e.g., Alt et al., 2010; Castelain et al., 2014;
665 Delaney et al., 1987; Kelley & Delaney 1987; Kelley et al., 1992; Vanko, 1988). At the 13°20'N
666 detachment fault, the minimum temperature for supercritical phase separation at the seafloor
667 (~3000 m, 300 bars, see 5.1) is ~400 °C (Figure 11), and would form high salinity brines and a
668 vapor phase. However, we do not have any direct evidence for in-situ phase separation during
669 silicification as we lack fluid inclusions with pure brines (up to ~40-50 wt.% eq. NaCl), as observed
670 in diabbases (Kelley & Delaney, 1987) or trondhjemite (Castelain et al., 2014; Figure 8a), or

671 inclusions with pure vapor phase (vapor to total volume of 0.1-0.5 in our study). This suggests that
672 phase separation occurred earlier, at deeper levels. Vapor and brine were likely segregated and
673 migrated upwards separately, similarly to the two-stage model proposed by Delaney et al. (1987)
674 for the MARK hydrothermal field. The wide range of salinities (i.e., from lower- to three times
675 higher-than-seawater) reported in 13°20'N silicified fault rocks may be accounted for by either re-
676 homogenization of variable amounts of brines and vapor phases once released in the detachment
677 fault (in the one-phase field, Figure 11), or their mixing with fluids of different salinity, prior to
678 fluid entrapment in quartz.

679 Although we have no direct constraints, we hypothesize that phase separation may have
680 occurred in the brecciation zone or its immediate vicinity. Indeed, most of the breccia clasts from
681 13°20'N fault zone are originally diabase, suggesting that they were initially part of the
682 hangingwall dyke complex adjacent to the detachment fault (see 2.2 and 5.1 and Bonnemains et
683 al., 2017). With a fully developed amphibolite facies paragenesis (hornblende + labradorite), these
684 rocks experienced hydrothermal alteration at temperatures higher than 500 °C (see review in Alt,
685 1995), likely at the base of the upper crust (root of the dyke complex), therefore acting as a reaction
686 zone. Fluid pressures in this reaction zone may be between hydrostatic and lithostatic, even close
687 to hydrostatic for high fluid fluxes. Figure 11 shows that cold seawater infiltrating the hangingwall
688 towards the base of the crust would undergo phase separation between 440 °C and 570 °C,
689 depending on the fluid pressure gradient. It is thus plausible that phase separation occurred in the
690 reaction zone where brecciation is inferred to take place (e.g., Bonnemains et al., 2017). Diabase
691 brecciation along the detachment fault zone may even enhance phase separation, promoting sudden
692 fluid pressure drops leading to the crossing of the liquid-vapor curve (Figure 11).

693

694 ***5.2.2. Insights from bulk-rock and chlorite compositions: a mafic-rock derived fluid***

695 Textural and mineralogical observations, coupled to bulk-rock analyses, document that diabase
696 breccias underwent variable silicification during exhumation within the detachment zone (see
697 4.1.1), reaching up to ~90 vol.% of quartz in matrix-supported breccias (Figure 5; Tables 2 and
698 S1). Such degrees of silicification require both circulation of a silica-rich fluid and high fluid-rock
699 ratios along the detachment fault zone. Indeed, experiments suggest that water-rock ratios >50 are
700 required for basalt replacement by quartz-chlorite assemblages at 300 °C (Mottl, 1983). Elevated

701 fluid fluxes are also supported by the enhanced leaching of alkalis and calcium (Figures 5a and
702 S1a-b) from diabase clasts with increasing silicification (Bach et al., 2013; Cann, 1969).

703 Chlorite crystallization in both clasts and matrix is associated to silicification, as showed by
704 chlorite and quartz co-crystallization textures, increasing amount of chlorite with silicification, and
705 similar chlorite composition in both clasts and matrix (Figure 6a). The decrease of bulk-rock and
706 chlorite Mg# with increasing silicification (Figures 5b and 6b), correlated to pyrite crystallization
707 in the highly silicified breccias, suggests interaction with iron-rich fluids. The association iron-rich
708 chlorites, quartz and pyrite has been observed in silicified oceanic hydrothermal breccias associated
709 with mafic-rock hosted vents such as TAG (Alt et al., 1985; Honnorez et al., 1998; Humphris et
710 al., 1998) or at the MARK area (Delaney et al., 1987; Saccocia & Gillis, 1995). For Saccocia and
711 Gillis (1995), these minerals result from interactions with high salinity, silica- and iron-rich fluids,
712 depleted in H₂S. This is in agreement with the high salinity (Figure 8) and low H₂S content (only
713 recorded in 4 fluid inclusions from ODM218, Figure 9a) in our fluid inclusions. Hence, almost all
714 H₂S was likely stored into pyrite, leading to iron-enriched fluids from which Fe-rich chlorites
715 crystallized (type I breccias from Saccocia & Gillis, 1995). A low H₂S content in fluids is also
716 consistent with the small amount of metallic trace elements recorded in our fluid inclusions (i.e.,
717 diluted fluids, see 4.2.3). Such fluid composition is characteristic of highly evolved hydrothermal
718 fluids sampled in upflow zones of hydrothermal cells, and recording mafic rock-hosted reaction
719 zones (Bach et al., 2013; Saccocia & Gillis, 1995).

720 The significant amounts of silica precipitated in detachment fault breccias also suggest the
721 leaching of a deep mafic source. Indeed, high-temperature hydrothermal fluids from the reaction
722 zone at the base of the mafic upper crust may be quartz-saturated (or close to) according to Wetzel
723 and Shock (2000; ~20 mmolal of aqueous silica at 400°C for seawater-basalt equilibrium). This is
724 in agreement with fluid composition from basalt-hosted hydrothermal vents at >300 °C (Fouquet
725 et al., 2010; Schmidt et al., 2011; McDermott et al., 2018). Fluids circulating upwards along the
726 detachment fault zone may witness both a significant temperature reduction (to 200-300 °C) and
727 pressure drops, promoting fluid supersaturation and quartz precipitation. On the contrary,
728 hydrothermal fluids equilibrated with peridotite should be largely undersaturated with respect to
729 quartz (0.5 mmolal of aqueous silica at 400°, Wetzel & Shock, 2000), and vent fluids from
730 ultramafic-hosted hydrothermal systems generally record 6-8 mmol/L of aqueous silica (Fouquet,
731 2010). Under these conditions, a temperature drop of 200 °C will not be sufficient to trigger quartz

732 crystallization. Hence, silica may only be provided by fluids reacting with mafic rocks. Moreover,
733 the high amount of silica crystallized in the breccia matrix (up to 90 vol% of quartz) requires
734 circulation of extremely Si-rich fluids: phase separation and brine formation in the reaction zone
735 may have enhanced aqueous silica concentration, as quartz solubility is about one order of
736 magnitude higher in NaCl-rich brines than in pure H₂O (Scheuermann et al., 2018; Schmidt et al.,
737 2011; Steele-MacInnis et al., 2011), promoting efficient silica transport towards the upflow zone
738 along the detachment fault.

739 Therefore, significant amounts of highly evolved hydrothermal fluids from a reaction zone at
740 the base of the hangingwall dyke complex flowed up along the detachment fault zone, transporting
741 leached aqueous silica. This syntectonic circulation resulted in intense and pervasive silicification
742 of mafic detachment fault breccias (with crystallization of Fe-rich chlorite and pyrite).

743

744 ***5.2.3. Insights from fluid inclusion gas content: mix with an ultramafic-derived fluid***

745 While most fluid inclusions are purely aqueous (H₂O-NaCl), some contain small amounts of H₂,
746 CO₂, CH₄, and minor amounts of H₂S (i.e., ODM218b and ODM218c; Figure 9; Table 3) in
747 addition to dominant H₂O (H₂O-NaCl-H₂±CO₂±CH₄±H₂S). Seawater phase separation cannot
748 produce all these gases, and other fluid sources are required. Among these minor gases, H₂ is by
749 far the most abundant in the inclusions (Figure 9; Table 3). H₂ is likely produced during
750 serpentinization reactions by oxidation of the iron contained in olivine, reactions that preferentially
751 occur between 200 and 350 °C (Martin & Fyfe, 1970; McCollom & Bach, 2009; Seyfried et al.,
752 2007). At high temperatures (>400 °C), H₂ may also be produced in mafic rocks by pyroxene
753 alteration (Allen & Seyfried, 2003; Foustoukos & Seyfried, 2005). CO₂ can be either linked to
754 seawater, or to a magmatic source enriching nearby fluids. CH₄ likely results from CO₂-rich fluids
755 reacting with H₂. This reaction may occur either during serpentinization, from hydrothermal
756 circulation in ultramafic rocks enriching fluids in both hydrogen and methane (Berndt et al., 1996;
757 Boulart et al., 2013; Charlou et al., 1998, 2002; Holm & Charlou, 2001; Monnin et al., 2014; Wetzell
758 & Shock, 2000), in H₂-rich fluid inclusions hosted in footwall magmatic rocks (e.g., Klein et al.,
759 2019; McDermott et al., 2015), or at a later time (e.g., during transport), but in any case, prior to
760 fluid entrapment during silicification.

761 To discriminate the origin of fluids that circulated along the detachment fault zone, we compare
762 the ratios of H₂, CO₂, CH₄, H₂S in our fluid inclusions to those analyzed in vent fluids (from MAR
763 mainly). While few inclusions present a CO₂-dominant gas content comparable to basalt-hosted
764 vent fluids, most of these inclusions show high H₂/CO₂ and H₂/CH₄ ratios (Figure 9a) and very low
765 H₂S/H₂ ratios (Figure 9b), signatures typical of ultramafic-hosted vent fluids (e.g., Rainbow,
766 Logatchev, Semenov, Irinovskoe; Destringeville et al., 2015; Fouquet et al., 2010; Schmidt et al.,
767 2011), and of hydrothermal alteration of ultramafic rocks (i.e., serpentinization < 400 °C, Wetzell
768 & Shock, 2000). However, fluids from the Piccard vents at the ultraslow spreading Cayman ridge
769 show anomalously high H₂ contents and H₂/H₂S ratios, for mafic-rock-derived vents (McDermott
770 et al., 2018). These fluids are interpreted as resulting from basalt alteration in a reaction zone at
771 very high temperature (>500°C) and high fluid/rock ratios (McDermott et al., 2018; Scheuermann
772 et al., 2018). This suggests that the high H₂/H₂S ratios analyzed in our fluid inclusions could derive
773 from the hangingwall reaction zone. Lacking experimental data on basalt alteration at >500°C,
774 reactions able to release such high H₂ amounts remain unknown. The reaction invoked by
775 Scheuermann et al. (2020), of amphibole destabilization to magnetite and quartz, is clearly
776 incompatible with our rocks, as hornblende is fresh in the least altered clasts (Bonnemains et al.,
777 2017), and no magnetite (neither quartz) was observed. Moreover, H₂/H₂S ratios in Piccard vent
778 fluids remain lower than those measured in most of our fluid inclusions (Figure 9b), although there
779 is no reason for different partitioning of H₂ and H₂S between brines and vapor phases after phase
780 separation (McDermott et al., 2018; Scheuermann et al., 2020). Therefore, H₂ production in the
781 reaction zone seems to be possible, but may not account for the elevated H₂/H₂S ratios analyzed in
782 our fluid inclusions, which are best explained by H₂ derived from ultramafic-rock serpentinization.
783 Contribution of ultramafic-derived fluids is further supported by slight Cr and Ni enrichments of
784 both sample ODM218b (Figure 5c) and some chlorites from highly silicified mafic breccias (Tables
785 S2 and S3; Angiboust et al., 2014; Boutoux et al., 2014; Locatelli et al., 2019 ; Spandler et al.,
786 2011).

787 While the hangingwall sampled by the fault zone likely extends only to the base of the dyke
788 complex, the footwall below the fault zone and deep sections of the hangingwall likely contain
789 mantle peridotites that witnessed fluid circulation. This is demonstrated by the occurrence of mixed
790 breccias containing altered ultramafic clasts (Bonnemains et al., 2017), and the outcropping of
791 ultramafic rocks throughout the area (Escartin et al., 2017; MacLeod et al., 2011). During

792 exhumation, peridotites likely interacted with seawater-derived fluids, and progressively
793 serpentinized. Fluids may have been subsequently channelized into and along the detachment fault
794 zone. Mixing of such seawater-salinity fluids with silica-rich brines and vapor phases (prior to
795 entrapment) could account for the wide salinity range observed in trapped fluids from the silicified
796 breccias (Figure 8). This contribution of serpentinization fluids must remain limited nonetheless,
797 as the absolute gas amounts trapped in fluid inclusions are extremely low. We also note that two
798 thirds of the analyzed fluid inclusions from ODM218 have a gas signature very close to that
799 analyzed for Irinovskoe vent fluids (Figure 9a), and that present-day fluid circulation within the
800 footwall may record similar fluid-peridotite reactions at depth, even though these fluids do not
801 exploit the detachment fault as a flow channel.

802

803 **5.3. Detachment faulting, potential heat sources at the ridge axis and scenario for fluid** 804 **pathways**

805 Our results suggest that silicification was linked to flow along the detachment fault zone of
806 silica-rich brines and minor vapor phases likely mainly formed in the hangingwall reaction zone
807 (Figure 12a). Such a reaction zone at the base of the upper crust requires a heat source, such as a
808 magma chamber at deeper levels and nearby the fault, or an along-axis dyke propagation
809 (Bonnemains et al., 2017; MacLeod et al., 2009). The conceptual model in Figure 12a builds on
810 the detachment fault zone structure suggested by Bonnemains et al. (2017) and Parnell-Turner et
811 al. (2018). This model includes a) the incorporation of mafic clasts from the hangingwall upper
812 crust into the detachment fault zone, from its base to the near-surface (brown stars in Figure 12),
813 b) a thickening of the fault zone during exhumation, and c) an anastomosed fault zone mixing
814 footwall-derived ultramafic material with dominant mafic material from the hangingwall. This
815 model is also consistent with recent 3D seismic experiments revealing elevated seismic velocities
816 at the footwall, both along the exposed detachment fault, and below its continuation eastwards
817 below the rift valley floor (Simão et al., 2020). Elevated footwall seismic velocities are consistent
818 with a lithosphere composed of lower crust and upper mantle rocks, juxtaposed to mafic rocks
819 across the detachment (Simão et al., 2020).

820 As illustrated in Figure 12b, we propose that seawater percolates downwards through the
821 hangingwall crust, reaching a reaction zone at temperatures >500 °C, at or near the axial zone.

822 High-temperature fluids circulating into the reaction zone may hydrothermally alter surrounding
823 mafic rocks, while releasing aqueous silica and potentially small amounts of H₂S in the fluid phase
824 (e.g., Bach et al., 2013; Wetzel & Shock, 2000). At these P-T conditions, phase separation occurs
825 and forms high-salinity brines and low-salinity vapor phases. The small number of inclusions
826 recording lower-than-seawater salinity (Figure 8a) suggests that only limited amounts of vapor
827 reached and circulated within the detachment zone, while most of these low-density vapor phases
828 may have migrated upwards through the hangingwall crust (Figures 11 and 12). Denser, less
829 buoyant brines may be stored at depth in crustal porosity, within diabase units (Fontaine &
830 Wilcock, 2006; Fontaine et al., 2007). Brines may be released into the detachment fault zone upon
831 diabase brecciation, together with minor amounts of vapor phases, locally produced H₂S, and
832 potentially CO₂ either transported by seawater or exsolved from the magma lens. Diabase
833 brecciation may enhance phase separation by causing sudden and local fluid pressure drops (Figure
834 11). In turn, fluid phase separation may also promote local overpressures that may favor brecciation
835 along the fault (André-Mayer et al., 2002; Bertelli & Baker, 2010), with possible links to seismicity
836 along the detachment.

837 Varying gas content and wide salinity ranges of trapped fluids point to a complex and dynamic
838 system. During silicification of the fault zone, upwelling silica-rich brines and minor vapors mixed
839 in variable amounts with H₂(± CH₄)-rich fluids derived from serpentinization of ultramafic material
840 from the footwall (Figures 11 and 12; Andreani et al., 2014; McCaig et al., 2010; McCaig & Harris,
841 2012). These fluids homogenized as a single fluid phase before trapping (one-phase fluid field,
842 Figure 11). Fluid fluxes from these different sources were likely variable both in time and within
843 the fault zone, resulting in strong variability of both gas content and salinity of fluid inclusions
844 (Figures 8 and 9). Significant variations of inclusion fluid composition at quartz grain scale
845 (Figures 7b, d, S3b, e and 8b) clearly indicate that the fluids circulating along the detachment were
846 inherently heterogeneous at small spatial scales and short temporal scales. Yet there is no evidence
847 for any systematic long-term evolution in fluid sources or fluid mixing processes during
848 silicification (i.e., similarity in primary and secondary fluid inclusion salinity ranges). Moreover,
849 the wide distribution of samples along axis and the pervasively silicified fault zone also indicate
850 that this heterogeneous flow was maintained over long-periods of time, and was sampled by the
851 detachment fault along most of its along-axis length.

852 All these fluids were preferentially channelized within the permeable fault zone, and silica
853 precipitation was likely triggered by a combination of temperature decrease, pressure drops, and
854 mixing of silica-rich brines with less-salted fluids. Both chlorite and fluid inclusion temperatures
855 (Figures 10 and 11) are lower than those measured at the base of the dyke complex elsewhere (Hole
856 1256; Alt et al., 2010), documenting a significant temperature drop and silicification occurring
857 under greenschist facies conditions. Upflow silica-rich brines were likely cooled either
858 continuously or episodically, during transient circulation in a complex, anastomosing fault zone,
859 and coeval with deformation leading to quartz fracturing-sealing episodes (i.e., fluid pressure
860 varying between hydrostatic and lithostatic; Figures 7 and 10), but also by fluid mixing with cooler
861 fluids from the footwall serpentinization and potentially seawater percolating from the seafloor.

862 **5.4. Fluids trapped in detachment fault rocks vs. seafloor hydrothermal venting**

863 Models of fluid flow and detachment faulting often assume a permeable fault zone efficiently
864 channeling fluids to the seafloor or the shallow crust (e.g., Andersen et al., 2014; McCaig & Harris,
865 2012; Tao et al., 2020). In these models, fluid flow through the detachment fault feeds hydrothermal
866 systems found both at the footwall (e.g., Logatchev; Andersen et al., 2014; Longqi: Tao et al.,
867 2020) and hangingwall (TAG; McCaig & Harris, 2012). The heat source animating this circulation
868 is often located in the upper mantle, at the base of the detachment microseismicity.

869 Our data and results from the 13°20'N detachment are not consistent with these deep-rooted
870 hydrothermal systems along detachment fault zones. First, the present-day Irinovskoe
871 hydrothermal site is located on the striated surface. As the detachment fault emerges at <20° at the
872 hangingwall cutoff and the detachment is capped by a highly fractured and deformed fault zone
873 (e.g., Escartín et al., 2017; Parnell-Turner et al., 2018), no plausible mechanism can channel fluids
874 from the active detachment fault zone below the rift valley floor (below the hangingwall cutoff) to
875 the Irinovskoe site, over a horizontal distance of ~2 km. The footwall also displays both a high-
876 velocity seismic anomaly underlying Irinovskoe, restricted to the shallower 2 km, and a broad low
877 velocity zone at 7-10 km depth (Simão et al., 2020). Owing to seismic resolution limitations, the
878 presence of magma chambers or heat sources of sizes below the seismic resolution (1 to 3 km in
879 size, depending on the depth) cannot be excluded. We propose that the fluid circulation system
880 underlying Irinovskoe is unrelated to the active detachment, and instead is fully hosted within the
881 footwall, probably reaching depths >2 km. While we lack direct seismic evidence here, this model

882 is similar to that of Rainbow, a hydrothermal field at the top of a detachment massif that is underlain
883 by seismic reflectors identified as active and fossil magma chambers at depths >3 km (Canales et
884 al., 2017; Dunn et al., 2017).

885 Silicified fault rocks are distributed throughout the detachment, displaying similar fluid
886 compositions in quartz inclusions. This observation points to a flow organization along the
887 detachment that has not been recognized before. Geological observations demonstrate that
888 syntectonic silicification and associated fluid circulation occurred along the whole length (along-
889 axis, Figure 1) of the active detachment, and that it operated continuously over time (across-axis;
890 Bonnemains et al., 2017). Fluid inclusions further indicate that similar fluid sources (similar
891 primary and secondary inclusions) mixed within the detachment plane (see 5.2.1 and Figure 8a).
892 This type of distributed and pervasive hydrothermal circulation, extending laterally over several
893 km and sustained over long periods of time, contrasts with the extremely localized outflow
894 observed at the seafloor over relatively small surfaces (spatial scales of a few hundreds of m at
895 most). Assuming that similar fluid circulation linked to deformation operates along the present-
896 day, active detachment fault and at depth, this would require an extreme fluid flow localization on
897 a short vertical distance (~2 km), in addition to implausible fluid transport within the footwall.

898 In our preferred interpretation, the fault zone and the fluids within cool down efficiently during
899 exhumation at the shallower levels of the fault. This cooling can effectively suppress convection
900 and any active circulation in shallow parts of the system, precluding discharge of high-temperature
901 fluids at the seafloor. We suggest that the observed present-day hydrothermal activity observed on
902 the surface of footwall of detachments (e.g., Rainbow, Semenov, Irinovskoe, Mount Den, Mount
903 Fuji) is most likely due to heat sources underlying these sites and located within the detachment
904 footwall, rather than fluids steered along the detachment fault and with significant lateral flow. The
905 hydrothermal system that we document here may be indeed active at depth at 13°20'N, and be
906 widespread at other systems. Indeed, many active detachments rooting near-axis (e.g., TAG,
907 Dragon Horn) may be active in close proximity to nearby heat sources (melt lenses or dykes
908 propagating along-axis), sampling fluids from the associated reaction zone at depth. As these
909 systems may be restricted to deep lithospheric levels (>1 km) and lack a seafloor expression, they
910 may only be identifiable studying in situ detachment fault rocks.

911

912 6. Conclusions

913 The 13°20'N detachment fault zone displays pervasive, syntectonic silicification of fault breccia
914 that is originally mostly of mafic origin (diabase). Quartz crystals in breccia matrix and clasts
915 preserve fluid inclusions. Their analyses, coupled to both bulk-rock and chlorite geochemical
916 compositions, allow us to constrain hydrothermal fluid flow during deformation, and propose a
917 conceptual model of detachment deformation and fluid flow.

918 First, we document the mixing of two fluid sources based on fluid inclusion salinity and gas
919 content: 1) primarily brines and minor amounts of vapor phases resulting from phase separation at
920 high temperature ($T > 410$ °C), and likely occurring in the hangingwall reaction zone at the base of
921 the dyke complex; and 2) minor amounts of fluids that interacted with ultramafic rocks, likely
922 recording serpentinization reactions at temperatures of 200-350 °C, associated with H₂ (and CH₄)
923 production. The lack of correlation between salinity and gas content, as well as quartz grain-scale
924 variations of fluid composition, suggests syntectonic mixing in variable proportions of
925 compositionally heterogeneous flows at small spatial and short temporal scales.

926 The hydrothermal circulation we document along the detachment fault zone reaches the base of
927 the hangingwall dyke complex, i.e., 2 km depth, as constrained by seismic refraction data. Fault
928 zone rocks are brecciated and incorporated into the detachment, together with the silica-rich brines
929 emanating from a nearby reaction zone. A significant temperature drop is recorded by chlorite
930 thermometry, from amphibolite facies (~500 °C) to quartz/chlorite equilibrium temperatures as low
931 as ~200 °C. This temperature drop likely occurs both over small spatial distances and over short
932 periods of time, with transients, promoting syntectonic silica precipitation in the fault zone. The
933 hydrothermal circulation documented here is decoupled from present day hydrothermal activity at
934 the seafloor. We suggest that detachment-related hydrothermal flow, which is widespread, is likely
935 hosted within the footwall of detachments, passively cross-cuts inactive detachment faults, and is
936 unrelated to the active detachment fault operating at depth.

937
938 **Acknowledgements** – The authors warmly acknowledge M-C. Caumon for her help with Raman
939 Spectroscopy on fluid inclusions at GeoRessources Nancy, O. Boudouma and M. Fialin for their
940 assistance with SEM-cathodoluminescence and EPMA respectively, M. Quintin and E. Delairis for
941 thin and thick sections preparation respectively. We thank B. Dubacq and J. Touret for fruitful

942 discussions on chlorite analysis and fluid inclusions, respectively. Two anonymous reviewers are
943 acknowledged for their critical remarks, and W. Berh and Associate Editor for editorial handling.
944 This work was funded by INSU Tellus-SYSTER program (ODEFLUIN). Data were acquired
945 during the ODEMAR cruise (<https://doi.org/10.17600/13030070>) and we thank the extraordinary
946 work of the crew, engineers, and officers that led to an extremely successful cruise. Bathymetry
947 (shipboard and AUV) data are publicly available through www.seanoe.org
948 (<https://doi.org/10.17882/48324>, <https://doi.org/10.17882/48335>), and samples presented here are
949 available for further studies through the Marine Rock Repository at IPGP (see lithotheque.ipgp.fr)
950 or contacting JE.

951 **References**

- 952 Allen, D.E. & Seyfried, W.E. (2003) Compositional controls on vent fluids from ultramatic-
953 hosted hydrothermal systems at mid-ocean ridges: An experimental study at 400 degrees C,
954 500 bars. *Geochimica Et Cosmochimica Acta*, 67, 1531-1542.
955 [https://doi.org/10.1016/S0016-7037\(02\)01173-0](https://doi.org/10.1016/S0016-7037(02)01173-0)
- 956 Alt, C. J. (1995). Subseafloor processes in mid-ocean ridge hydrothermal systems. In S. E.
957 Humphris et al. (Eds.), *Seafloor Hydrothermal Systems: Physical, Chemical, Bio- logical,*
958 *and Geological Interactions, Geophys. Monogr. Ser.* (Vol. 91, pp. 85–114). Washington, DC:
959 AGU, <https://doi.org/10.1029/GM091p0085>.
- 960 Alt, J.C., Laverne, C., Coggon, R.M., Teagle, D.A.H., Banerjee, N.R., Morgan, S., et al. (2010).
961 Subsurface structure of a submarine hydrothermal system in ocean crust formed at the East
962 Pacific Rise, ODP/IODP Site 1256. *Geochemistry, Geophysics, Geosystems*, 11(10), p. 1-28.
963 <https://doi.org/10.1029/2010GC003144>
- 964 Alt, J.C., Laverne, C., & Muehlenbachs, K. (1985). Alteration of the upper oceanic crust:
965 mineralogy and processes in Deep Sea Drilling Project Hole 504B, Leg 83. In R.N. Anderson,
966 J. Honnorez, K. Becker, et al., *Init. Repts. DSDP*, 83: Washington (US Govt. Printing Office),
967 217-247
- 968 Andersen, C., Rupke, L., Hasenclever, J., Grevemeyer, I., & Petersen, S. (2014). Fault geometry
969 and permeability contrast control vent temperatures at the Logatchev 1 hydrothermal field,
970 Mid-Atlantic Ridge. *Geology*, 43(1), 51–54. <https://doi.org/10.1130/G36113.1>
- 971 André-Mayer, A-S., Leroy, J.L., Bailly, L., Chauvet, A., Marcoux, E., Grancea, L., et al. (2002).
972 Boiling and vertical mineralization zoning: a case study from the Apacheta low-sulfidation
973 epithermal gold-silver deposit, southern Peru. *Mineralium Deposita*, 37, 452-464.
974 <https://doi.org/10.1007/s00126-001-0247-2>
- 975 Andreani, M., Escartin, J., Delacour, A., Ildefonse, B., Godard, M., Dymont, J., Fallick, A.E., &
976 Fouquet, Y. (2014). Tectonic structure, lithology, and hydrothermal signature of the Rainbow
977 massif (Mid-Atlantic Ridge 36°14'N). *Geochemistry, Geophysics, Geosystems*, 15, 3543-
978 3571. <https://doi.org/10.1002/2014GC005269>
- 979 Angiboust, S., Pettke, T., De Hoog, J.C.M., Caron, B., & Oncken, O. (2014). Channelized Fluid
980 Flow and Eclogite-facies Metasomatism along the Subduction Shear Zone. *J. Petrol.* 55,
981 883–916. <https://doi.org/10.1093/petrology/egu010>

- 982 Bach, W., Jons, N., & Klein, F. (2013). Metasomatism within the oceanic crust. In D. E. Harlov &
983 H. Austrheim (Eds.). *Metasomatism and the chemical transformation of rock*. Lecture notes
984 in Earth System Sciences. Springer, Berlin, Heidelberg. [https://doi.org/10.1007/978-3-642-](https://doi.org/10.1007/978-3-642-28394-9_8)
985 [28394-9_8](https://doi.org/10.1007/978-3-642-28394-9_8)
- 986 Berndt, M.E., Allen, D.E. & Seyfried, W.E. (1996) Reduction of CO₂ during serpentinization of
987 olivine at 300 degrees C and 500 bar (vol 24, pg 351, 1996). *Geology*, **24**, 671-671.
988 [https://doi.org/10.1130/0091-7613\(1996\)024<0351:ROCDSO>2.3.CO;2](https://doi.org/10.1130/0091-7613(1996)024<0351:ROCDSO>2.3.CO;2)
- 989 Bertelli, M. & Baker, T. (2010). A fluid inclusion study of the Suicide Ridge Breccia Pipe,
990 Cloncurry district, Australia: implication for breccia genesis and IOCG mineralization.
991 *Precambrian Research*, *179* (1-4), 69-87. <https://doi.org/10.1016/j.precamres2010.02.016>
- 992 Bodnar, R. J. (1993). Revised equation and table for determining the freezing point depression of
993 H₂O-NaCl solutions. *Geochim. Cosmochim. Acta* *57*, 683–684.
- 994 Boiron, M.C., Essarraj, S., Sellier, E., Cathelineau, M., Lespinasse, M., Poty, B. (1992).
995 Identification of fluid inclusions in relation to their host microstructural domains in quartz
996 by cathodoluminescence. *Geochim. Cosmochim Acta* *56*, 175–185.
- 997 Bonnemains, D., Escartín, J., Mével, C., Andreani, M., & Verlaguet, A. (2017). Pervasive
998 silicification and hanging wall overplating along the 13°20'N oceanic detachment fault (Mid-
999 Atlantic Ridge): *Geochemistry, Geophysics, Geosystems*, *18*(6), 2028–2053.
1000 <https://doi.org/10.1002/2017GC006846>
- 1001 Bortnikov, N.S., Simonov, V.A., Amplieva, E.E., & Borovikov, A.A. (2014). Anomalously high
1002 concentrations of metals in fluid of the Semenov Modern Hydrothermal System (Mid-
1003 Atlantic Ridge, 13°31'N): LA-ICP-MS study of fluid inclusions in minerals. *Doklady Earth*
1004 *Sciences*, *456*(2), 714-719. <https://doi.org/10.1134/S1028334X14060221>
- 1005 Bortnikov, N.S., Simonov, V.A., Amplieva, E.E., Stavrova, O.O., & Fouquet, Y. (2011). The
1006 physicochemical conditions of hydrothermal ore-forming systems of “black smokers”
1007 associated with mantle ultrabasites in the Central Atlantic region. *Russian Geology and*
1008 *Geophysics*, *52*(11), 1412–1420. <https://doi.org/10.1016/j.rgg.2011.10.010>
- 1009 Bortnikov, N.S., Simonov, V.A., Borovikov, A.A., Bel, V.E., Amplieva, E.E., Kotlyarov, A. V,
1010 and Bryanskiy, N. V (2015). The metalliferous fluid of the hydrothermal sulfide system
1011 associated with the oceanic core complex 13°20'N, The Mid-Atlantic Ridge (LA-ICP-MS
1012 and fluid inclusions), in *Oceanic Core Complexes and Hydrothermalism*, p. 80–83

- 1013 Boschi, C., Früh-Green, G., Delacour, A., Karson, J., & Kelley, D.S. (2006). Mass transfer and
1014 fluid flow during detachment faulting and development of an oceanic core complex, Atlantic
1015 Massif (MAR 30°N). *Geochemistry, Geophysics, Geosystems*, 7(1), Q01004,
1016 <https://doi.org/10.1029/2005GC001074>
- 1017 Boulart, C., Chavagnac, V., Monnin, C., Delacour, A., Ceuleneer, G., & Hoareau, G. (2013).
1018 Differences in gas venting from ultramafic-hosted warm springs: the example of Oman and
1019 Ligurian Ophiolites. *Ophioliti*, 38(2), 142-156. <https://doi.org/10.4454/ofioliti.v38i2.423>.
- 1020 Bourdelle, F., Parra, T., Chopin, C., & Beyssac, O. (2013). A new chlorite geothermometer for
1021 diagenetic to low-grade metamorphic conditions. *Contributions to Mineralogy and
1022 Petrology*, 165(4), 723–735. <https://doi.org/10.1007/s00410-012-0832-7>
- 1023 Bourdelle, F. & M. Cathelineau (2015). Low-temperature chlorite geothermometry: a graphical
1024 representation based on a T–R²⁺–Si diagram. *European Journal of Mineralogy*, 27(5), 617-
1025 626. <https://doi.org/10.1127/ejm/2015/0027-2467>
- 1026 Boutoux, A., Verlaquet, A., Bellahsen, N., Lacombe, O., Villemant, B., Caron, B., Martin, E.,
1027 Assayag, N., & Cartigny, P. (2014) Fluid systems above basement shear zones during
1028 inversion of pre-orogenic sedimentary basins (External Crystalline Massifs, Western Alps).
1029 *Lithos*, 206–207, 435–453. <https://doi.org/10.1016/j.lithos.2014.07.005>
- 1030 Buck, W.R., Lavier, L.L., and Poliakov, A.N.B., 2005, Modes of faulting at mid-ocean ridges:
1031 *Nature*, v. 434, p. 719–723
- 1032 Canales, J.P., Dunn, R.A., Arai, R., & Sohn, R.A. (2017). Seismic imaging of magma sills beneath
1033 an ultramafic-hosted hydrothermal system. *Geology*, 45(5), 451–454.
1034 <https://doi.org/10.1130/G38795.1>
- 1035 Cann, J.R. (1969). Spilites from the Carlsberg Ridge, Indian Ocean. *Journal of Petrology*, 10, 1–
1036 19
- 1037 Cannat, M., Sauter, D., Mendel, V., Ruellan, E., Okino, K., Escartin, J., Combier, V., & Baala, M.
1038 (2006). Modes of seafloor generation at a melt-poor ultraslow-spreading ridge. *Geology*,
1039 34(7), 605–608. <https://doi.org/10.1130/G22486.1>
- 1040 Carignan, J., Hild, P., Mevelle, G., Morel, J., & Yeghicheyan, D. (2001). Routine analyses of trace
1041 elements in geological samples using flow injection and low pressure on-line liquid
1042 chromatography coupled to ICP-MS: a study of geochemical reference materials BR, DR-N,

1043 UB-N, AN-G and GH. *Geostandards and Geoanalytical Research*, 25(2–3), 187–198.
1044 <https://doi.org/10.1111/j.1751-908X.2001.tb00595.x>

1045 Castelain, T., McCaig, A.M., & Cliff, R.A. (2014). Fluid evolution in an Oceanic Core Complex:
1046 A fluid inclusion study from IODP hole U1309 D-Atlantis Massif, 30°N, Mid-Atlantic
1047 Ridge. *Geochemistry, Geophysics, Geosystems*, 15(4), 1193–1214.
1048 <https://doi.org/10.1002/2013GC004975>

1049 Charlou, J.L., Fouquet, Y., Bougault, H., Donval, J.P., Etoubleau, J., Jean-Baptiste, P., Dapoiny,
1050 A., Appriou, P., & Rona, P.A. (1998). Intense CH₄ plumes generated by serpentinization of
1051 ultramafic rocks at the intersection of the 15°20'N fracture zone and the Mid-Atlantic Ridge.
1052 *Geochim. Cosmochim. Acta* 62, 2323 – 2333. [https://doi.org/10.1016/S0016-7037\(98\)00138-](https://doi.org/10.1016/S0016-7037(98)00138-0)
1053 0

1054 Charlou, J.J., Donval, J.P., Fouquet, Y., Jean Baptiste, P., & Holm, N. (2002). Geochemistry of
1055 high H₂ and CH₄ vent fluids issuing from ultramafic rocks at the Rainbow hydrothermal field
1056 (36°14'N, MAR). *Chemical Geology*, 191, 345–359. [https://doi.org/10.1016/S0009-](https://doi.org/10.1016/S0009-2541(02)00134-1)
1057 2541(02)00134-1

1058 Cherkashev, G.A., Ivanov, V.N., Lazareva, L.I., Rozhdestvenskaya, I.I., Samovarov, M.L.,
1059 Poroshina, I.M., Sergeev, M.B., Stepanova, T. V, &c Dobretsova, I.G. (2013). Massive
1060 sulfide ores of the northern equatorial Mid Atlantic Ridge. *Oceanology*, 53(5), 607–619.
1061 <https://doi.org/10.1134/S0001437013050032>

1062 Coumou, D., Driesner, T., Geiger, S., Paluszny, A., & Heinrich, C. A. (2009). High-resolution
1063 three-dimensional simulations of mid-ocean ridge hydrothermal systems. *J. Geophys. Res.*,
1064 114, B07104, <https://doi.org/10.1029/2008JB006121>

1065 Delaney, J.R., Mogk, D.W., & Mottl, M. (1987). Quartz-cemented breccias from the Mid-Atlantic
1066 Ridge: Samples of a high-salinity hydrothermal upflow zone. *Journal of Geophysical*
1067 *Research*, 92(B9), 9175. <https://doi.org/10.1029/JB092iB09p09175>

1068 deMartin, B.J., Sohn, R.A., Canales, J.P., & Humphris, S.E. (2007). Kinematics and geometry of
1069 active detachment faulting beneath the Trans-Atlantic Geotraverse (TAG) hydrothermal field
1070 on the Mid-Atlantic Ridge. *Geology*, 35(8), 711–714. <https://doi.org/10.1130/G23718A.1>

1071 Destrigneville, C., Chavagnac, V., Olive, J-A., Leleu, T., Rommevaux, C., Escartín, J., Jamieson,
1072 J., & Petersen S. (2015). Thermo-chemical fluxes, reactions and mixing in hydrothermal

1073 plumes at oceanic core complexes (Mid-Atlantic Ridge, 13°30'N and 13°20'N). Presented at
1074 AGU Meeting, San Francisco, USA, 14-18 Dec. 2015

1075 Diamond, L.W., Tarantola, A., & Stünitz, H. (2010). Modification of fluid inclusions in quartz by
1076 deviatoric stress II: experimentally induced changes in inclusion volume and composition.
1077 *Contrib. Mineral. Petrol.* 160, 845–864. <https://doi.org/10.1007/s00410-010-0510-6>

1078 Dubessy, J., Poty, B., & Ramboz, C. (1989). Advances in C-O-H-N-S fluid geochemistry based on
1079 micro-Raman spectrometric analysis of fluid inclusions. *European Journal of Mineralogy*,
1080 1(4), 517–534. <https://doi.org/10.1127/ejm/1/4/0517>

1081 Dunn, R.A., Arai, R., Eason, D.E., Canales, J.P., & Sohn, R.A. (2017). Three-Dimensional Seismic
1082 Structure of the Mid-Atlantic Ridge: An Investigation of Tectonic, Magmatic, and
1083 Hydrothermal Processes in the Rainbow Area. *Journal of Geophysical Research: Solid*
1084 *Earth*, 122(12), 9580–9602. <https://doi.org/10.1002/2017JB015051>

1085 Escartín, J., Mével, C., Petersen, S., Bonnemains, D., Cannat, M., Andreani, M., Augustin, N.,
1086 Bezos, A., Chavagnac, V., Choi, Y., Godard, M., Haaga, K., Hamelin, C., Ildefonse, B., et
1087 al. (2017). Tectonic structure, evolution, and the nature of oceanic core complexes and their
1088 detachment fault zones (13°20'N and 13°30'N, Mid Atlantic Ridge): *Geochemistry*,
1089 *Geophysics, Geosystems*, 18, (4), 1451–1482. <https://doi.org/10.1002/2016GC006775>

1090 Escartín, J., Mével, C., MacLeod, C.J., & McCaig, A.M. (2003). Constraints on deformation
1091 conditions and the origin of oceanic detachments: The Mid-Atlantic Ridge core complex at
1092 15°45'N. *Geochemistry, Geophysics, Geosystems*, 4(8), 1067.
1093 <https://doi.org/10.1029/2001GC000278>

1094 Escartín, J., Smith, D.K., Cann, J., Schouten, H., Langmuir, C.H., & Escrig, S. (2008). Central role
1095 of detachment faults in accretion of slow-spreading oceanic lithosphere. *Nature*, 455(7214),
1096 790–794. <https://doi.org/10.1038/nature07333>

1097 Fontaine, F.J., & Wilcock, W.S.D. (2006). Dynamics and storage of brine in mid-ocean ridge
1098 hydrothermal systems. *Journal of Geophysical Research*, 111, B06102.
1099 <https://doi.org/10.1029/2005JB003866>

1100 Fontaine, F.J., Wilcock, W.S.D., & Butterfield, D.A. (2007). Physical controls on the salinity of
1101 mid-ocean ridge hydrothermal vent fluids. *Earth and Planetary Science Letters*, 257, 132-
1102 145. <https://doi:10.1016/j.epsl.2007.02.027>

1103 Fouquet, Y., Cambon, P., Etoubleau, J., Charlou, J.L., Ondréas, H., Barriga, F.J.A.S., Cherkashov,
1104 G., Semkova, T., Poroshina, I., Bohn, M., Donval, J.P., Henry, K., Murphy, P., & Rouxel, O.
1105 (2010). Geodiversity of Hydrothermal Processes Along the Mid-Atlantic Ridge and
1106 Ultramafic-Hosted Mineralization: a New Type Of Oceanic Cu-Zn-Co-Au Volcanogenic
1107 Massive Sulfide Deposit, *in* Diversity Of Hydrothermal Systems On Slow Spreading Ocean
1108 Ridges, American Geophysical Union, p. 321–367

1109 Foustoukos, D.I. & Seyfried, W.E. (2005) Redox and pH constraints in the subseafloor root zone
1110 of the TAG hydrothermal system, 26°N Mid-Atlantic Ridge. *Earth and Planetary Science*
1111 *Letters*, 235, 497-510. <https://doi.org/10.1016/j.epsl.2005.04.042>

1112 Frezzotti, M.L., Ferrando, S., Tecce, F., & Castelli, D. (2012). Water content and nature of solutes
1113 in shallow-mantle fluids from fluid inclusions. *Earth and Planetary Science Letters*, 351–
1114 352, 70–83. <https://doi.org/10.1016/j.epsl.2012.07.023>

1115 Früh-Green, G.L., Kelley, D.S., Bernasconi, S.M., Karson, J.A., Ludwig, K.A., Butterfield, D.A.,
1116 Boschi, C., & Proskurowski, G. (2003) 30,000 Years of Hydrothermal Activity at the Lost
1117 City Vent Field. *Science*, 301, 495–498

1118 Gillis, K., & Thompson, G. (1993). Metabasalts from the Mid-Atlantic Ridge: new insights into
1119 hydrothermal systems in slow-spreading crust. *Contrib. Mineral. Petrol.*, 113, 502-523

1120 Godard, M., Lagabrielle, Y., Alard, O., & Harvey, J. (2008). Geochemistry of the highly depleted
1121 peridotites drilled at ODP Sites 1272 and 1274 (Fifteen-Twenty Fracture Zone, Mid-Atlantic
1122 Ridge): Implications for mantle dynamics beneath a slow spreading ridge. *Earth and*
1123 *Planetary Science Letters*, 267(3–4), 410–425. <https://doi.org/10.1016/j.epsl.2007.11.058>

1124 Hodgkinson, M.R.S., Webber, A.P., Roberts, S., Mills, R.A., Connelly, D.P., & Murton, B.J.
1125 (2015). Talc-dominated seafloor deposits reveal a new class of hydrothermal system: *Nature*
1126 *Communications*, 6, 10150. <https://doi.org/10.1038/ncomms10150>

1127 Holm, N.G., & Charlou, J.L. (2001). Initial indications of abiotic formation of hydrocarbons in the
1128 Rainbow ultramafic hydrothermal system, Mid-Atlantic Ridge. *Earth Planet. Sci. Lett.*, 191,
1129 1–8.

1130 Honnorez, J., Alt, J.C. & Humphris, S.E. (1998). Vivesection and autopsy of active and fossil
1131 hydrothermal alteration of basalts beneath and within the TAG hydrothermal mound: Herzig,
1132 P.M., Humphris, S.E., Miller, D.J., and Zierenberg, R.A. (Eds.), *Proceedings of the Ocean*
1133 *Drilling Program, Scientific Results*, Vol. 158, p. 231-254

- 1134 Humphris, S.E., & Thompson, G. (1978). Hydrothermal alteration of oceanic basalts by seawater.
1135 *Geochim. Cosmochim. Acta* 42, 107–125.
- 1136 Humphris, S.E., Alt, J.C., Teagle, D.A.H., & Honnorez, J.J. (1998). Geochemical changes during
1137 hydrothermal alteration of basement in the stockwork beneath the active TAG hydrothermal
1138 mound, *in* Proceedings of the Ocean Drilling Program, 158 Scientific Results, Ocean Drilling
1139 Program, p. 255–276.
- 1140 Karson, J.A., Früh-Green, G.L., Kelley, D.S., Williams, E.A., Yoerger, D.R., & Jakuba, M. (2006).
1141 Detachment shear zone of the Atlantis Massif core complex, Mid-Atlantic Ridge, 30°N.
1142 *Geochemistry, Geophysics, Geosystems*, 7(6), Q06016.
1143 <https://doi.org/10.1029/2005GC001109>
- 1144 Kelley, D.S., & Delaney, J.R. (1987). Two-phase separation and fracturing in mid-ocean ridge
1145 gabbros at temperatures greater than 700 °C. *Earth. Planet. Sci. Lett.*, 83, 53-66
- 1146 Kelley, D.S., Gillis, K.M., & Thompson, G. (1993). Fluid evolution in submarine magma-
1147 hydrothermal systems at the Mid-Atlantic Ridge. *Journal of Geophysical Research*, 98(B11),
1148 19579–19596
- 1149 Kelley, D.S., & Robinson, P.T. (1990). Development of a brine-dominated hydrothermal system
1150 at temperatures of 400–500 °C in the upper level plutonic sequence, Troodos ophiolite,
1151 Cyprus. *Geochim. Cosmochim. Acta*, 54, 653–661
- 1152 Kelley, D. S., Robinson P. T., & Malpas, J. G. (1992). Processes of brine generation and circulation
1153 in the oceanic crust: Fluid inclusion evidence from the Troodos Ophiolite, Cyprus. *J.*
1154 *Geophys. Res*, 97, B6, 9307-9322.
- 1155 Klein, F., Grozeva, N.G., & Seewald, J.S. (2019). Abiotic methane synthesis and serpentinization
1156 in olivine-hosted fluid inclusions. *Proceedings of the National Academy of Sciences*, 116(36),
1157 17666–17672. <https://doi.org/10.1073/pnas.1907871116>
- 1158 Leisen, M., Boiron, M.C., Richard, A., & Dubessy, J. (2012). Determination of Cl and Br
1159 concentrations in individual fluid inclusions by combining microthermometry and LA-
1160 ICPMS analysis: Implications for the origin of salinity in crustal fluids. *Chemical Geology*,
1161 330–331, 197–206. <https://doi.org/10.1016/j.chemgeo.2012.09.003>
- 1162 Locatelli, M., Verlaquet, A., Agard, P., Pettke, T., & Federico, L. (2019). Fluid pulses during
1163 stepwise brecciation at intermediate subduction depths (Monviso eclogites, W. Alps): first

1164 internally then externally sourced, *Geochemistry, Geophysics, Geosystems*, 20(3).
1165 <https://doi.org/10.1029/2019GC008549>

1166 Longerich, H. P., Jackson, S. E., & Gunther, D. (1996). Laser ablation inductively coupled plasma
1167 mass spectrometric transient signal data acquisition and analyte concentration calculation. *J.*
1168 *Anal. Atom. Spectrom.* 11, 899–904

1169 MacLeod, C.J., Escartín, J., Banerji, D., Banks, G.J., Gleeson, M., Irving, D.H.B., Lilly, R.M.,
1170 McCaig, A., Niu, Y.-L., Allerton, S., & Smith, D.K. (2002). Direct geological evidence for
1171 oceanic detachment faulting: The Mid-Atlantic Ridge, 15°45'N. *Geology*, 30(10), 279–282.

1172 MacLeod, C.J., Searle, R.C., Casey, J.F., Mallows, C., Unsworth, M., Achenbach, K., & Harris,
1173 M. (2009). Life cycle of oceanic core complexes. *Earth and Planetary Science Letters*, 287,
1174 333–344

1175 Mallows, C., & Searle, R.C. (2012). A geophysical study of oceanic core complexes and
1176 surrounding terrain, Mid-Atlantic Ridge 13°N–14°N. *Geochemistry Geophysics Geosystems*,
1177 13(1), Q0AG08. <https://doi.org/10.1029/2012GC004075>

1178 Martin, B., & Fyfe, W. S. (1970). Some experimental and theoretical observations on the kinetics
1179 of hydration reactions with particular reference to serpentinization, *Chem. Geol.*, 6, 185–202.
1180 [https://doi.org/10.1016/0009-2541\(70\)90018-5](https://doi.org/10.1016/0009-2541(70)90018-5).

1181 McCaig, A., Cliff, R.A., Escartín, J., Fallick, A.E., & MacLeod, C.J. (2007). Oceanic detachment
1182 faults focus very large volumes of black smoker fluids. *Geology*, 35, 935–938.
1183 <https://doi.org/10.1130/G23657A.1>

1184 McCaig, A.M., Delacour, A., Fallick, A.E., Castelain, T., & Früh-Green, G.L. (2010). Detachment
1185 fault control on hydrothermal circulation systems: Interpreting the subsurface beneath the
1186 TAG hydrothermal field using the isotopic and geological evolution of oceanic core
1187 complexes in the Atlantic. *Geophysical Monograph Series*, 188, 207–239.
1188 <https://doi.org/10.1029/2008GM000729>

1189 McCaig, A.M., & Harris, M. (2012). Hydrothermal circulation and the dike-gabbro transition in
1190 the detachment mode of slow seafloor spreading. *Geology*, 40, 367–370

1191 McCollom, T.M. & Bach, W. (2009) Thermodynamic constraints on hydrogen generation during
1192 serpentinization of ultramafic rocks. *Geochimica et Cosmochimica Acta*, 73, 856–875.
1193 <https://doi.org/10.1016/j.gca.2008.10.032>

1194 McDermott, J.M., Seewald, J.S., German, C.R. & Sylva, S.P. (2015) Pathways for abiotic organic
1195 synthesis at submarine hydrothermal fields. *PNAS*, *112*(25), 7668-7672. [https://doi.org](https://doi.org/10.1073/pnas.1506295112)
1196 [/10.1073/pnas.1506295112](https://doi.org/10.1073/pnas.1506295112)

1197 McDermott, J.M., Sylva, S.P., Ono, S., German, C.R. & Seewald, J.S. (2018) Geochemistry of
1198 fluids from Earth's deepest ridge-crest hot-springs: Piccard hydrothermal field, Mid-Cayman
1199 Rise. *Geochimica and Cosmochimica Acta*, *228*, 95-118. [https://doi.org](https://doi.org/10.1016/j.gca.2018.01.021)
1200 [/10.1016/j.gca.2018.01.021](https://doi.org/10.1016/j.gca.2018.01.021)

1201 Monnin, C., Chavagnac, V., Boulart, C., Ménez, B., Gérard, M., Gérard, E., Quéméneur M., Erauso
1202 G., Postec A., Guentas-Dombrowski L., Payri C., & Pelletier B. (2014). The low temperature
1203 hyperalkaline hydrothermal system of the Prony Bay (New Caledonia). *Biogeosciences*
1204 *Discussion*, *11*, 5687-5706. <https://doi:10.5194/bg-11-5687-2014>

1205 Mottl, M.J. (1983). Metabasalts, axial hot springs, and the structure of hydrothermal systems at
1206 mid- ocean ridges. *Geol. Soc. Am. Bull.* *94*, 161–180

1207 Olive, J.A., Parnell-Turner, R., Escartin, J., Smith, D.K., & Petersen, S. (2019). Controls on the
1208 seafloor exposure of detachment fault surfaces. *Earth and Planetary Science Letters*, *506*,
1209 381-387. <https://doi.org/10.1016/j.epsl.2018.11.001>

1210 Ondréas, H., Cannat, M., Fouquet, Y., & Normand, A. (2012). Geological context and vents
1211 morphology of the ultramafic-hosted Ashadze hydrothermal areas (Mid-Atlantic Ridge
1212 13°N). *Geochemistry Geophysics Geosystems*, *13*(1), Q0AG14.
1213 <https://doi.org/10.1029/2012GC004433>

1214 Parnell-Turner, R., White, N., Henstock, T.J., Jones, S.M., MacLennan, J., & Murton, B.J. (2017).
1215 Causes and Consequences of Diachronous V-Shaped Ridges in the North Atlantic Ocean.
1216 *Journal of Geophysical Research: Solid Earth*, *122*(11), 8675–8708.
1217 <https://doi.org/10.1002/2017JB014225>

1218 Parnell-Turner, R., Escartín, J., Olive, J.-A., Smith, D.K., & Petersen, S. (2018). Genesis of
1219 corrugated fault surfaces by strain localization recorded at oceanic detachments. *Earth and*
1220 *Planetary Science Letters*, *498*, 116–128. <https://doi.org/10.1016/j.epsl.2018.06.034>

1221 Pasteris, J.D., Wopenka, B., & Seitz, J.C. (1988). Practical aspects of quantitative laser Raman
1222 microprobe spectroscopy for the study of fluid inclusions. *Geochimica et Cosmochimica*
1223 *Acta*, *52*, 979–988

1224 Paulick, H., Bach, W., Godard, M., de Hoog, J.C.M., Suhr, G., & Harvey, J. (2006). Geochemistry
1225 of abyssal peridotites (Mid-Atlantic Ridge, 15°20'N, ODP Leg 209): implications for fluid-
1226 rock interaction in slow spreading environments. *Chemical Geology*, 234(3-4), 179-210

1227 Pearce, N. J. G., Perkins, W. T., Westgate, J. A., Gorton, M. P., Jackson, S. E., Nael, C. R. &
1228 Chenery, S. P. (1997). Compilation of new and published major trace element data for NIST
1229 610 NIST SRM 612 glass reference materials. *Geostand. Newslett.* 21, 115–144.

1230 Pertsev, A.N., Bortnikov, N.S., Vlasov, E.A., Beltenev, V.E., Dobretsova, I.G., & Ageeva, O. A.
1231 (2012). Recent massive sulfide deposits of the Semenov ore district, Mid-Atlantic Ridge,
1232 13°31' N: Associated rocks of the oceanic core complex and their hydrothermal alteration.
1233 *Geology of Ore Deposits*, 54(5), 334–346. <https://doi.org/10.1134/S1075701512050030>.

1234 Petersen, S., Hertzog, M., & Hannington, M.D. (1998). Fluid inclusion studies as a guide to the
1235 temperature regime within the TAG hydrothermal mound, 26°, Mid-Atlantic Ridge. In P.M.
1236 Hertzog, S.E. Humphris, D.J. Miller, R.A. Zierenberg (Eds.), *Proceedings of the Ocean*
1237 *Drilling Program, Scientific Results* (vol. 158, pp. 163-178).

1238 Petersen, S., Kuhn, K., Kuhn, T., Augustin, N., Hekinian, R., Franz, L., & Borowski, C. (2009).
1239 The geological setting of the ultramafic-hosted Logatchev hydrothermal field (14°45'N,
1240 Mid-Atlantic Ridge) and its influence on massive sulfide formation. *Lithos*, 112(1-2), 40-56.
1241 <https://doi.org/10.1016/j.lithos.2009.02.008>

1242 Raimbourg, H., Thiéry, R., Vacelet, M., Ramboz, C., Cluzel, N., Le Trong, E., Yamaguchi, A., &
1243 Kimura, G. (2014). A new method of reconstituting the P-T conditions of fluid circulation in
1244 an accretionary prism (Shimanto, Japan) from microthermometry of methane-bearing
1245 aqueous inclusions. *Geochim. Cosmochim. Acta* 125, 96–109.
1246 <http://dx.doi.org/10.1016/j.gca.2013.09.025>.

1247 Roedder, E. (1984). Fluid Inclusions. *Reviews in Mineralogy*, Vol. 12, Mineralogical Society of
1248 America, 644 p.

1249 Saccoccia, P.J., & Gillis, K.M. (1995). Hydrothermal upflow zones in the oceanic crust. *Earth and*
1250 *Planetary Science Letters*, 136, 1–16

1251 Scheuermann, P.P., Tan, C. & Seyfried, W.E. (2018) Quartz solubility in the two-phase region of
1252 the NaCl-H₂O system: an experimental study with application to the Piccard hydrothermal
1253 field, Mid-Cayman Rise. *Geochemistry, Geophysics, Geosystems*, 19, 3570-3582.
1254 <https://doi.org/10.1029/2018GC007610>.

1255 Scheuermann, P.P., Xing, Y., Ding, K. & Seyfried, W.E. (2020) Experimental measurement of
1256 H₂(aq) solubility in hydrothermal fluids: application to the Piccard hydrothermal field, Mid-
1257 Cayman Rise. *Geochemica and Cosmochimica Acta*, (283), 22-39.
1258 <https://doi.org/10.1016/j.gca.2020.05.020>.

1259 Schmidt, K., Garbe-Schönberg, D., Koschinsky, A., Strauss, H., Jost, C. L., Klevenz, V., &
1260 Königer P. (2011). Fluid elemental and stable isotope composition of the Nibelungen
1261 hydrothermal field (8°18'S, Mid-Atlantic Ridge): constraints on fluid–rock interaction in
1262 heterogeneous lithosphere. *Chem. Geol.*, 280, 1–18.

1263 Schroeder, T., & John, B.E. (2004). Strain localization on an oceanic detachment fault system,
1264 Atlantis Massif, 30°N, Mid-Atlantic Ridge. *Geochemistry, Geophysics, Geosystems*, 5(11),
1265 Q11007. <https://doi.org/10.1029/2004GC00728>.

1266 Seyfried, W.E., Foustoukos, D.I. & Fu, Q. (2007) Redox evolution and mass transfer during
1267 serpentinization: An experimental and theoretical study at 200 degrees C, 500 bar with
1268 implications for ultramafic-hosted hydrothermal systems at Mid-Ocean Ridges. *Geochimica*
1269 *Et Cosmochimica Acta*, 71, 3872-3886. <https://doi.org/10.1016/j.gca.2007.05.015>

1270 Simão, N.M., Peirce, C., Funnell, M.J., Robinson, A.H., Searle, R.C., MacLeod, C.J., & Reston,
1271 T.J. (2020). 3-D P-wave velocity structure of oceanic core complexes at 13°N on the Mid-
1272 Atlantic Ridge. *Geophysical Journal International*, 221(3), 1555–1579.
1273 <https://doi.org/10.1093/gji/ggaa093>

1274 Simonov, V.A., Borovikov, A.A., Kotlyarov, A.V., Amplieva, E.E., & Bortnikov, N.S. (2015). *LA-*
1275 *ICP-MS evidence for high concentrations of metals in fluid from modern sea-floor*
1276 *hydrothermal systems: a case study of fluid inclusions in minerals from Semenov, Ashadze,*
1277 *and Logatchev sulfide edifices (Mid-Atlantic Ridge)*. Paper presented at the proceedings of
1278 the 13th biennial SGA meeting, 24-27 August 2015, Nancy, France

1279 Smith, D.K., Cann, J.R., & Escartín, J. (2006). Widespread active detachment faulting and core
1280 complex formation near 13° N on the Mid-Atlantic Ridge. *Nature*, 442(7101), 440–443.
1281 <https://doi.org/10.1038/nature04950>

1282 Smith, D.K., Escartín, J., Schouten, H., & Cann, J.R. (2008). Fault rotation and core complex
1283 formation: Significant processes in seafloor formation at slow-spreading mid-ocean ridges
1284 (Mid-Atlantic Ridge, 13 –15° N). *Geochemistry, Geophysics, Geosystems*, 9(3), Q03003.
1285 <https://doi.org/10.1029/2007GC001699>

1286 Son, J., Pak, S.-J., Kim, J., Baker, E.T., You, O.-R., Son, S., & Moon, J. (2014). Tectonic and
1287 magmatic control of hydrothermal activity along the slow-spreading Central Indian Ridge,
1288 8°S-17°S. *Geochemistry, Geophysics, Geosystems*, 15(5), 2011–2020.
1289 <https://doi.org/10.1002/2013GC005206>

1290 Sourirajan, S. & Kennedy, G.C. (1962). The system H₂O–NaCl at elevated temperatures and
1291 pressures, *Am. J. Sci.*, 260, 115–141.

1292 Spandler, C., Pettke, T., & Rubatto, D. (2011). Internal and external fluid sources for eclogite-
1293 facies veins in the Monviso meta-ophiolite, Western Alps: Implications for fluid flow in
1294 subduction zones. *Journal of Petrology*, 52(6), 1207–1236.
1295 <https://doi.org/10.1093/petrology/egr025>

1296 Steele-MacInnis, M., Bodnar, R.J., & Naden, J. (2011). Numerical model to determine the
1297 composition of H₂O–NaCl–CaCl₂ fluid inclusions based on microthermometric and
1298 microanalytical data. *Geochimica et Cosmochimica Acta*, 75(1), 21–40.
1299 <https://doi.org/10.1016/j.gca.2010.10.002>

1300 Tao, C., Seyfried, W.E., Lowell, R.P., Liu, Y., Liang, J., Guo, Z., Ding, K., Zhang, H., Liu, J., Qiu,
1301 L., Egorov, I., Liao, S., Zhao, M., Zhou, J., et al. (2020). Deep high-temperature
1302 hydrothermal circulation in a detachment faulting system on the ultra-slow spreading ridge.
1303 *Nature Communications*, 11(1), 1300. <https://doi.org/10.1038/s41467-020-15062-w>

1304 Tarantola, A., Diamond, L.W., & Stünitz, H. (2010). Modification of fluid inclusions in quartz by
1305 deviatoric stress. I: experimentally induced changes in inclusion shapes and microstructures.
1306 *Contrib. Mineral. Petrol.*, 160, 825–843.

1307 Tarantola, A., Diamond, L.W., Stünitz, H., Thust, A., & Pec, M. (2010). Modification of fluid
1308 inclusions in quartz by deviatoric stress. III: influence of principal stresses on inclusion
1309 density and orientation. *Contrib. Mineral. Petrol.*, 164, 537-550.

1310 Tivey, M.K., Mills, R.A., & Teagle, D.A.H. (1998). Temperature and salinity of fluid inclusions
1311 in anhydrite as indicators of seawater entrainment and heating in the TAG active mound. In:
1312 Herzig PM, Humphris SE, Miller DJ, Zierenberg RA (eds) *Proceedings of the ocean drilling
1313 program, scientific results, vol 158*. Ocean drilling program, College Station, 179–190

1314 Touret, J.L.R. (2001). Fluids in metamorphic rocks. *Lithos* 55(1-4), 1-25.
1315 [https://doi.org/10.1016/S0024-4937\(00\)00036-0](https://doi.org/10.1016/S0024-4937(00)00036-0)

- 1316 Tucholke, B.E., Behn, M.D., Buck, W.R., & Lin, J. (2008). Role of melt supply in oceanic
1317 detachment faulting and formation of megamullions. *Geology*, 36(6), 455–458.
1318 <https://doi.org/10.1130/G24639A>
- 1319 Van den Kerkhof, A.M., & Hein, U.F. (2001). Fluid inclusion petrography. *Lithos*, 55(1–4), 27–
1320 47. [https://doi.org/10.1016/S0024-4937\(00\)00037-2](https://doi.org/10.1016/S0024-4937(00)00037-2)
- 1321 Vanko, D.A. (1988). Temperature, pressure, and composition of hydrothermal fluids with their
1322 bearing on the magnitude of tectonic uplift at mid-ocean ridges, inferred from fluid inclusions
1323 in oceanic layer 3 rocks. *J. Geophys. Res.*, 93, 4595-4611
- 1324 Vanko, D. A., Wolfgang, B., Roberts, S., Yeats, C.J., & Scott, S.D. (2004). Fluid inclusion
1325 evidence for subsurface phase separation and variable fluid mixing regimes beneath the deep-
1326 sea PACMANUS hydrothermal field, Manus Basin back arc rift, Papua New Guinea. *Journal*
1327 *of Geophysical Research*, 109(B3), B03201. <https://doi.org/10.1029/2003JB002579>
- 1328 Vidal, O., De Andrade, V., Lewin, E., Munoz, M., Parra, T., & Pascarelli, S. (2006). P-T-
1329 deformation-Fe³⁺/Fe²⁺ mapping at the thin section scale and comparison with XANES
1330 mapping: application to a garnet-bearing metapelite from the Sambagawa metamorphic belt
1331 (Japan). *J. Metamorph. Geol.*, 24(7), 669–683
- 1332 Vidal, O., & Parra, T. (2000). Exhumation paths of high-pressure metapelites obtained from local
1333 equilibria for chlorite-phengite assemblages. *Geol. J.* 35(3–4), 139–161
- 1334 Vidal, O., Parra, T., & Trotet, F. (2001). A thermodynamic model for Fe-Mg aluminous chlorite
1335 using data from phase equilibrium experiments and natural pelitic assemblages in the 100–
1336 600 °C, 1–25 kb range. *Am. J. Sci.*, 301(6), 557–592
- 1337 Vidal, O., Parra, T., & Vieillard, P. (2005). Thermodynamic properties of the Tschermak solid
1338 solution in Fe-chlorite: application to natural examples and possible role of oxidation. *Am.*
1339 *Mineral.*, 90(2–3), 347–358
- 1340 Vityk, M.O., & Bodnar, R.J. (1995). Textural evolution of synthetic fluid inclusions in quartz
1341 during reequilibration, with applications to tectonic reconstruction. *Contrib. Mineral. Petrol.*
1342 121, 309–323.
- 1343 Walshe, J-L. (1986). A six-component chlorite solid solution model and the conditions of chlorite
1344 formation in hydrothermal and geothermal systems. *Econ. Geol.*, 81, 681-703

- 1345 Wetzel, L.R., & Shock, E.L. (2000). Distinguishing ultramafic- from basalt-hosted submarine
1346 hydrothermal vent fluid compositions. *Journal of Geophysical Research*, *105*(B4), 8319–
1347 8340
- 1348 Wilson, S.C., Murton, B.J., & Taylor, R.N. (2013). Mantle composition controls the development
1349 of an Oceanic Core Complex. *Geochemistry, Geophysics, Geosystems*, *14*, 1–18.
1350 <https://doi.org/10.1002/ggge.20046>.
- 1351 Zhang, Y.G., & Frantz, J.D. (1987). Determination of the homogenization temperatures and
1352 densities of supercritical fluids in the system NaCl-KCl-CaCl₂-H₂O using synthetic fluid
1353 inclusions. *Chemical Geology*, *64*, 335-350.
- 1354

1355 **Tables**

1356

1357 **Table 1.** Characteristics of the six fault rocks considered for this study. The outcrop numbers refer to Figure 1b and to Bonnemains et
 1358 al. (2017).

1359

Outcrop	Sample # ODM ROC_ Referred to as	IGSN	Latitude	Longitude	Depth (m)	Rock type	Texture	Mineralogical composition*	Quartz content	Analyses		
										Whole rock	Chlorite	Fluid Inclusions
1	V547_115 ODM115	CNRS0000000115	13°18.96' N	-44°53.43' W	3159	mafic	clast of breccia with vacuoles	Chl, Pl, Px, Pmp	absent	x	x	
2	V552_217 ODM217	CNRS0000000221	13°19.22' N	-44°53.31' W	3113	mafic / ultramaf ic	matrix-supported breccia with a striated surface and 4 slip zones	<i>clast:</i> Tlc / Chl ± Ttn <i>matrix:</i> Tlc, Amp, Srp	absent	x	x	
	V552_218 ODM218	CNRS0000000222	13°19.22' N	-44°53.28' W	3133	mafic	matrix-supported breccia with a striated surface and 6 slip zones	<i>clast:</i> Chl ± Ttn / Chl + Qz ± Sulf (Py, Po, Ccp) <i>matrix:</i> Qz + Chl + Sulf (Py, Po, Ccp)	high	x	x	x
3	V551_173 ODM173	CNRS0000000176	13°20.40' N	-44°54.03' W	3218	mafic / ultramaf ic	matrix-supported breccia with one side mostly matrix and the other containing clasts	<i>clast:</i> Tlc, Amp / Chl ± Ttn <i>matrix:</i> Tlc, Chl ± Qz ± Sulf (Py, Po)	high on matrix- supported side, mo- derate on the other	x	x	x
4	V551_195 ODM195	CNRS0000000199	13°19.51' N	-44°53.75' W	2922	mafic	clast-supported breccia	<i>clast:</i> Pl + Amp + Chl <i>matrix:</i> fine-grained with sub- mm clasts and rare Chl and Qz grains	moderate	x	x	x
6	V550_155 ODM155	CNRS0000000157	13°19.40' N	-44°54.04' W	3104	mafic	matrix-supported breccia with a striated surface and 5 slip zones	<i>clast:</i> Chl ± Ttn / Chl + Qz ± Sulf (Py) <i>matrix:</i> Qz + Chl + Sulf (Py)	high	x	x	x

1360 * Mineral abbreviations: Amp, amphibole; Ccp, chalcopyrite; Chl, chlorite; Pl, plagioclase; Pmp, pumpellyite; Px, pyroxene; Py, pyrite; Po, pyrrhotite; Qz, quartz; Srp, serpentine; Ttn, titanite; Sulf, sulfide;
 1361 Tlc, talc

1362

1363

1364

1365

1366

1367

1368

1369

1370 **Table 2.** Major and selected trace element whole-rock analyses of mafic and mixed mafic-ultramafic breccias from the detachment fault
 1371 surface (see Table S1 for full analyses).
 1372

Nature Degree of silicification		Basaltic clast Qz free	Mafic Moderately Si	Mafic Highly Si	Mafic Highly Si	Mafic Highly Si	Mafic Highly Si	Mixed Qz free	Mixed Qz free	Mixed Qz free	Mixed Moderately Si	Mixed Moderately Si	Mixed Moderately Si
Sample		ODM115	ODM195	ODM218a	ODM218b	ODM218 wr	ODM155	ODM217a	ODM217b	ODM217 wr	ODM173a	ODM173b	ODM173 wr
SiO ₂	wt.%	51.81	49.16	84.35	62.40	65.72	79.27	49.41	55.08	48.90	55.64	57.37	68.25
Al ₂ O ₃	wt.%	13.76	13.05	2.69	4.12	3.78	2.43	5.46	2.26	5.25	9.05	1.50	5.18
Fe ₂ O ₃	wt.%	8.16	10.76	6.30	19.97	17.09	9.47	11.25	8.07	12.50	13.79	10.04	11.07
MnO	wt.%	0.16	0.22	0.06	0.08	0.08	0.06	0.33	0.39	0.45	0.11	0.07	0.07
MgO	wt.%	6.08	11.88	2.43	4.33	4.08	2.10	22.70	22.93	21.30	11.24	20.49	8.18
CaO	wt.%	11.27	4.57	0.28	0.48	0.30	0.28	4.32	6.72	5.33	0.24	0.09	0.17
Na ₂ O	wt.%	3.78	1.23	< D.L.	0.11	0.07	0.05	0.22	0.20	0.24	0.29	0.28	0.17
K ₂ O	wt.%	0.09	0.04	< D.L.	< D.L.	< D.L.	0.02	0.03	0.03	0.04	0.04	0.03	0.03
TiO ₂	wt.%	1.37	0.65	0.17	0.27	0.26	0.15	0.42	0.12	0.40	0.49	< D.L.	0.26
P ₂ O ₅	wt.%	0.16	< D.L.	< D.L.	< D.L.	< D.L.	< D.L.	0.06	< D.L.	0.05	0.05	< D.L.	0.04
PF	wt.%	3.03	7.22	3.44	7.72	7.77	6.67	6.39	4.86	6.52	9.18	10.28	6.24
Total	wt.%	99.65	98.79	99.71	99.48	99.14	100.49	100.60	100.67	100.97	100.11	100.15	99.66
Mg #		59.61	68.62	43.26	30.05	32.11	30.51	80.00	84.91	77.15	61.74	80.18	59.41
FeO	wt.%	4.74	5.54	5.50	14.46	12.49	3.51	8.01	5.61	8.85	7.45	5.75	6.14
S	wt.%	0.04	0.04	1.04	7.68	6.21	4.75	0.02	0.03	0.02	0.66	0.69	1.98
Cr	ppm	308.50	349.30	293.70	590.40	525.60	303.30	1826.00	1895.00	2070.00	934.30	3319.00	1214.00
Cu	ppm	66.84	11.68	87.36	564.10	697.30	19.05	874.20	450.80	1540.00	504.20	1609.00	605.20
Ni	ppm	112.80	126.40	140.40	492.70	385.90	190.70	1080.00	1180.00	1064.00	429.50	1609.00	710.70
Zn	ppm	60.02	105.60	45.73	56.51	64.18	33.78	139.50	115.00	161.80	237.90	2947.00	379.70

<D.L.: lower than detection limit. Qz: quartz; Highly Si: highly silicified

1373
 1374
 1375 **Table 3.** Microthermometric measurements in fluid inclusions and Raman spectroscopy results.
 1376

Sample	Quartz location	Nb	Th (°C)			Salinity (wt.% NaCl eq.)			Gases other than H ₂ O in fluid inclusions, analyzed by Raman spectroscopy
			Range	Average	SD	Range	Average	SD	
ODM195	Matrix	19	149-218	182	16	4.3-5.9	5.2	0.5	12 FI studied – no gas detected
ODM155	All	24	183-322	263	25	3.5-5.9	4.8	0.3	17 FI studied – 2 with CO ₂ only
	- Matrix	14	197-286	258	24	4.3-5.9	4.9	0.4	
	- Clasts	10	183-322	271	23	3.5-5.3	4.7	0.3	
ODM218b	All	30	260-336	318	9	4.8-10.2	7.6	0.9	28 FI studied – 7 with H ₂ only. 6 with H ₂ +CO ₂ . 2 with H ₂ +CH ₄
	- Matrix	6	260-329	305	25	6.2-6.9	6.4	0.3	
	- Clasts	24	310-336	321	5	4.8-10.2	7.9	0.8	
ODM218c	Matrix	36	258-348	317	12	2.4-6.2	4.3	0.8	21 FI studied – 11 with H ₂ only. 1 with H ₂ +CO ₂ . 3 with H ₂ +CH ₄ . 2 with H ₂ +CO ₂ +CH ₄ . 4 with H ₂ +CO ₂ +CH ₄ +H ₂ S
ODM173	Matrix	10	153-177	176	13	3.9-6.4	4.6	0.8	6 FI studied – no gas detected

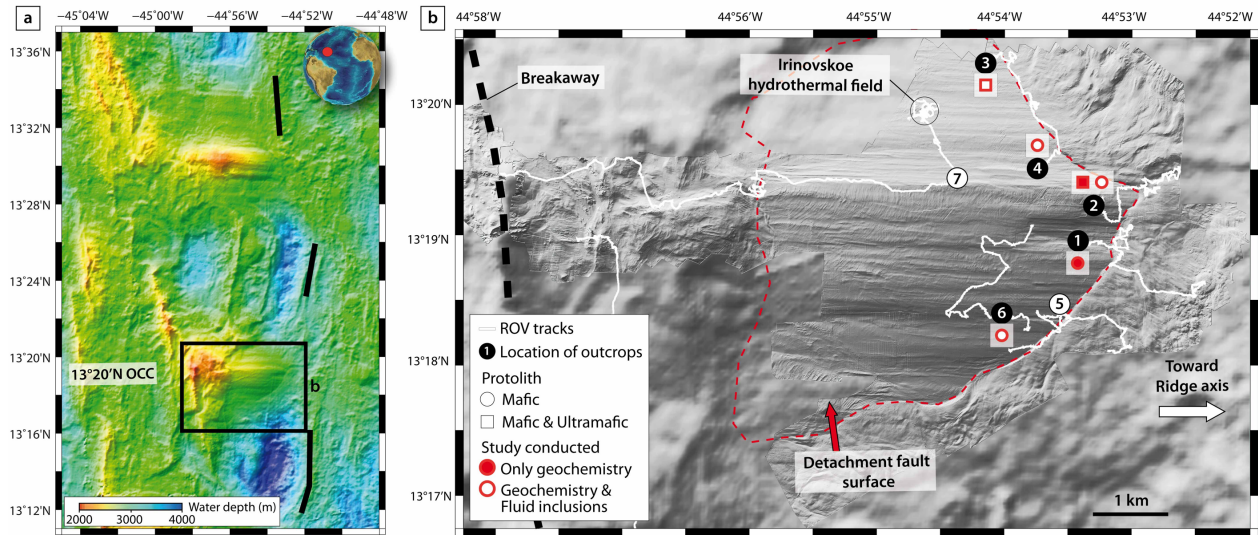
Nb: number of fluid inclusions; SD: standard deviation

1377
 1378

1379 **Figures**

1380

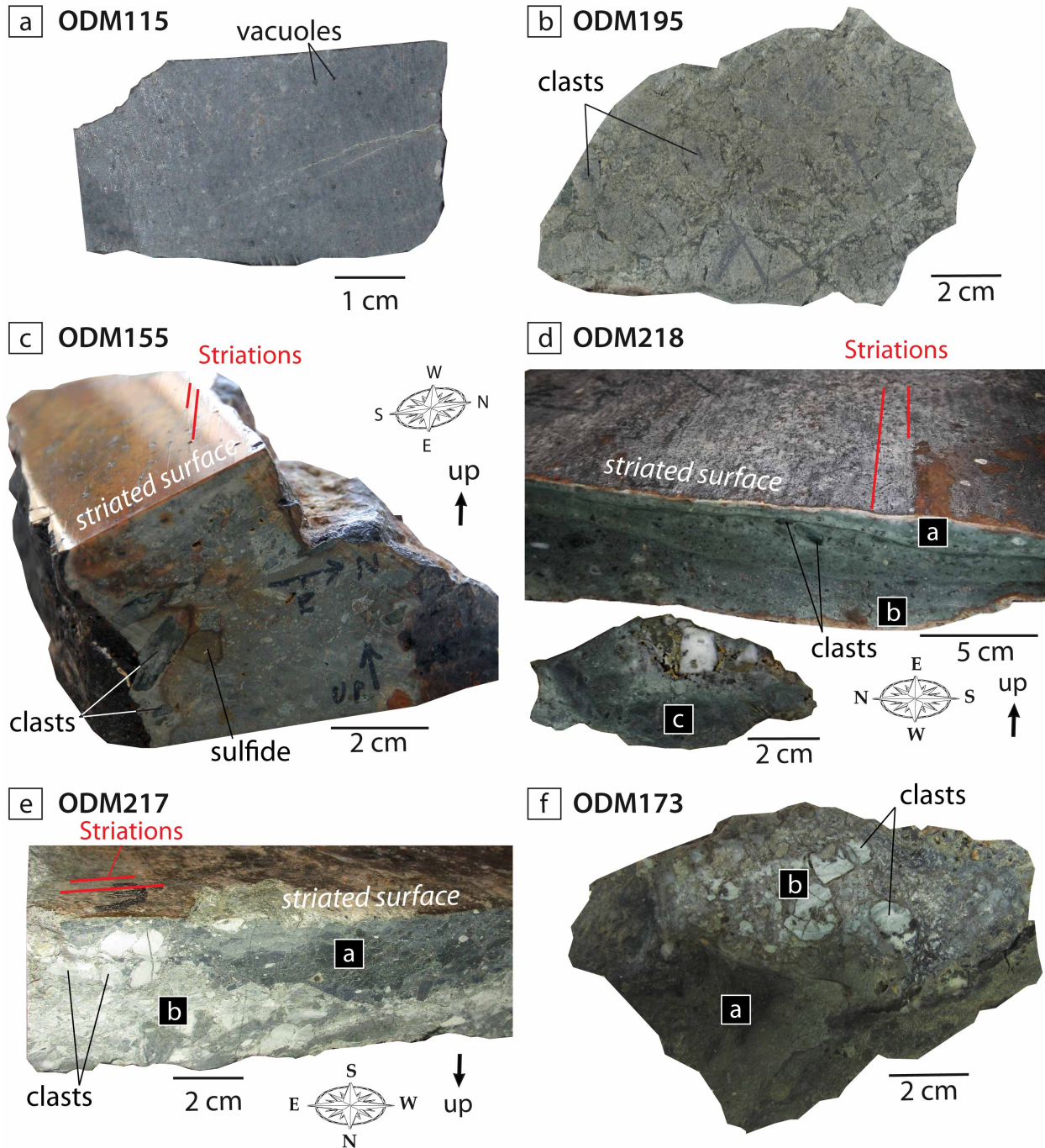
1381



1382

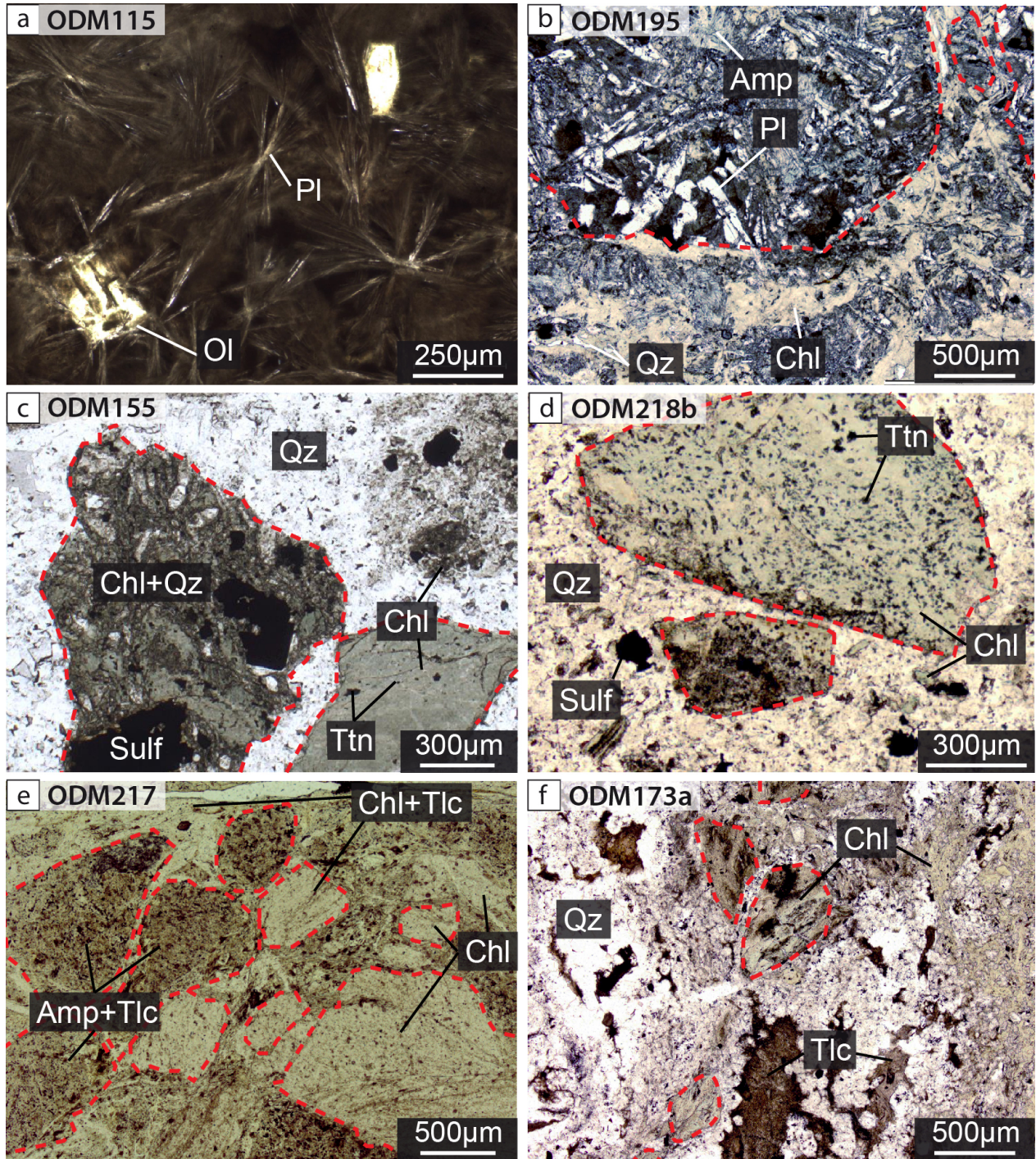
1383 **Figure 1:** (a) Multibeam bathymetry data of the 13°20'N detachment region, showing the core
1384 complex (black box) and the ridge axis (thick black lines). (b) Shaded relief microbathymetry
1385 acquired with the AUV Abyss (GEOMAR), collected during the ODEMAR cruise
1386 (<https://doi.org/10.17600/13030070>) over the 13°20'N OCC, complemented with shipboard
1387 bathymetry. White lines are tracks of ten ROV dives. Fault surface outcrops identified and sampled
1388 with the ROV are shown by a circle (see Bonnemains et al., 2017). Samples used for this study
1389 come from five of them (black numbered circles and associated red symbols, see **Table 1** for
1390 details).

1391



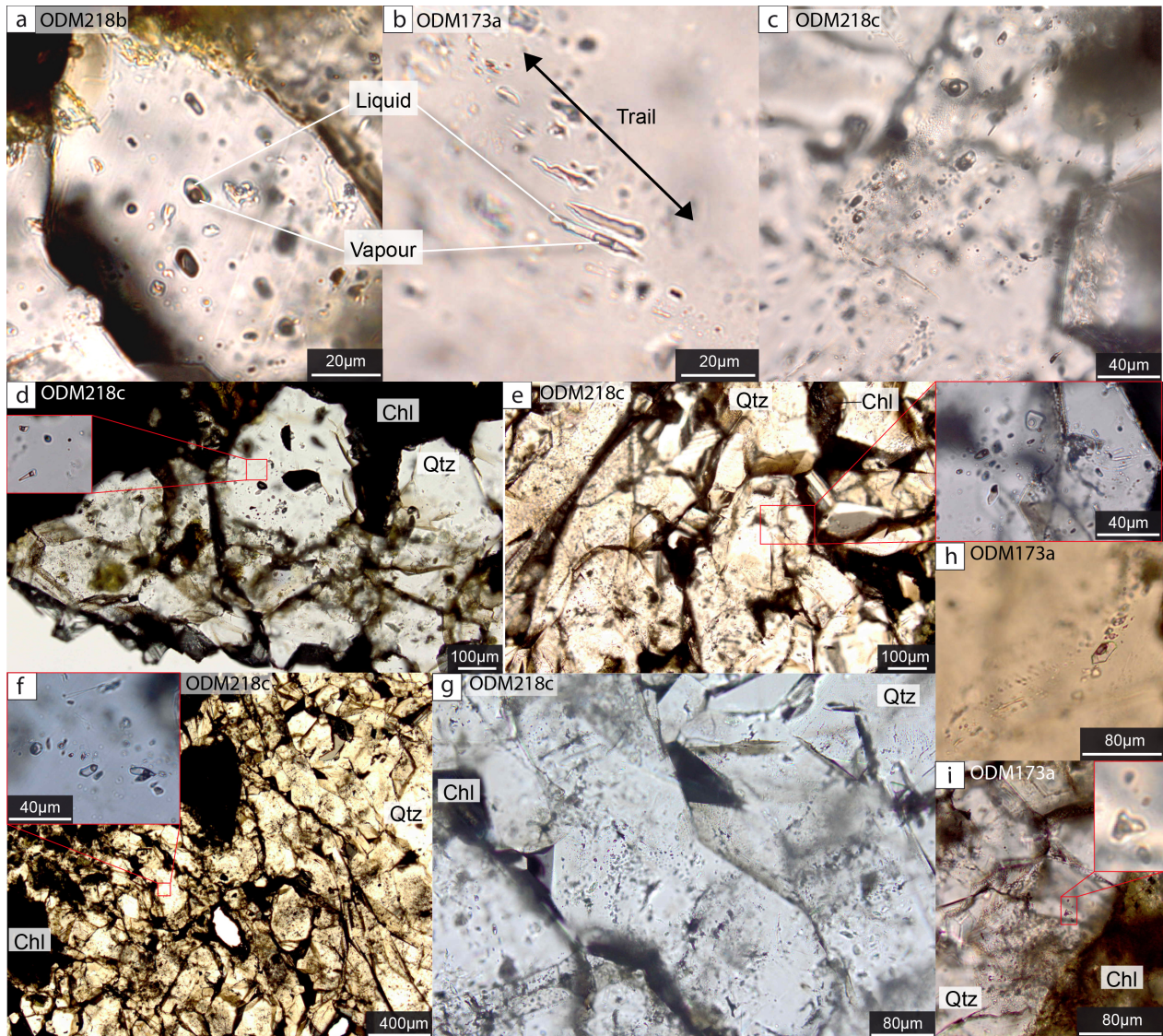
1392
 1393 **Figure 2:** Macro-photographs of the studied fault rocks. (a) Clast of metabasalt with no quartz
 1394 ODM115. (b) Moderately silicified mafic breccia ODM195. (c) Highly silicified mafic breccia
 1395 ODM155. (d) Highly silicified mafic breccia ODM218 that is distinguished in two parts
 1396 (subsamples a and b) at different distance from the striated surface (or slip plane) and a fragment
 1397 dislodged from the lower part of sample (subsample ODM218c). (e) Unsilicified mafic-ultramafic
 1398 breccia ODM217. We identify two parts based on the difference in color and mineralogical

1399 composition between these slip layers. (f) Silicified mafic-ultramafic breccia ODM173 with
1400 ODM173a richer in quartz than ODM173b. All samples were recovered in situ at the detachment
1401 fault zone.
1402



1403
 1404 **Figure 3:** Microphotographs of studied samples in plane polarized light. (a) Unsilicified mafic
 1405 clast showing basaltic texture with radiating plagioclase (Pl) laths and dendritic olivine (Ol)
 1406 crystals. (b) Moderately silicified mafic breccia contains clasts displaying a doleritic texture, made
 1407 of amphibole (Amp) + plagioclase ± chlorite (Chl), surrounded by a matrix consisting of crushed
 1408 clasts mixed with chlorite and quartz (Qz). (c, d) Highly silicified mafic breccias containing clasts

1409 of chlorite ± titanite (Ttn) and chlorite ± quartz ± sulfide (Sulf), in a matrix mainly composed of
 1410 quartz and minor chlorite and sulfide. In one of the clasts (c), the doleritic texture is still visible.
 1411 (e) Unsilicified and (f) silicified mafic-ultramafic breccias containing both mafic (made of chlorite
 1412 ± titanite) and ultramafic (made of talc, Tlc, and amphibole) clasts embedded in a matrix composed
 1413 of chlorite and talc, in addition to quartz for sample (f). (e) corresponds to zone a in Figure 2f.
 1414 Clasts are delimited by red dotted lines.
 1415



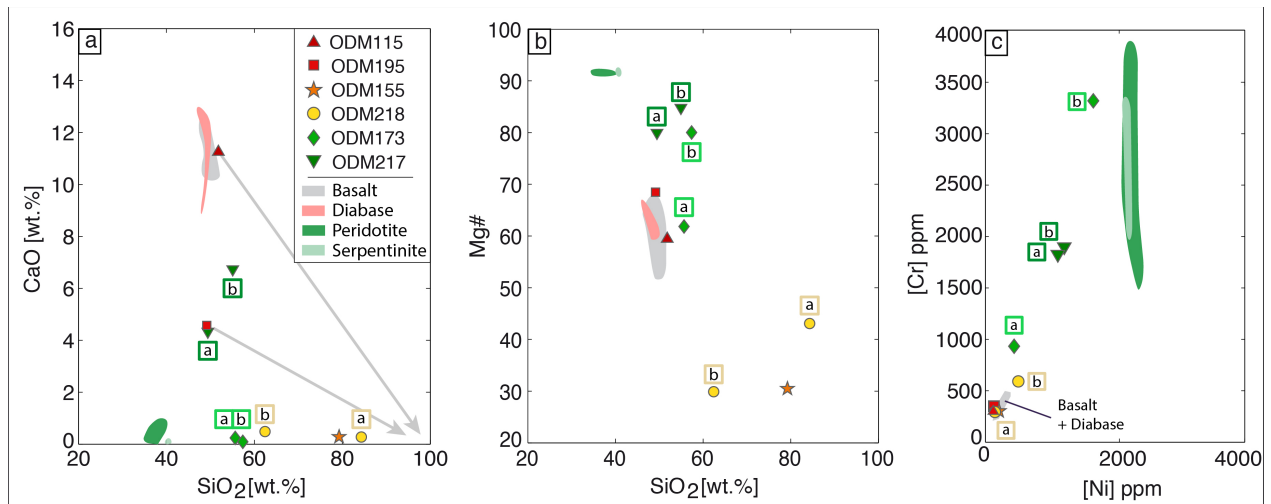
1416
 1417 **Figure 4:** Microphotographs of representative two-phase (liquid and vapor) fluid inclusions in
 1418 quartz grains. Clustered fluid inclusions with similar vapor/liquid ratios are considered as primary
 1419 (a, d; e; i); fluid inclusions organized in trails are considered as secondary inclusions (b, c, f, g, h).

1420 Note that most trails are intragrain trails, restricted to one quartz grain, while only few trails
 1421 crosscut several quartz grain boundaries (g). Qtz: quartz; Chl: chlorite.

1422

1423

1424



1425

1426 **Figure 5:** Bulk rock geochemistry. SiO₂ versus (a) CaO and (b) Mg# ($=Mg/(Mg+Fe)*100$);

1427 brecciated rocks show a relative decrease in both CaO and Mg# with increasing degree of

1428 silicification; mixed mafic-ultramafic breccias (green symbols) tend to be higher in magnesium at

1429 a given silica content; grey arrows: trend of passive depletion of CaO in breccias due to silica

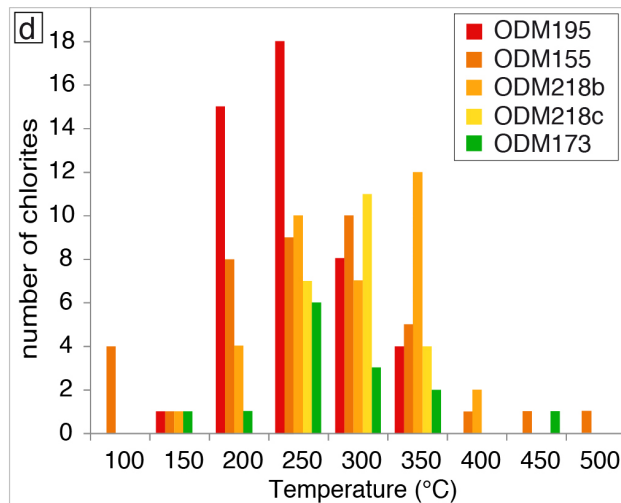
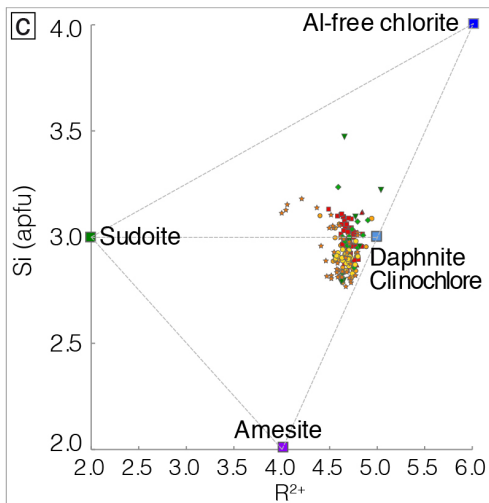
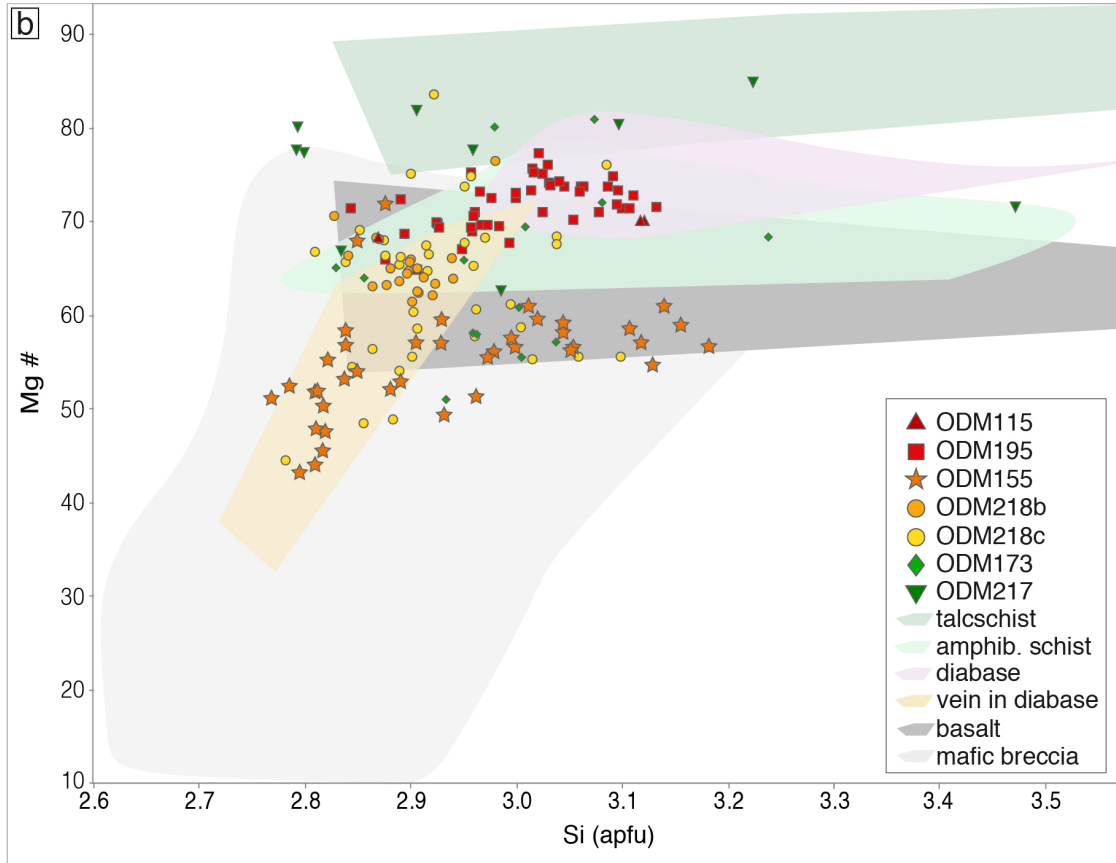
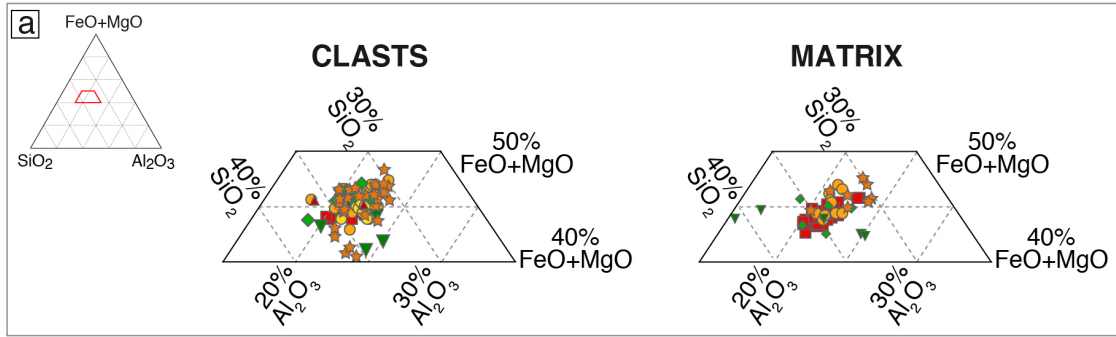
1430 addition; Mg# will not be affected by silica addition. (c) Cr vs Ni; mixed breccias tend to be

1431 enriched in nickel and chromium compared with purely mafic breccias. Data for basalts and

1432 diabases from the 13°20'N OCC (Wilson et al., 2013) and for peridotites from the 15°20'N Fracture

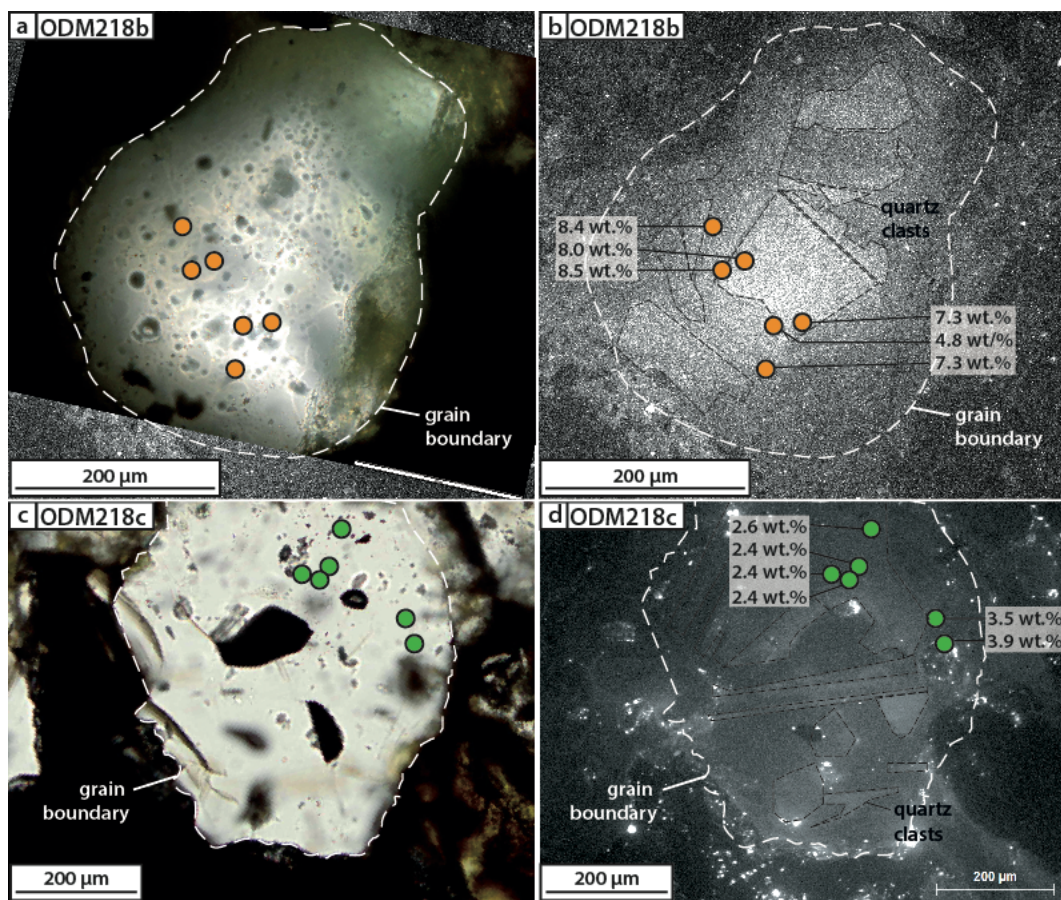
1433 Zone (Godard et al., 2008; Paulick et al., 2006) are shown for comparison. Data are available in

1434 Table 2.



1436 **Figure 6:** Chlorite composition in clasts and matrices (a) in a FeO+MgO, Al₂O₃, SiO₂ ternary
 1437 diagram; (b) Mg# versus Si (atoms per formula unit); chlorite compositions are compared to
 1438 other oceanic chlorites from ultramafic rocks (talcschists from 15°45'N: Escartín et al., 2003, and
 1439 south of Atlantis Massif: Boschi et al., 2006); mixed mafic-ultramafic amphibolite schists
 1440 (Escartín et al., 2003); mafic rocks (diabases: Escartín et al., 2003; basalts from MAR: Humphris
 1441 & Thompson, 1978, and from MARK: Gillis and Thompson, 1993); altered mafic rocks
 1442 (silicified breccias from MARK: Delaney et al., 1987; Saccocia and Gillis, 1995; chlorite-quartz
 1443 vein in diabase, Atlantis Massif: Castelain et al., 2014); (c) Si versus R²⁺ diagram with chlorite
 1444 endmembers; (d) Histogram of chlorite crystallization temperatures estimated using the semi-
 1445 empirical geothermometer of Bourdelle et al. (2013). Chlorite analyses and calculated
 1446 temperatures are available in Tables S2 and S4.

1447

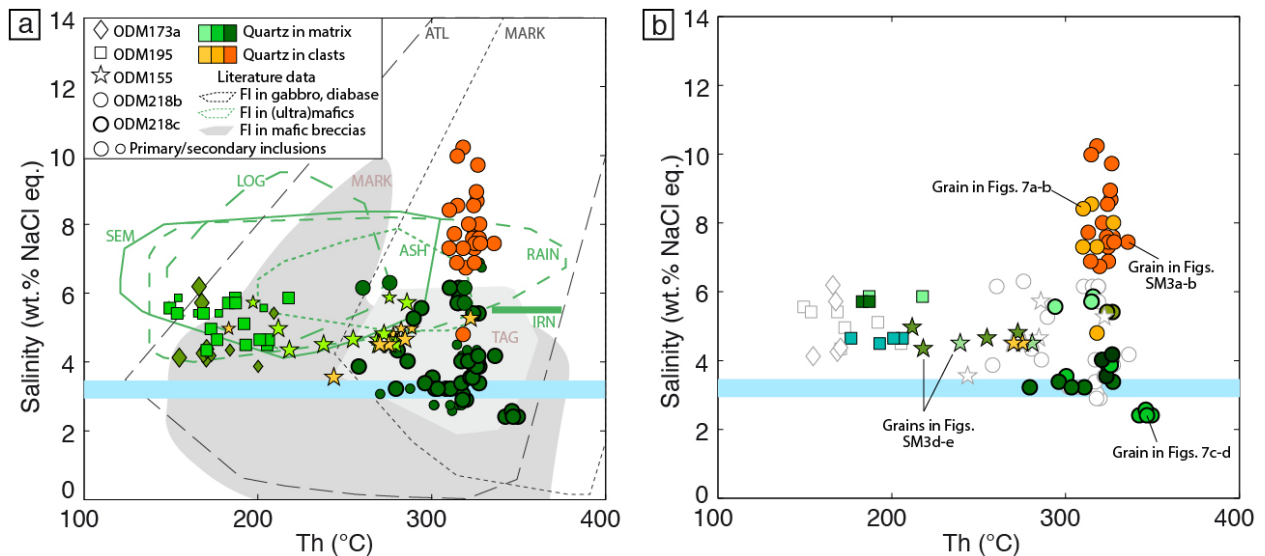


1448

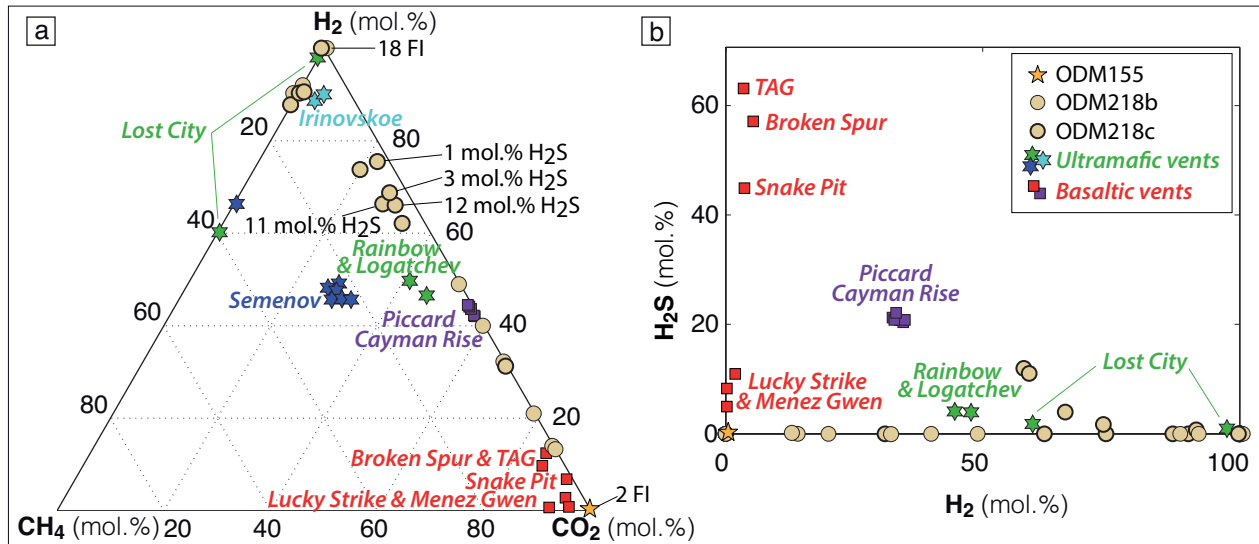
1449 **Figure 7:** Distribution of measured fluid inclusions in quartz grains from ODM218b (a and b,
 1450 orange dots) and ODM218c (c and d, green dots). Microphotographs under parallel nicols showing

1451 individual quartz crystals in ODM218b (a) and in ODM218c (c). SEM-cathodoluminescence image
 1452 of the same quartz grains in ODM218b (b) and in ODM218c (d); grain boundary shown by the
 1453 white dashed line; luminescence variations illustrate that quartz grains are composed of multiple
 1454 former quartz angular clasts (black dotted lines) around which quartz recrystallized in successive
 1455 generations. Quartz crystallization was obviously syntectonic, with successive steps of quartz
 1456 growth-hydrofracturing-overgrowth. The large salinity (indicated in wt.% NaCl equivalent)
 1457 variation for fluid inclusions at the quartz grain scale suggests that fluids with different salinities
 1458 were circulating (and thus trapped) during the successive episodes of quartz growth. Note that the
 1459 position of fluid inclusions was projected on the grain surface, while inclusions are in fact
 1460 distributed at various depths in the quartz grain.

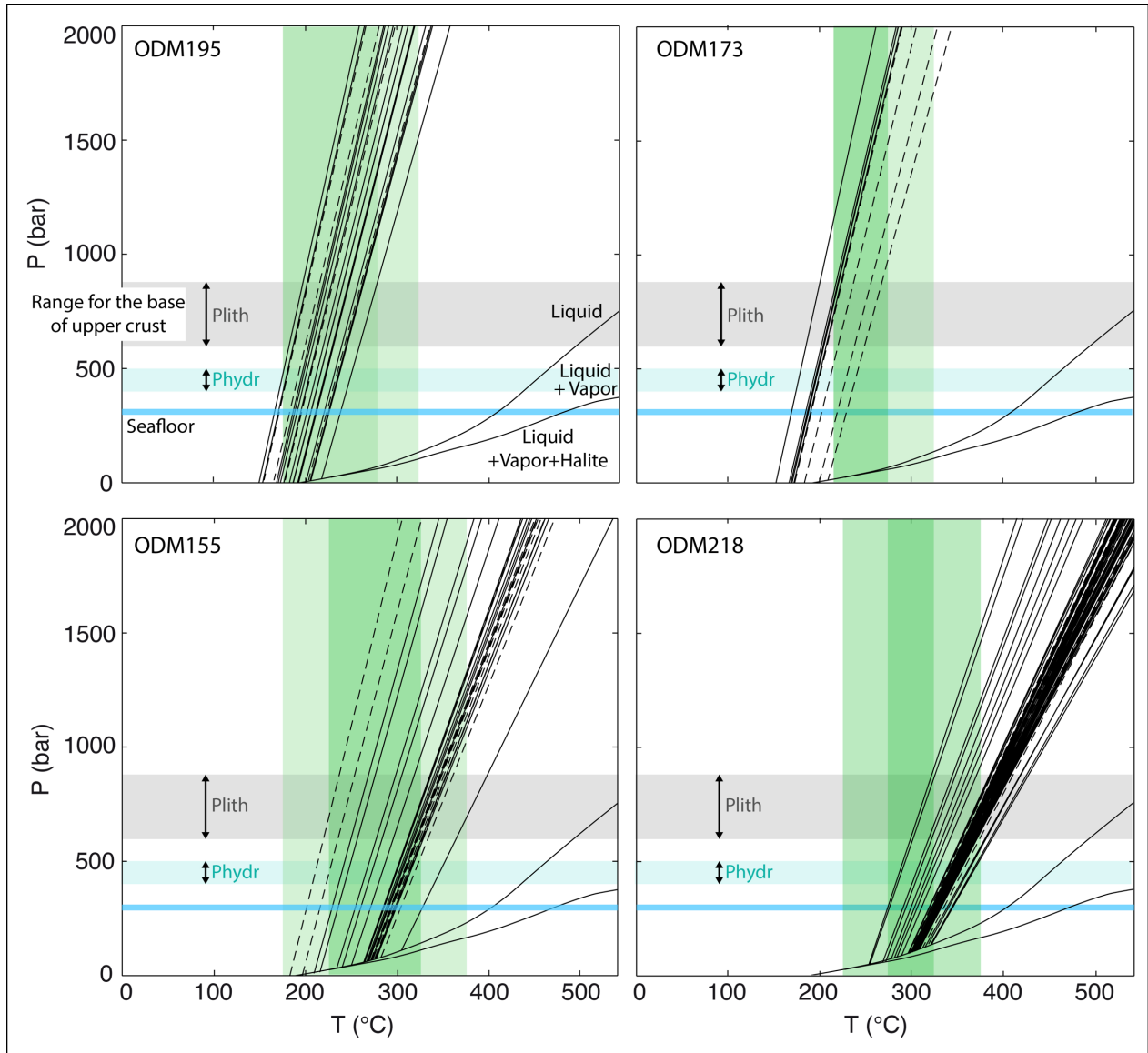
1461



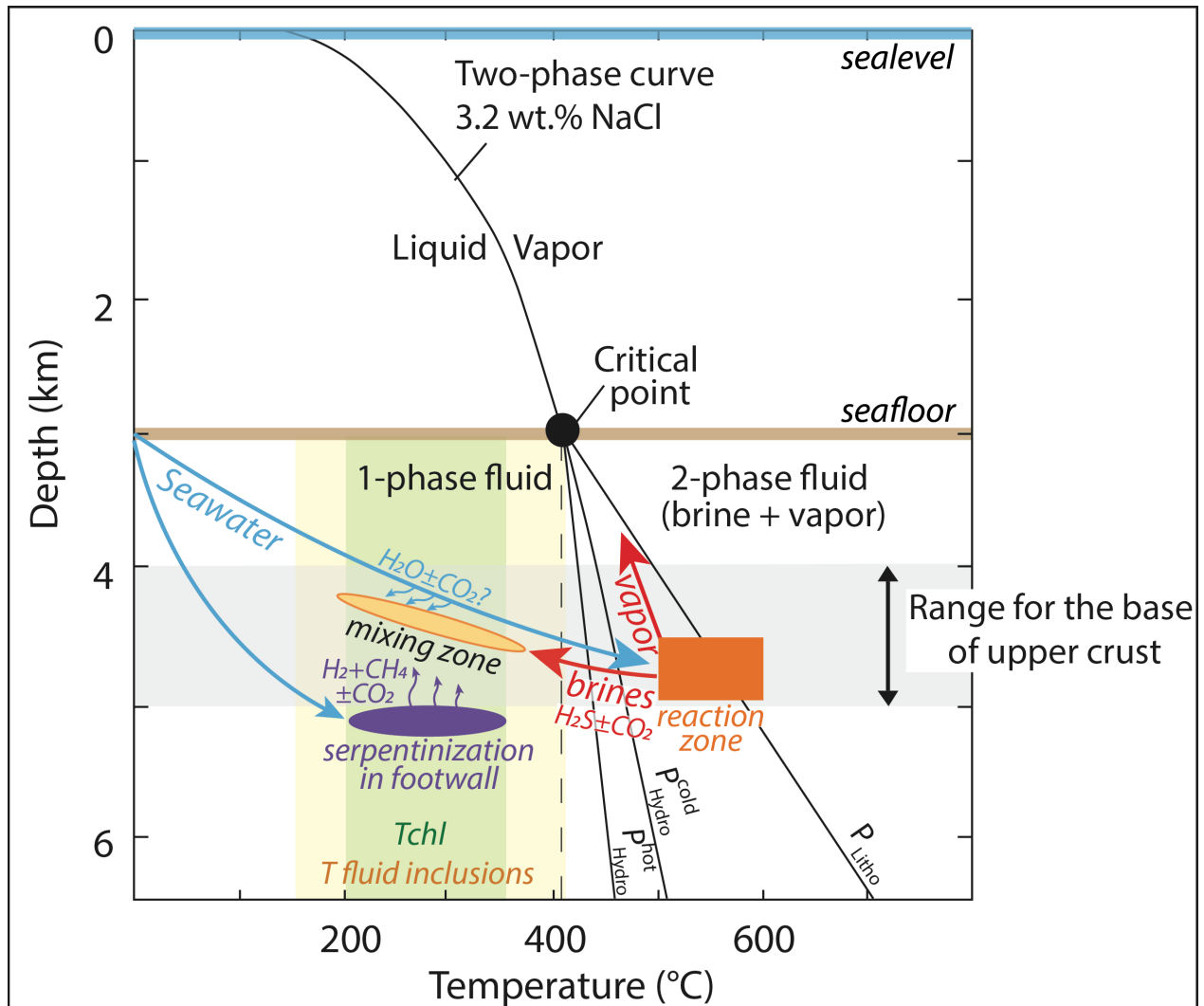
1462
 1463 **Figure 8:** Homogenization temperatures (Th) against salinity for (a) all primary and secondary
 1464 fluid inclusions; data are compared to Th and salinity ranges measured in fluid inclusions from
 1465 oceanic gabbros (MARK: Kelley and Delaney, 1987), diabases (Atlantis Massif: Castelain et al.,
 1466 2014), mafic silicified breccias from MARK (Delaney et al., 1987; Saccocia and Gillis, 1995) and
 1467 TAG (Petersen et al., 1998), detachment plane (ultra)mafic rocks hosting hydrothermal vents
 1468 (Rainbow, Logatchev, Ashadze, Semenov, Irinovskoe; Bortnikov et al., 2011, 2014, 2015;
 1469 Simonov et al., 2015); (b) Heterogeneity of inclusion Th and salinity at the sample scale for the
 1470 primary inclusions only, for clarity issues, using a similar color and symbol for inclusions in each
 1471 grain. Seawater salinity is indicated with a blue line.



1472
 1473 **Figure 9:** Molar proportion of gases (other than H₂O) analyzed by Raman spectroscopy in the
 1474 vapor phase of two-phase fluid inclusions for the two highly silicified mafic breccias ODM155 and
 1475 ODM218. All fluid inclusions are dominantly aqueous, and H₂O vapor is the dominant gas phase.
 1476 (a) Relative molar proportions of CH₄, CO₂ and H₂ in the gas phase. Gases other than H₂O were
 1477 analyzed in only 2 inclusions (over 17 analyzed) for ODM155 (and contain only CO₂ other than
 1478 H₂O vapor), in 15 inclusions over 28 analyzed for ODM218b, and in the 21 fluid inclusions
 1479 analyzed in ODM218c. 7 and 11 fluid inclusions contain only H₂ (other than H₂O vapor) in
 1480 ODM218b and ODM218c, respectively. (b) H₂ versus H₂S content in fluid inclusions (expressed
 1481 as a mol.% of CH₄-CO₂-H₂-H₂S in the vapor phase). Fluid inclusion gas compositions are
 1482 compared to data from basaltic- (Menez Gwen, Broken Spur, TAG, Snake Pit, Lucky Strike) and
 1483 ultramafic- (Rainbow, Logatchev, Lost City) derived hydrothermal vents (Fouquet et al., 2010).
 1484 Data from Semenov and Irinovskoe ultramafic-derived vents (Destrigneville et al., 2015) and from
 1485 Piccard mafic-derived vents on Cayman Rise (McDermott et al., 2018) are also plotted for
 1486 comparison.
 1487



1488
 1489 **Figure 10:** Range of P-T conditions for silicification of brecciated rocks within the detachment
 1490 plane. P-T isochoric relationships for fluid inclusions, calculated from microthermometric data
 1491 (equation of Zhang & Frantz, 1987), are plotted in black plain and dashed lines for primary and
 1492 secondary fluid inclusions respectively. The liquid-vapor and liquid-vapor-halite curves are from
 1493 Sourirajan and Kennedy (1962). Pressure at the seafloor is indicated with a blue line, and the range
 1494 of lithostatic and hydrostatic fluid pressures at the base of the hangingwall upper crust (1–2 km
 1495 thick) is in grey and blue respectively (assuming seawater and rock densities of 1025 and 3000
 1496 kg/m³ respectively). The temperature range of chlorite crystallization during silicification,
 1497 calculated from chlorite composition (geothermometer of Bourdelle et al., 2013), is in green (darker
 1498 green for higher number of chlorites; see Figure 6d).

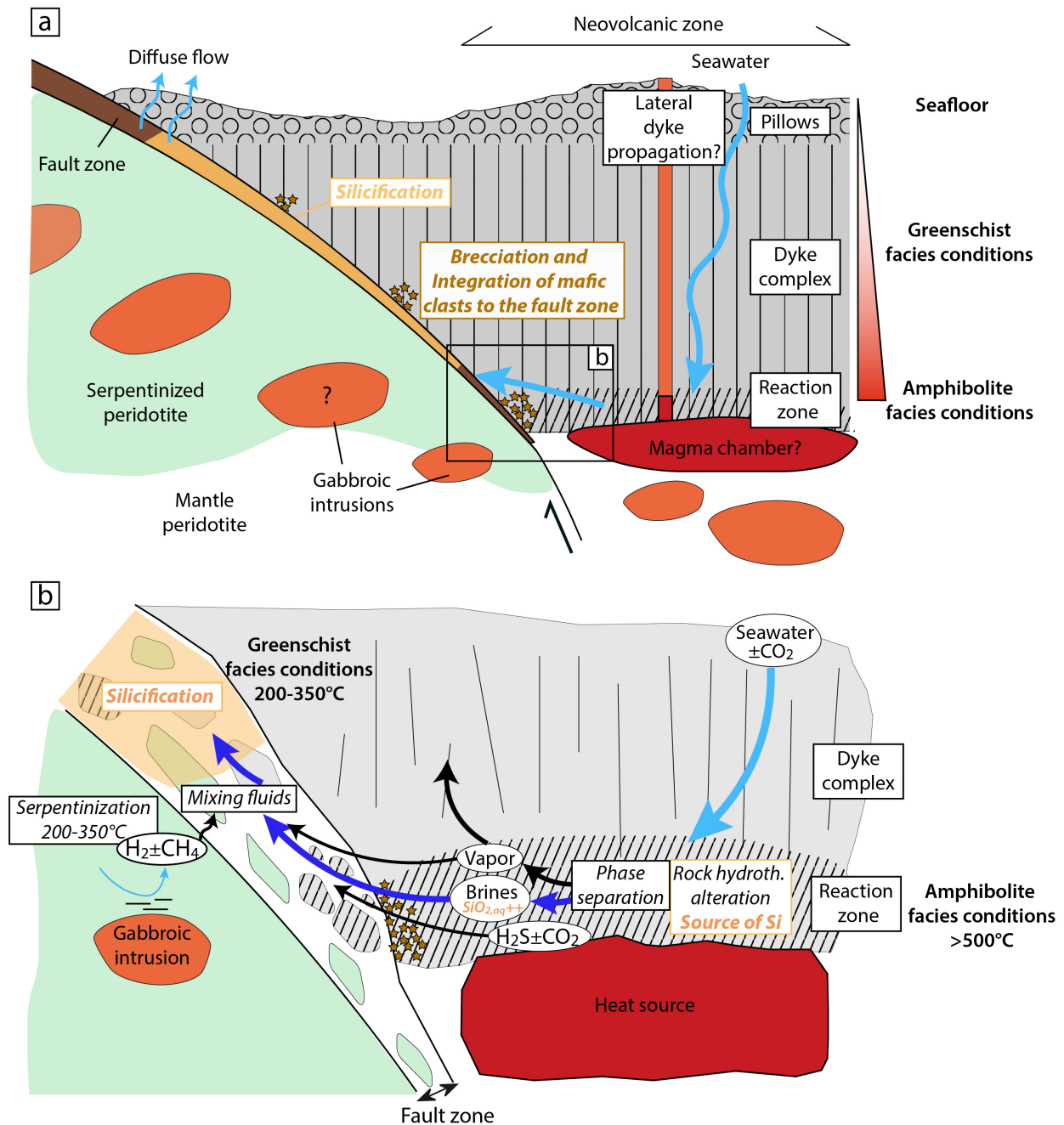


1499
 1500 **Figure 11:** P-T-depth relationships in the NaCl-H₂O system for a hydrothermal seawater-like
 1501 solution (3.2 wt.% NaCl). The two-phase curve separates the one-phase liquid field from the two-
 1502 phase liquid+vapor field (Sourirajan & Kennedy, 1962). Temperature-depth relationship for the
 1503 two-phase curve beyond the critical point (407°C, 298 bars, black dot) is calculated for both
 1504 lithostatic and hydrostatic fluid pressures. Cold and hot hydrostatic pressure gradients (100 and 50
 1505 bar/km respectively) were taken from Coumou et al. (2009) and Castelain et al. (2014). Seawater
 1506 (blue arrow) infiltrating the hangingwall crust (1-2 km thick) may undergo phase separation, at
 1507 least when reaching the reaction zone (orange rectangle) at the base of the crust (diabase clasts
 1508 suggest temperature >500 °C). While part of vapor phases can migrate upwards into the crust,
 1509 higher density brines are likely released in the detachment plane upon diabase brecciation (red
 1510 arrows). They are mixed in variable amounts with fluids derived from footwall serpentinization

1511 (purple arrows) and potentially small amounts of seawater circulating in hangingwall basalts (blue
 1512 arrows). Temperature ranges of chlorite formation (light green zone) and homogenization of fluid
 1513 inclusions (light yellow zone) are reported (see Figures 6d, 8, 10 and text for details).

1514

1515



1516

1517 **Figure 12:** Schematic interpretation of fluid circulation along the 13°20'N OCC. (a) The
 1518 hangingwall corresponds to a section of upper crust while the footwall progressively exhumates

1519 material from deeper levels of the lithosphere (mantle-derived peridotites with gabbroic intrusions).
1520 A reaction zone at the base of the upper crust is generated by a heat source located beneath the
1521 neovolcanic zone. The fault zone thickens during exhumation, due to the integration of hangingwall
1522 material. (b) Close up of the reaction zone close to the heat source. Seawater percolates down to
1523 the reaction zone where increased pressure and temperature generate phase separation into brine
1524 and vapor phases. Brines are enriched in silica released by hydrothermal alteration of the mafic
1525 rocks. While most of the vapor phases escape towards the surface, brines (and a small portion of
1526 vapor phases) are integrated into the fault zone during the overplating and mix with (small amounts
1527 of) hydrogen-bearing fluids generated by serpentinization of the footwall. Reaction of hydrogen
1528 with CO₂ either dissolved in seawater or released by magmatic activity results in the formation of
1529 methane. As the fluid ascends and cools down, the solubility of silica strongly decreases resulting
1530 in precipitation of quartz that entraps the fluid inclusions.

1531

1532

1533

Geochemistry, Geophysics, Geosystems

1534

Supporting Information for

1535

Fluid circulation along an oceanic detachment fault: insights from fluid

1536

inclusions in silicified brecciated fault rocks (Mid-Atlantic Ridge at 13°20'N)

1537

A. Verlaguet^{1*}, D. Bonnemains², C. Mével², J. Escartín^{2,3}, M. Andreani⁴, F.

1538

Bourdelle⁵, M-C. Boiron⁶, V. Chavagnac⁷

1539

¹ Sorbonne Université, CNRS-INSU, Institut des Sciences de la Terre, IStEP UMR 7193, F 75005 Paris,

1540

France

1541

² Université de Paris, Institut de Physique du Globe, CNRS, F-75005 Paris, France

1542

³ Laboratoire de Géologie (CNRS UMR 8538), Département de Géosciences, Ecole Normale Supérieure,

1543

PSL University, F-75005 Paris, France

1544

⁴ Laboratoire de Géologie LGL-TPE, Université de Lyon, UCBL, ENSL, CNRS, Villeurbanne, 69622, France

1545

⁵ Univ. Lille, IMT Lille Douai, Univ. Artois, Yncrea Hauts-de-France, ULR 4515 - LGCgE,

1546

Laboratoire de Génie Civil et géo-Environnement, F-59000 Lille, France

1547

⁶ Université de Lorraine, CNRS, GeoRessources, F-54000 Nancy, France

1548

⁷ Géosciences Environnement Toulouse (GET), Université Paul Sabatier Toulouse 3, CNRS UMR 5563, IRD,

1549

Toulouse, France

1550

* Corresponding author: anne.verlaguet@sorbonne-universite.fr

1551

1552

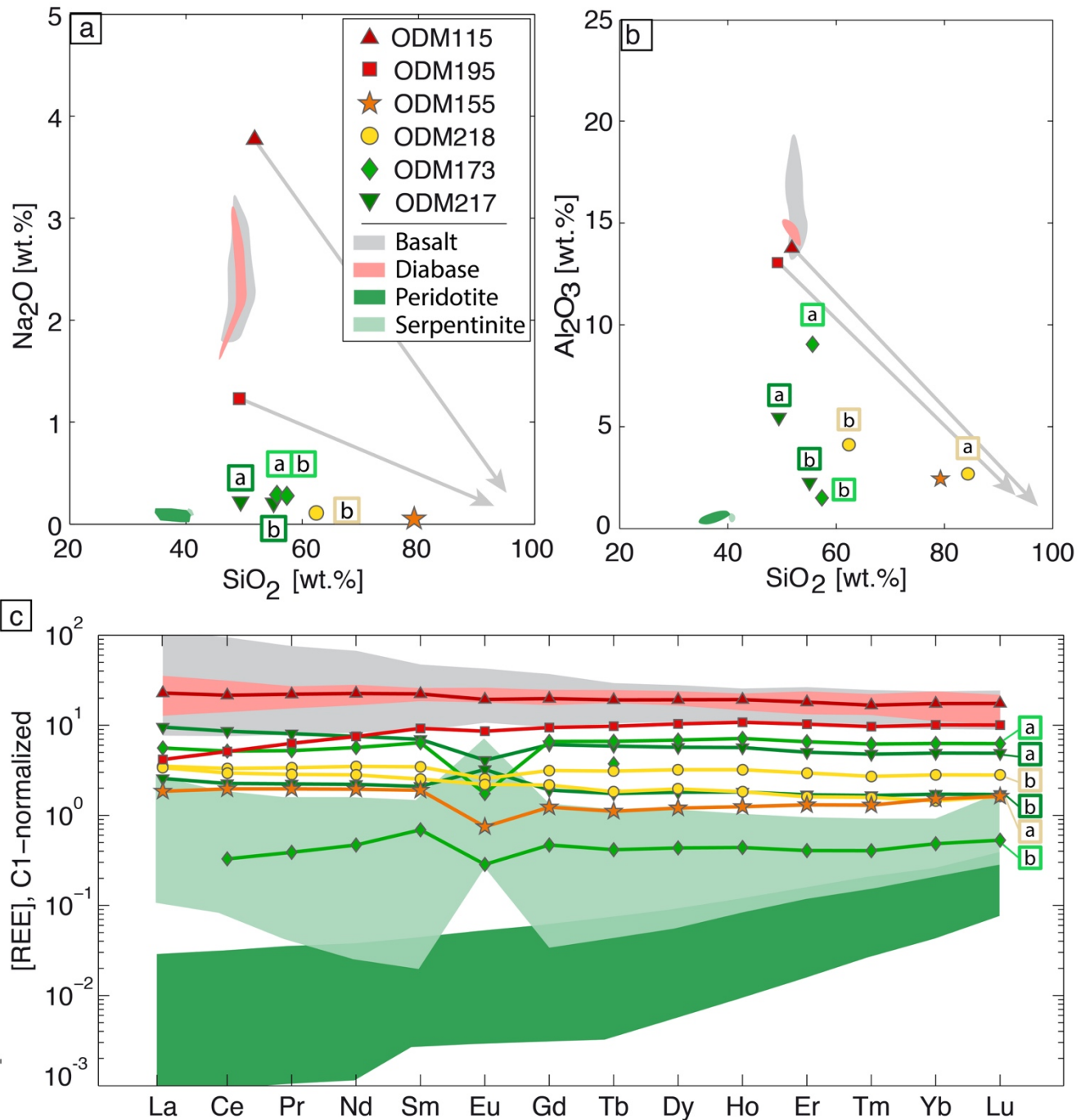
1553 **Contents of this file**

1554

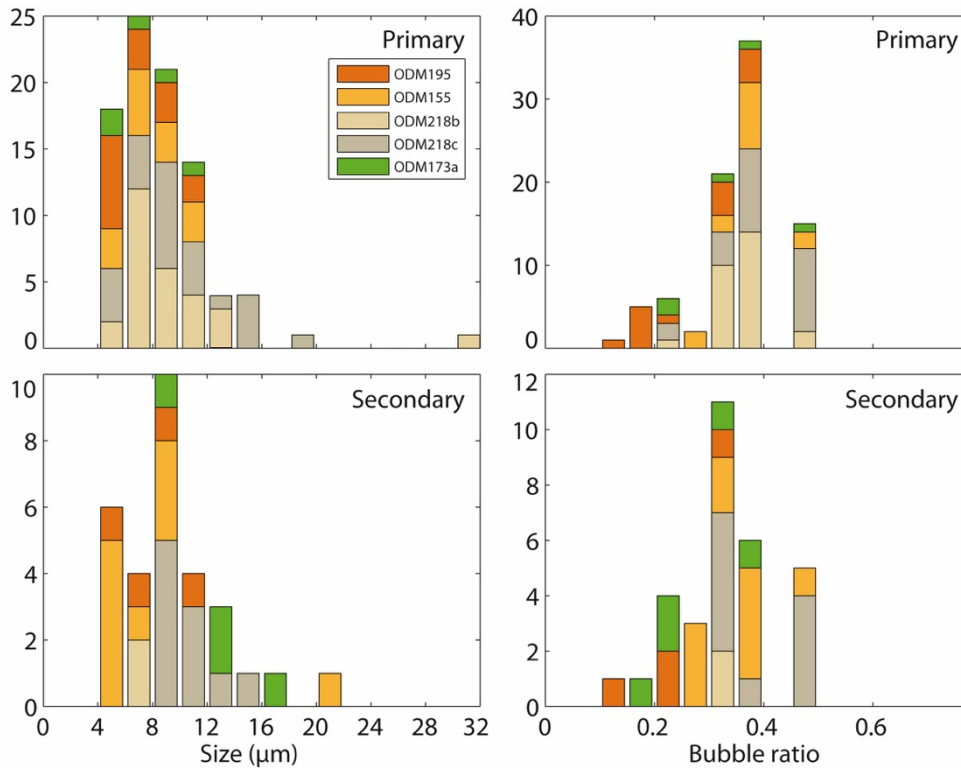
Figures S1 to S5

1555

Tables S1 to S4



1556
 1557
 1558 **Figure S1:** Bulk rock geochemistry. SiO₂ versus (a) Na₂O and (b) Al₂O₃; brecciated rocks show a
 1559 relative decrease in both Na₂O and Al₂O₃ with increasing degree of silicification; grey arrows:
 1560 trend of passive depletion of Na₂O and Al₂O₃ in breccias due to silica addition. (c) Rare earth
 1561 element (REE) content of brecciated rocks normalized to chondrite. Compositions are compared
 1562 to data for basalts and diabases from the 13°20'N OCC (Wilson et al., 2013) and for peridotites
 1563 from the 15°20'N Fracture Zone (Godard et al., 2008; Paulick et al., 2006).



1564

1565

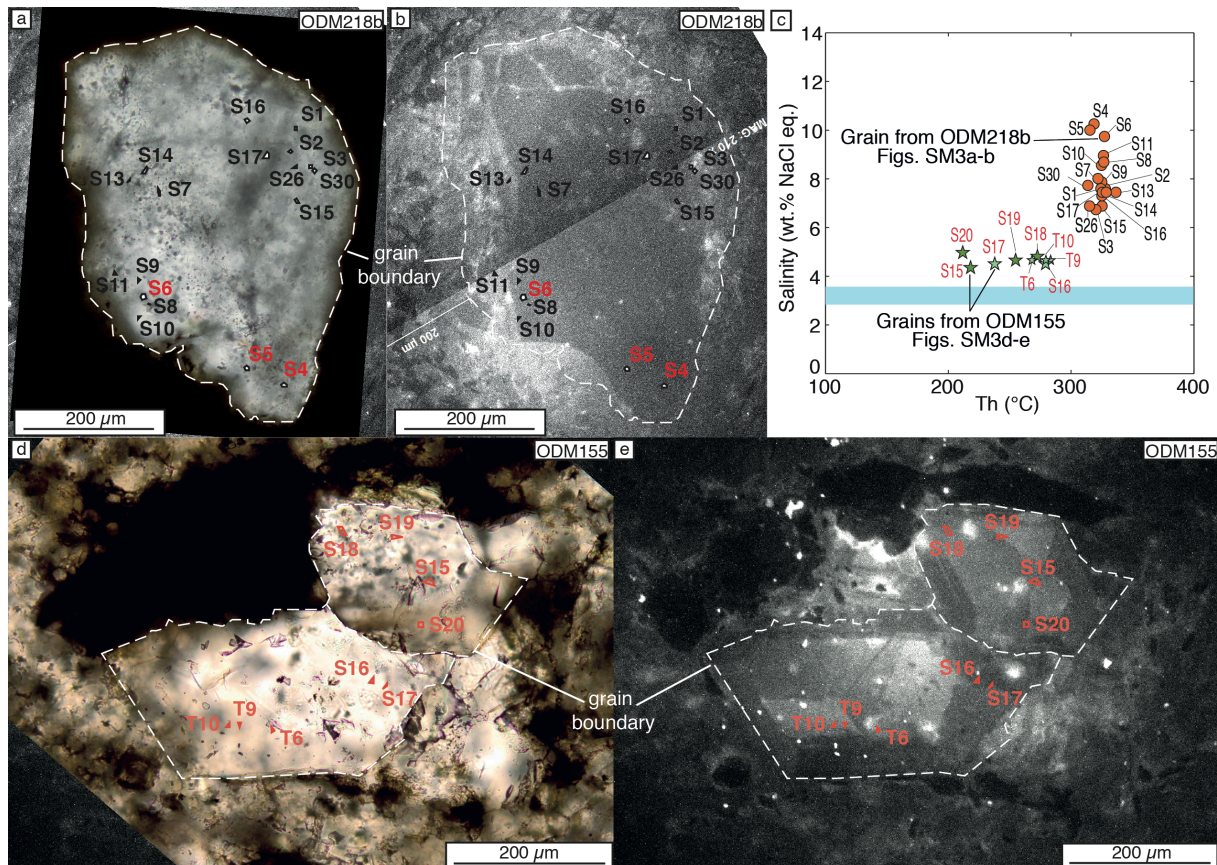
1566 **Figure S2:** Size distribution (left) and bubble/inclusion volumetric ratio (right) histograms for primary (top)
 1567 and secondary (bottom) fluid inclusions. Vertical axis is frequency.

1568

1569

1570

1571



1572

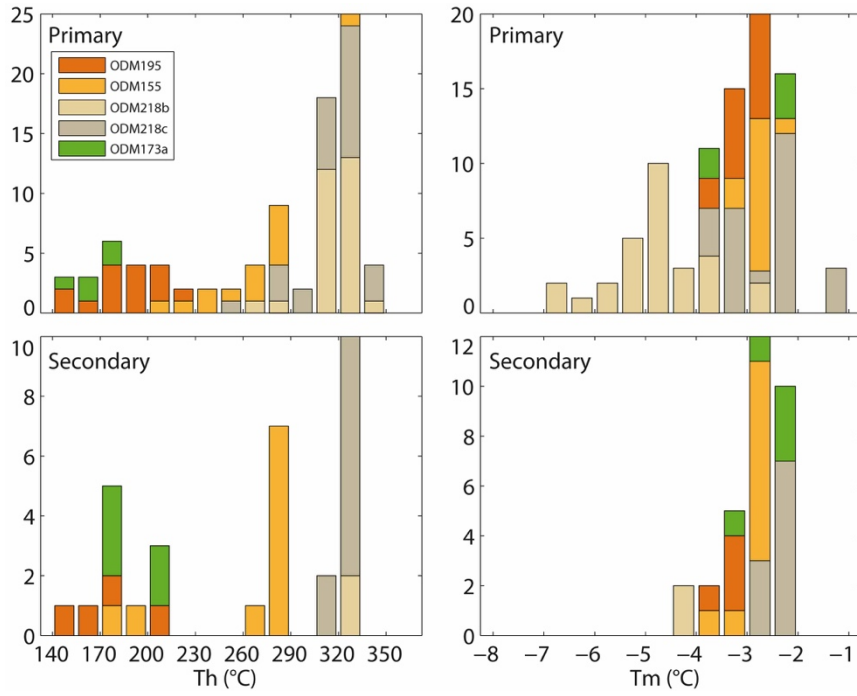
1573

1574 **Figure S3:** Location of analyzed fluid inclusions in quartz grains from ODM218b (a and b, orange dots in c)
 1575 and ODM155 (d and e, green stars in c). Microphotographs under parallel nicols showing individual quartz
 1576 crystals in ODM218b (a) and in ODM155 (d). SEM-cathodoluminescence images of the same quartz grains
 1577 in ODM218b (b) and in ODM155 (e); grain boundaries are shown by the white dashed line; luminescence
 1578 variations illustrate that quartz grains are composed of multiple former quartz angular clasts around which
 1579 quartz recrystallized in successive generations. Quartz crystallization was unequivocally syntectonic, with
 1580 successive steps of quartz growth-hydrofracturing-overgrowth. (c) Homogenization temperatures (Th)
 1581 against salinity (indicated in wt.% NaCl equivalent) for primary (big symbols) and secondary (small symbols)
 1582 fluid inclusions from quartz grains in ODM218b (a, b) and ODM155 (d, e). Seawater salinity is indicated
 1583 with a blue line. The large salinity variation measured from fluid inclusions within individual grains
 1584 indicates entrapment of fluids with varying salinities during successive quartz growth episodes. Note that
 1585 the position of fluid inclusions was projected on the grain surface, while inclusions are in fact distributed
 1586 at various depths within the quartz grain. In ODM218b (a, b) inclusions in red are those very close to the
 1587 thick section surface.

1588

1589

1590



1591

1592

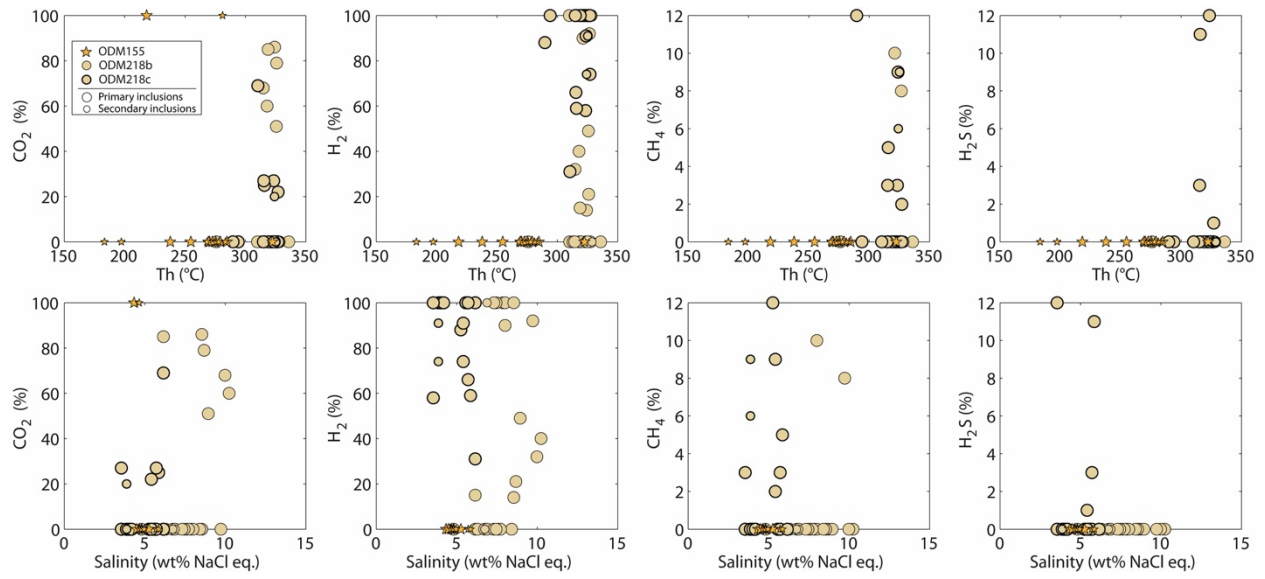
1593 **Figure S4:** Histogram showing the distribution of homogenization temperatures (Th, left) and ice melting
1594 temperatures ($T_{m_{ice}}$, right) for primary (top) and secondary (bottom) fluid inclusions. Vertical axis is
1595 frequency.

1596

1597

1598

1599



1600

1601 **Figure S5:** Gas content (mol.% of gas other than H₂O in the gas bubble) versus homogenization
 1602 temperature (Th) and salinity.

1603 **Table S1. Full chemical analyses of the selected samples.**

1604

Nature Degree of silicification Sample	Basaltic clast Qz free ODM115	Mafic Moderately Si ODM195	Mafic Highly Si ODM218a	Mafic Highly Si ODM218b	Mafic Highly Si ODM218 wr	Mafic Highly Si ODM155	Mixed Qz free ODM217a	Mixed Qz free ODM217b	Mixed Qz free ODM217 wr	Mixed Moderately Si ODM173a	Mixed Moderately Si ODM173b	Mixed Moderately Si ODM173 wr
SiO₂ wt.%	51.81	49.16	84.35	62.40	65.72	79.27	49.41	55.08	48.90	55.64	57.37	68.25
Al₂O₃ wt.%	13.76	13.05	2.69	4.12	3.78	2.43	5.46	2.26	5.25	9.05	1.50	5.18
Fe₂O₃ wt.%	8.16	10.76	6.30	19.97	17.09	9.47	11.25	8.07	12.50	13.79	10.04	11.07
MnO wt.%	0.16	0.22	0.06	0.08	0.08	0.06	0.33	0.39	0.45	0.11	0.07	0.07
MgO wt.%	6.08	11.88	2.43	4.33	4.08	2.10	22.70	22.93	21.30	11.24	20.49	8.18
CaO wt.%	11.27	4.57	0.28	0.48	0.30	0.28	4.32	6.72	5.33	0.24	0.09	0.17
Na₂O wt.%	3.78	1.23	< D.L.	0.11	0.07	0.05	0.22	0.20	0.24	0.29	0.28	0.17
K₂O wt.%	0.09	0.04	< D.L.	< D.L.	< D.L.	0.02	0.03	0.03	0.04	0.04	0.03	0.03
TiO₂ wt.%	1.37	0.65	0.17	0.27	0.26	0.15	0.42	0.12	0.40	0.49	< D.L.	0.26
P₂O₅ wt.%	0.16	< D.L.	< D.L.	< D.L.	< D.L.	< D.L.	0.06	< D.L.	0.05	0.05	< D.L.	0.04
PF wt.%	3.03	7.22	3.44	7.72	7.77	6.67	6.39	4.86	6.52	9.18	10.28	6.24
Total wt.%	99.65	98.79	99.71	99.48	99.14	100.49	100.60	100.67	100.97	100.11	100.15	99.66
Mg #	59.61	68.62	43.26	30.05	32.11	30.51	80.00	84.91	77.15	61.74	80.18	59.41
FeO wt.%	4.74	5.54	5.50	14.46	12.49	3.51	8.01	5.61	8.85	7.45	5.75	6.14
H₂O total wt.%	3.22	8.13	2.49	4.20	4.32	2.62	7.05	5.55	6.95	8.93	< D.L.	5.32
S total wt.%	0.04	0.04	1.04	7.68	6.21	4.75	0.02	0.03	0.02	0.66	0.69	1.98
B ppm	5	2	2	<2	<2	4	11	8	14	8	10	7
Cl ppm	230	800	240	355	295	235	435	380	580	1520	2540	1030
Li ppm	3.7	7.6	5.4	3.0	3.3	8.3	7.4	7.6	7.4	4.3	4.2	3.1
As ppm	2.29	< D.L.	< D.L.	< D.L.	< D.L.	1.80	1.88	1.75	3.25	1.68	< D.L.	< D.L.
Ba ppm	35.37	4.17	3.00	1.67	< D.L.	2.66	< D.L.	1.69	< D.L.	1.90	< D.L.	6.75
Be ppm	0.64	< D.L.	< D.L.	< D.L.	< D.L.	< D.L.	0.46	0.60	0.50	< D.L.	< D.L.	< D.L.
Bi ppm	0.19	< D.L.	0.21	0.69	1.30	0.32	< D.L.	< D.L.	0.10	0.12	0.52	0.20
Cd ppm	0.14	< D.L.	< D.L.	< D.L.	0.12	< D.L.	< D.L.	< D.L.	< D.L.	0.68	203.80	12.18
Ce ppm	13.19	3.13	1.81	2.03	1.98	1.20	5.26	1.38	3.77	3.17	0.20	1.35
Co ppm	30.87	31.10	36.76	206.20	151.30	82.21	71.51	61.76	71.78	49.51	280.50	60.67
Cr ppm	308.50	349.30	293.70	590.40	525.60	303.30	1826.00	1895.00	2070.00	934.30	3319.00	1214.00
Cs ppm	< D.L.	< D.L.	< D.L.	< D.L.	< D.L.	< D.L.	< D.L.	< D.L.	< D.L.	< D.L.	< D.L.	< D.L.
Cu ppm	66.84	11.68	87.36	564.10	697.30	19.05	874.20	450.80	1540.00	504.20	1609.00	605.20
Dy ppm	4.72	2.55	0.48	0.79	0.75	0.30	1.40	0.44	1.38	1.68	0.11	0.92
Er ppm	2.89	1.65	0.26	0.47	0.45	0.21	0.80	0.27	0.81	1.05	0.07	0.59
Eu ppm	1.09	0.48	0.12	0.14	0.13	0.04	0.23	0.18	0.19	0.10	0.02	0.05
Ga ppm	13.96	11.95	3.46	5.99	5.77	3.93	8.09	4.23	8.36	11.42	5.84	7.08
Gd ppm	3.93	1.88	0.43	0.63	0.60	0.25	1.21	0.38	1.12	1.32	0.09	0.75
Ge ppm	1.85	0.75	0.50	0.43	0.40	0.28	1.57	1.64	1.95	0.61	5.09	0.74
Hf ppm	2.45	0.97	0.27	0.48	0.45	0.28	0.75	0.22	0.68	0.75	< D.L.	0.39
Ho ppm	1.05	0.59	0.10	0.18	0.16	0.07	0.31	0.10	0.30	0.39	0.02	0.22
In ppm	< D.L.	< D.L.	< D.L.	< D.L.	< D.L.	< D.L.	0.11	< D.L.	0.18	< D.L.	< D.L.	< D.L.
La ppm	5.40	0.99	0.80	0.83	0.83	0.44	2.26	0.61	1.55	1.33	< D.L.	0.55
Lu ppm	0.43	0.25	0.04	0.07	0.07	0.04	0.12	0.04	0.12	0.15	0.01	0.09
Mo ppm	< D.L.	< D.L.	5.58	12.11	8.58	1.43	< D.L.	< D.L.	< D.L.	1.39	184.30	14.06

Nb	ppm	6.84	0.57	1.08	1.46	1.47	0.89	3.90	0.88	2.96	2.07	< D.L.	1.16
Nd	ppm	10.30	3.43	1.28	1.60	1.52	0.89	3.45	1.01	2.69	2.59	0.21	1.20
Ni	ppm	112.80	126.40	140.40	492.70	385.90	190.70	1080.00	1180.00	1064.00	429.50	1609.00	710.70
Pb	ppm	0.90	< D.L.	< D.L.	1.23	1.17	1.08	< D.L.	< D.L.	< D.L.	< D.L.	2.24	1.22
Pr	ppm	2.05	0.58	0.26	0.31	0.29	0.18	0.75	0.21	0.56	0.49	0.04	0.20
Rb	ppm	0.79	< D.L.	< D.L.	< D.L.	< D.L.	< D.L.	< D.L.					
Sc	ppm	38.58	32.40	5.40	8.67	8.67	5.12	15.97	9.30	16.01	22.31	9.47	12.85
Sb	ppm	< D.L.	< D.L.	< D.L.	< D.L.	0.25	< D.L.						
Sm	ppm	3.30	1.36	0.37	0.51	0.50	0.28	1.03	0.31	0.90	0.95	0.10	0.50
Sn	ppm	1.55	0.64	3.80	0.48	0.52	9.66	< D.L.	< D.L.	0.54	0.79	0.83	1.09
Sr	ppm	145.50	32.01	< D.L.	4.17	< D.L.	3.86	5.94	4.84	6.93	9.61	4.48	6.18
Ta	ppm	0.52	0.05	0.09	0.11	0.11	0.07	0.28	0.06	0.21	0.16	< D.L.	0.08
Tb	ppm	0.69	0.35	0.07	0.11	0.11	0.04	0.21	0.06	0.20	0.24	0.02	0.14
Th	ppm	0.55	< D.L.	< D.L.	0.12	0.11	0.07	0.29	0.07	0.23	0.16	< D.L.	0.08
Tm	ppm	0.41	0.24	0.04	0.07	0.06	0.03	0.12	0.04	0.12	0.15	0.01	0.08
U	ppm	0.19	< D.L.	0.07	0.07	0.06	0.05	0.13	0.07	0.15	0.14	0.45	0.14
V	ppm	266.50	180.50	35.06	58.83	54.12	34.71	99.12	49.06	99.92	115.90	42.02	68.29
W	ppm	0.32	< D.L.	0.72	< D.L.	< D.L.	0.55	0.32	< D.L.	0.41	1.28	< D.L.	1.21
Y	ppm	26.89	14.83	2.43	4.39	4.12	1.91	7.95	2.65	7.71	10.34	0.61	5.87
Yb	ppm	2.80	1.63	0.23	0.45	0.43	0.24	0.79	0.28	0.80	1.01	0.08	0.57
Zn	ppm	60.02	105.60	45.73	56.51	64.18	33.78	139.50	115.00	161.80	237.90	2947.00	379.70
Zr	ppm	84.25	29.36	10.77	17.07	16.19	10.14	27.35	7.70	24.15	24.61	< D.L.	14.00

1605 <D.L.: lower than detection limit. Qz: quartz. Highly/moderately Si: highly/moderately silicified

1606

1607

1608

Sample	218a	218a	218a	218a	218a	218a	218a	218a	218a	218a	218a	218a	218a	218a	218a	218a	218a	218a	218a	218a	218a	218a	218a	
Clast vs matrix	Clast	Clast	Clast	Clast	Clast	Clast	Clast	Clast	Clast	Clast	Clast	Clast	Clast	Clast	Clast	Clast	Clast	Clast	Clast	Clast	Clast	Clast	Clast	Clast
Analysis #	22	29	30	13 / 1	14 / 1	18 / 1	19 / 1	20 / 1	21 / 1	23 / 1	26 / 1	27 / 1	33 / 1	39 / 1	41 / 1	43 / 1	49 / 1	56 / 1	57 / 1	58 / 1	59 / 1	60 / 1	61 / 1	
Zone analysed	C2	C6	C6	C-3	C-4	C-4	C-4	C-4	C-4	C-4	C-5	C-6	C-6	C-6	C-7	C-7								
Chlorite composition ^a																								
SiO ₂	27.59	30.42	27.21	29.33	28.53	27.11	27.18	28.94	25.64	26.69	29.01	28.37	29.10	28.70	27.66	28.07	28.88	29.91	30.98	29.13	28.05	27.65	28.23	
TiO ₂	0.03	0.02	0.03	0.00	0.08	0.06	0.11	0.06	0.04	0.06	0.00	0.08	0.00	0.34	0.04	0.11	0.03	0.03	0.04	0.01	0.07	0.06	0.09	
Al ₂ O ₃	19.06	19.76	19.12	17.56	17.23	19.43	18.92	18.86	19.64	19.08	19.64	19.59	17.66	18.09	18.48	18.21	17.55	17.48	15.91	18.13	19.30	19.37	19.31	
Cr ₂ O ₃	0.03	0.04	0.05	0.07	0.07	0.08	0.19	0.00	0.04	0.12	0.04	0.08	0.17	0.05	0.17	0.12	0.16	0.66	0.64	0.35	0.09	0.05	0.01	
FeO	23.76	9.81	24.59	23.27	23.60	25.89	23.53	18.33	28.21	26.53	18.58	17.75	22.42	20.09	21.23	21.92	18.37	17.41	14.20	14.87	18.70	19.11	18.76	
MnO	0.42	0.25	0.47	0.58	0.45	0.51	0.59	0.73	0.37	0.50	0.21	0.18	0.44	0.57	0.35	0.54	0.30	0.01	0.06	0.11	0.23	0.07	0.20	
MgO	17.14	27.78	16.45	16.29	16.29	13.86	15.44	21.24	12.65	13.98	20.59	21.11	17.87	17.73	18.06	16.77	21.61	21.13	25.20	23.31	19.73	20.50	20.66	
NiO	0.01	0.10	0.00	0.00	0.11	0.00	0.02	0.04	0.09	0.00	0.00	0.08	0.05	0.06	0.06	0.11	0.08	0.23	0.26	0.23	0.02	0.05	0.00	
CaO	0.13	0.03	0.09	0.23	0.24	0.15	0.26	0.07	0.05	0.11	0.04	0.11	0.17	0.46	0.15	0.23	0.09	0.07	0.01	0.02	0.19	0.03	0.03	
Na ₂ O	0.04	0.02	0.03	0.00	0.02	0.04	0.01	0.00	0.05	0.02	0.01	0.00	0.02	0.01	0.03	0.00	0.03	0.00	0.00	0.00	0.06	0.03	0.01	
K ₂ O	0.01	0.02	0.01	0.03	0.02	0.01	0.01	0.02	0.03	0.00	0.00	0.00	0.01	0.01	0.00	0.04	0.01	0.00	0.00	0.04	0.05	0.02	0.01	
total	88.23	88.23	88.06	87.37	86.64	87.14	86.26	88.29	86.82	87.10	88.10	87.34	87.92	86.10	86.24	86.13	87.11	86.94	87.33	86.21	86.48	86.93	87.31	
K ₂ O+Na ₂ O+CaO	0.18	0.07	0.14	0.26	0.28	0.20	0.28	0.09	0.13	0.13	0.05	0.11	0.20	0.48	0.18	0.27	0.13	0.08	0.02	0.06	0.29	0.08	0.05	
Structural formula ^b																								
Si	2.86	2.92	2.84	3.06	3.01	2.88	2.89	2.91	2.78	2.85	2.92	2.87	3.00	2.99	2.90	2.96	2.95	3.04	3.08	2.95	2.89	2.84	2.88	
Ti	0.00	0.00	0.00	0.00	0.01	0.01	0.01	0.00	0.00	0.00	0.00	0.01	0.00	0.03	0.00	0.01	0.00	0.00	0.00	0.00	0.01	0.00	0.01	
Al	2.33	2.24	2.36	2.16	2.15	2.43	2.37	2.24	2.51	2.40	2.33	2.34	2.15	2.22	2.28	2.26	2.11	2.09	1.87	2.16	2.34	2.34	2.32	
Al ^{IV}	1.14	1.08	1.16	0.94	0.99	1.12	1.11	1.09	1.22	1.15	1.08	1.13	1.00	1.01	1.10	1.04	1.05	0.96	0.92	1.05	1.11	1.16	1.12	
Al ^{VI}	1.19	1.16	1.20	1.21	1.16	1.32	1.26	1.15	1.29	1.26	1.24	1.21	1.15	1.22	1.19	1.22	1.06	1.13	0.95	1.11	1.23	1.18	1.19	
Cr	0.00	0.00	0.00	0.01	0.01	0.01	0.02	0.00	0.00	0.01	0.00	0.01	0.01	0.00	0.01	0.01	0.01	0.05	0.05	0.03	0.01	0.00	0.00	
Fe	2.06	0.79	2.15	2.03	2.09	2.30	2.09	1.54	2.56	2.37	1.56	1.50	1.94	1.75	1.86	1.93	1.57	1.48	1.18	1.26	1.61	1.64	1.60	
Mn	0.04	0.02	0.04	0.05	0.04	0.05	0.05	0.06	0.03	0.04	0.02	0.02	0.04	0.05	0.03	0.05	0.03	0.00	0.01	0.01	0.02	0.01	0.02	
Mg	2.65	3.98	2.56	2.53	2.57	2.20	2.45	3.19	2.05	2.23	3.09	3.19	2.75	2.76	2.82	2.64	3.29	3.20	3.74	3.52	3.03	3.14	3.14	
Ni	0.00	0.01	0.00	0.00	0.01	0.00	0.00	0.00	0.01	0.00	0.00	0.01	0.00	0.01	0.01	0.01	0.01	0.02	0.02	0.02	0.00	0.00	0.00	
Ca	0.01	0.00	0.01	0.03	0.03	0.02	0.03	0.01	0.01	0.01	0.00	0.01	0.02	0.05	0.02	0.03	0.01	0.01	0.00	0.02	0.02	0.00	0.00	
Na	0.01	0.00	0.01	0.00	0.00	0.01	0.00	0.00	0.01	0.00	0.00	0.00	0.00	0.00	0.01	0.00	0.01	0.00	0.00	0.00	0.01	0.01	0.00	
K	0.00	0.00	0.00	0.00	0.00	0.00	0.00	0.00	0.00	0.00	0.00	0.00	0.00	0.00	0.00	0.01	0.00	0.00	0.00	0.01	0.01	0.00	0.00	
octahedral sum	5.97	5.96	5.98	5.86	5.90	5.89	5.90	5.96	5.96	5.93	5.92	5.94	5.92	5.84	5.95	5.89	5.99	5.89	5.95	5.96	5.94	5.98	5.95	
vacancies	0.03	0.04	0.02	0.14	0.10	0.11	0.10	0.04	0.04	0.07	0.08	0.06	0.08	0.16	0.05	0.11	0.01	0.11	0.05	0.04	0.06	0.02	0.05	
Mg# ^c	0.56	0.83	0.54	0.56	0.55	0.49	0.54	0.67	0.44	0.48	0.66	0.68	0.59	0.61	0.60	0.58	0.68	0.68	0.76	0.74	0.65	0.66	0.66	
R ²⁺ ^d	4.75	4.79	4.75	4.61	4.70	4.54	4.59	4.80	4.65	4.65	4.67	4.71	4.73	4.57	4.72	4.63	4.89	4.70	4.95	4.81	4.66	4.79	4.75	
Calculated T (°C)																								
Bourdelle et al. (2013) ^e	445	362	500	194	234	247	263	388	407	313	271	336	251	203	330	233	585	211	302	330	304	630	379	
T _{corrected} (>350°C) ^e	351	319	369					330	337								391					402	326	

1620

1621

Sample	218a	218a	218a	218a	218a	218a	218a	218a	218a	218a	218a	218a	218a
Clast vs matrix	Clast	Clast	Clast	Clast	Mat	Mat	Mat	Mat	Mat	Mat	Mat	Mat	Mat
Analysis #	62 / 1	63 / 1	64 / 1	65 / 1	9 / 1	10 / 1	11 / 1	44 / 1	45 / 1	46 / 1	47 / 1	50 / 1	69 / 1
Chlorite composition ^a													
SiO ₂	28.23	29.35	27.75	28.58	28.20	30.04	28.31	27.60	28.93	28.98	28.65	30.16	29.44
TiO ₂	0.01	0.08	0.04	0.04	0.00	0.03	0.00	0.04	0.00	0.09	0.03	0.00	0.03
Al ₂ O ₃	19.86	18.85	20.29	20.27	18.42	17.92	17.90	18.64	18.47	19.06	19.56	18.66	18.49
Cr ₂ O ₃	0.00	0.01	0.02	0.11	0.27	0.67	0.08	0.11	0.03	0.04	0.26	0.17	0.03
FeO	17.36	17.43	18.52	18.22	22.93	22.55	21.15	23.60	19.10	14.22	18.97	17.54	14.29
MnO	0.16	0.17	0.15	0.21	0.38	0.40	0.36	0.43	0.25	0.28	0.26	0.26	0.11
MgO	21.71	21.00	20.83	19.95	18.08	15.79	18.24	16.47	20.11	23.98	19.42	20.42	23.76
NiO	0.02	0.07	0.16	0.06	0.10	0.04	0.16	0.04	0.25	0.10	0.11	0.02	0.28
CaO	0.00	0.11	0.03	0.06	0.05	0.28	0.10	0.15	0.00	0.07	0.11	0.06	0.06
Na ₂ O	0.00	0.01	0.01	0.00	0.00	0.05	0.08	0.03	0.00	0.02	0.08	0.05	0.00
K ₂ O	0.00	0.00	0.02	0.02	0.00	0.08	0.00	0.00	0.00	0.03	0.03	0.03	0.01
total	87.35	87.08	87.82	87.52	88.42	87.85	86.38	87.11	87.13	86.87	87.50	87.37	86.49
K ₂ O+Na ₂ O+CaO	0.00	0.11	0.05	0.09	0.05	0.40	0.18	0.18	0.00	0.12	0.23	0.13	0.07
Structural formula ^b													
Si	2.85	2.97	2.81	2.89	2.91	3.10	2.96	2.90	2.96	2.90	2.92	3.04	2.96
Ti	0.00	0.01	0.00	0.00	0.00	0.00	0.00	0.00	0.00	0.01	0.00	0.00	0.00
Al	2.36	2.25	2.42	2.42	2.24	2.18	2.21	2.31	2.23	2.25	2.35	2.22	2.19
Al ^{IV}	1.15	1.03	1.19	1.11	1.09	0.90	1.04	1.10	1.04	1.10	1.08	0.96	1.04
Al ^{VI}	1.21	1.22	1.23	1.31	1.14	1.28	1.17	1.21	1.18	1.15	1.26	1.25	1.14
Cr	0.00	0.00	0.00	0.01	0.02	0.05	0.01	0.01	0.00	0.00	0.02	0.01	0.00
Fe	1.47	1.48	1.57	1.54	1.98	1.94	1.85	2.07	1.63	1.19	1.61	1.48	1.20
Mn	0.01	0.01	0.01	0.02	0.03	0.03	0.03	0.04	0.02	0.02	0.02	0.02	0.01
Mg	3.27	3.17	3.14	3.01	2.78	2.43	2.84	2.58	3.07	3.58	2.95	3.07	3.56
Ni	0.00	0.01	0.01	0.00	0.01	0.00	0.01	0.00	0.02	0.01	0.01	0.00	0.02
Ca	0.00	0.01	0.00	0.01	0.01	0.03	0.01	0.02	0.00	0.01	0.01	0.01	0.01
Na	0.00	0.00	0.00	0.00	0.00	0.01	0.02	0.01	0.00	0.00	0.02	0.01	0.00
K	0.00	0.00	0.00	0.00	0.00	0.01	0.00	0.00	0.00	0.00	0.00	0.00	0.00
octahedral sum	5.97	5.90	5.98	5.89	5.96	5.79	5.94	5.94	5.93	5.97	5.91	5.85	5.94
vacancies	0.03	0.10	0.02	0.11	0.04	0.21	0.06	0.06	0.07	0.03	0.09	0.15	0.06
Mg# ^c	0.69	0.68	0.67	0.66	0.58	0.56	0.61	0.55	0.65	0.75	0.65	0.67	0.75
R ²⁺ ^d	4.75	4.66	4.74	4.57	4.79	4.41	4.74	4.70	4.74	4.80	4.59	4.57	4.79
Calculated T (°C)													
Bourdelle et al. (2013) ^e	422	236	494	245	393	152	284	309	267	415	246	188	300
Tcorrected (>350°C) ^e	343		367		332					340			

1622

1623

Sample	218c	218c	218c	218c	218c	218c	218c	218c	218c	218c	218c	218c	218c	218c	218c	218c	218c	218c	218c	218c	218c	218c	218c	
Clast vs matrix	Clast	Clast	Clast	Clast	Clast	Clast	Clast	Clast	Clast	Clast	Clast	Clast	Clast	Clast	Clast	Clast	Clast	Clast	Clast	Clast	Clast	Clast	Clast	Clast
Analysis #	33 / 1	38 / 1	39 / 1	40 / 1	41 / 1	42 / 1	101 /	102 /	103 /	103 /	103 /	103 /	103 /	103 /	103 /	103 /	103 /	103 /	103 /	103 /	103 /	103 /	104 /	
Chlorite composition ^a																								
SiO ₂	28.75	28.61	28.38	28.00	28.29	28.44	27.80	28.02	27.66	27.81	28.39	28.56	27.99	28.37	28.54	28.60	28.45	27.75	28.02	28.96	28.54	30.11		
TiO ₂	0.14	0.02	0.03	0.67	0.05	0.08	0.04	0.04	0.03	0.00	0.06	0.03	0.07	0.10	0.06	0.14	0.06	0.09	0.17	0.39	0.08	0.02		
Al ₂ O ₃	18.97	18.75	19.48	19.58	19.71	19.08	19.25	18.25	19.14	19.10	19.93	18.93	19.01	19.32	19.88	19.38	19.07	19.85	19.33	19.66	19.59	18.50		
Cr ₂ O ₃	0.41	0.01	0.00	0.02	0.03	0.03	0.33	0.19	0.29	0.18	0.11	0.13	0.00	0.08	0.00	0.04	0.04	0.17	0.00	0.10	0.09	0.12		
FeO	19.01	18.52	17.89	16.44	17.60	19.25	20.10	20.73	19.67	18.92	18.31	19.41	19.11	19.49	19.89	19.64	20.55	18.36	19.79	19.49	20.95	13.56		
MnO	0.22	0.26	0.27	0.17	0.26	0.21	0.27	0.31	0.28	0.31	0.28	0.22	0.22	0.30	0.35	0.27	0.18	0.17	0.21	0.26	0.34	0.28		
MgO	20.59	20.17	21.41	22.15	21.14	19.97	19.22	19.21	18.95	19.65	19.58	19.23	19.61	18.82	19.43	19.90	18.89	20.27	18.44	19.42	18.63	24.56		
NiO	0.17	0.07	0.12	0.06	0.08	0.13	0.09	0.04	0.11	0.13	0.05	0.03	0.09	0.00	0.00	0.16	0.09	0.05	0.05	0.08	0.07	0.14		
CaO	0.13	0.05	0.04	0.05	0.06	0.07	0.06	0.05	0.05	0.06	0.09	0.09	0.08	0.06	0.09	0.12	0.10	0.09	0.20	0.25	0.11	0.05		
Na ₂ O	0.02	0.04	0.00	0.01	0.04	0.02	0.09	0.02	0.03	0.04	0.00	0.04	0.00	0.05	0.00	0.00	0.00	0.00	0.05	0.05	0.03	0.03		
K ₂ O	0.01	0.00	0.02	0.01	0.00	0.02	0.00	0.00	0.02	0.01	0.02	0.00	0.02	0.05	0.01	0.02	0.00	0.00	0.00	0.01	0.02	0.00		
total	88.41	86.49	87.62	87.16	87.26	87.28	87.24	86.87	86.22	86.20	86.82	86.67	86.22	86.65	88.23	88.26	87.43	86.79	86.26	88.67	88.46	87.36		
K ₂ O+Na ₂ O+CaO	0.16	0.09	0.05	0.07	0.10	0.10	0.15	0.08	0.10	0.11	0.11	0.13	0.11	0.16	0.10	0.14	0.10	0.09	0.25	0.30	0.17	0.07		
Structural formula ^b																								
Si	2.90	2.94	2.87	2.83	2.87	2.91	2.86	2.91	2.88	2.88	2.90	2.94	2.90	2.92	2.89	2.90	2.92	2.84	2.91	2.91	2.90	2.98		
Ti	0.01	0.00	0.00	0.05	0.00	0.01	0.00	0.00	0.00	0.00	0.00	0.00	0.01	0.01	0.00	0.01	0.00	0.01	0.01	0.03	0.01	0.00		
Al	2.25	2.27	2.32	2.33	2.35	2.30	2.34	2.23	2.35	2.33	2.40	2.30	2.32	2.35	2.37	2.31	2.31	2.40	2.36	2.33	2.35	2.16		
Al ^{IV}	1.10	1.06	1.13	1.17	1.13	1.09	1.14	1.09	1.12	1.12	1.10	1.06	1.10	1.08	1.11	1.10	1.08	1.16	1.09	1.09	1.10	1.02		
Al ^{VI}	1.15	1.21	1.19	1.16	1.22	1.20	1.20	1.14	1.22	1.21	1.30	1.24	1.22	1.27	1.26	1.21	1.23	1.24	1.27	1.24	1.25	1.14		
Cr	0.03	0.00	0.00	0.00	0.00	0.00	0.03	0.02	0.02	0.01	0.01	0.01	0.00	0.01	0.00	0.00	0.00	0.01	0.00	0.01	0.01	0.01		
Fe	1.60	1.59	1.51	1.39	1.49	1.64	1.73	1.80	1.71	1.64	1.56	1.67	1.65	1.68	1.68	1.66	1.76	1.57	1.72	1.64	1.78	1.12		
Mn	0.02	0.02	0.02	0.01	0.02	0.02	0.02	0.03	0.02	0.03	0.02	0.02	0.02	0.03	0.03	0.02	0.02	0.01	0.02	0.02	0.03	0.02		
Mg	3.10	3.09	3.23	3.33	3.19	3.04	2.95	2.97	2.94	3.03	2.98	2.95	3.02	2.89	2.93	3.00	2.89	3.09	2.85	2.91	2.82	3.62		
Ni	0.01	0.01	0.01	0.00	0.01	0.01	0.01	0.00	0.01	0.01	0.01	0.00	0.01	0.00	0.00	0.01	0.01	0.00	0.00	0.01	0.01	0.01		
Ca	0.01	0.01	0.00	0.01	0.01	0.01	0.01	0.01	0.01	0.01	0.01	0.01	0.01	0.01	0.01	0.01	0.01	0.01	0.02	0.03	0.01	0.00		
Na	0.00	0.01	0.00	0.00	0.01	0.00	0.02	0.00	0.01	0.01	0.00	0.01	0.00	0.01	0.00	0.00	0.00	0.01	0.01	0.01	0.01	0.01		
K	0.00	0.00	0.00	0.00	0.00	0.00	0.00	0.00	0.00	0.00	0.00	0.00	0.00	0.01	0.00	0.00	0.00	0.00	0.00	0.00	0.00	0.00		
octahedral sum	5.94	5.93	5.97	5.91	5.95	5.93	5.96	5.97	5.94	5.95	5.89	5.91	5.93	5.89	5.92	5.93	5.92	5.94	5.89	5.87	5.91	5.94		
vacancies	0.06	0.07	0.03	0.09	0.05	0.07	0.04	0.03	0.06	0.05	0.11	0.09	0.07	0.11	0.08	0.07	0.08	0.06	0.11	0.13	0.09	0.06		
Mg# ^c	0.66	0.66	0.68	0.71	0.68	0.65	0.63	0.62	0.63	0.65	0.66	0.64	0.65	0.63	0.64	0.64	0.62	0.66	0.62	0.64	0.61	0.76		
R ²⁺ ^d	4.73	4.71	4.77	4.74	4.71	4.72	4.71	4.80	4.68	4.71	4.57	4.64	4.71	4.60	4.65	4.70	4.68	4.68	4.59	4.58	4.64	4.78		
Calculated T (°C)																								
Bourdelle et al. (2013) ^e	322	278	418	373	351	303	371	410	313	334	242	250	305	242	280	299	270	349	248	234	269	285		
Tcorrected (>350°C) ^e			341	323	314		323	338																

1624

1625

1626

1627

1628

Sample	155	155	155	155	155	155	155	155	155	155	155	155	155	155	155	155	155	155	115	115	115
Clast vs matrix	Clast	Clast	Clast	Clast	Clast	Clast	Mat	clast	clast	clast											
Analysis #	83 / 1	87 / 1	89 / 1	92 / 1	93 / 1	94 / 1	78 / 1	80 / 1	89 / 1	56 / 1	59 / 1	60 / 1	61 / 1	73 / 1	74 / 1	78 / 1	79 / 1	25 / 1	28 / 1	33 / 1	
Chlorite composition ^a																					
SiO ₂	30.66	28.34	28.78	26.99	26.58	27.52	27.14	27.31	28.80	29.88	27.78	26.30	28.12	26.37	26.72	26.72	26.64	28.14	31.06	30.62	
TiO ₂	0.05	0.08	0.06	0.00	0.07	0.02	0.00	0.00	0.10	0.07	0.04	0.03	0.10	0.02	0.00	0.19	0.06	0.04	0.00	0.00	
Al ₂ O ₃	19.94	20.83	19.88	19.73	20.45	19.92	20.08	19.97	18.05	17.19	19.13	19.38	19.46	20.03	20.13	20.48	20.67	19.12	16.18	15.94	
Cr ₂ O ₃	0.50	0.00	0.00	0.20	0.04	0.06	0.18	0.04	0.02	0.61	0.00	0.00	0.00	0.07	0.02	0.07	0.04	0.05	0.00	0.08	
FeO	21.27	17.35	15.81	23.87	26.12	22.39	24.36	22.95	23.72	21.24	25.96	27.42	24.31	28.69	28.29	24.56	26.33	17.71	17.14	16.92	
MnO	0.33	0.15	0.12	0.14	0.25	0.21	0.31	0.26	0.20	0.43	0.14	0.20	0.16	0.14	0.21	0.22	0.25	0.23	0.25	0.11	
MgO	14.43	20.71	22.77	15.71	15.33	17.69	15.54	16.93	17.11	16.92	14.25	14.09	14.37	12.71	13.27	14.93	13.45	21.41	22.53	22.31	
NiO	0.06	0.04	0.03	0.00	0.00	0.12	0.02	0.02	0.00	0.12	0.07	0.00	0.04	0.03	0.05	0.01	0.08	0.09	0.10	0.06	
CaO	0.26	0.05	0.08	0.07	0.05	0.03	0.07	0.05	0.11	0.15	0.08	0.04	0.10	0.06	0.08	0.03	0.04	0.12	0.32	0.38	
Na ₂ O	0.05	0.04	0.02	0.06	0.04	0.06	0.09	0.06	0.08	0.12	0.04	0.06	0.09	0.05	0.08	0.04	0.01	0.03	0.06	0.06	
K ₂ O	0.04	0.02	0.00	0.01	0.01	0.00	0.05	0.04	0.02	0.03	0.03	0.04	0.09	0.02	0.01	0.01	0.01	0.02	0.03	0.05	
total	87.59	87.62	87.55	86.79	88.95	88.01	87.85	87.62	88.22	86.76	87.52	87.54	86.84	88.19	88.86	87.27	87.59	86.97	87.71	86.54	
K ₂ O+Na ₂ O+CaO	0.36	0.12	0.10	0.15	0.10	0.09	0.21	0.14	0.22	0.30	0.14	0.13	0.27	0.13	0.17	0.08	0.07	0.18	0.44	0.49	
Structural formula ^b																					
Si	3.13	2.85	2.87	2.85	2.77	2.84	2.84	2.84	2.98	3.11	2.93	2.81	2.96	2.81	2.82	2.81	2.82	2.87	3.12	3.12	
Ti	0.00	0.01	0.00	0.00	0.01	0.00	0.00	0.00	0.01	0.01	0.00	0.00	0.01	0.00	0.00	0.02	0.01	0.00	0.00	0.00	
Al	2.40	2.47	2.34	2.45	2.51	2.42	2.47	2.45	2.20	2.10	2.38	2.44	2.42	2.51	2.50	2.54	2.58	2.30	1.92	1.91	
Al ^{IV}	0.87	1.15	1.13	1.15	1.23	1.16	1.16	1.16	1.02	0.89	1.07	1.19	1.04	1.19	1.18	1.19	1.18	1.13	0.88	0.88	
Al ^{VI}	1.53	1.32	1.21	1.30	1.28	1.26	1.31	1.28	1.18	1.21	1.31	1.25	1.38	1.32	1.31	1.35	1.39	1.16	1.04	1.03	
Cr	0.04	0.00	0.00	0.02	0.00	0.01	0.01	0.00	0.00	0.05	0.00	0.00	0.00	0.01	0.00	0.01	0.00	0.00	0.00	0.01	
Fe	1.81	1.46	1.32	2.11	2.27	1.93	2.13	1.99	2.05	1.85	2.29	2.45	2.14	2.55	2.49	2.16	2.33	1.51	1.44	1.44	
Mn	0.03	0.01	0.01	0.01	0.02	0.02	0.03	0.02	0.02	0.04	0.01	0.02	0.01	0.01	0.02	0.02	0.02	0.02	0.02	0.01	
Mg	2.19	3.10	3.39	2.47	2.38	2.72	2.42	2.62	2.64	2.62	2.24	2.24	2.26	2.02	2.08	2.34	2.12	3.25	3.37	3.38	
Ni	0.00	0.00	0.00	0.00	0.00	0.01	0.00	0.00	0.00	0.01	0.01	0.00	0.00	0.00	0.00	0.00	0.01	0.01	0.01	0.01	
Ca	0.03	0.01	0.01	0.01	0.01	0.00	0.01	0.01	0.01	0.02	0.01	0.00	0.01	0.01	0.01	0.00	0.00	0.01	0.03	0.04	
Na	0.01	0.01	0.00	0.01	0.01	0.01	0.02	0.01	0.02	0.02	0.01	0.01	0.02	0.01	0.02	0.01	0.00	0.01	0.01	0.01	
K	0.01	0.00	0.00	0.00	0.00	0.00	0.01	0.01	0.00	0.00	0.00	0.01	0.01	0.00	0.00	0.00	0.00	0.00	0.01	0.01	
octahedral sum	5.65	5.91	5.95	5.93	5.97	5.95	5.93	5.95	5.92	5.82	5.88	5.98	5.83	5.93	5.94	5.89	5.88	5.98	5.93	5.93	
vacancies	0.35	0.09	0.05	0.07	0.03	0.05	0.07	0.05	0.08	0.18	0.12	0.02	0.17	0.07	0.06	0.11	0.12	0.02	0.07	0.07	
Mg# ^c	0.55	0.68	0.72	0.54	0.51	0.58	0.53	0.57	0.56	0.59	0.49	0.48	0.51	0.44	0.46	0.52	0.48	0.68	0.70	0.70	
R ²⁺ ^d	4.04	4.58	4.72	4.59	4.67	4.68	4.58	4.64	4.71	4.51	4.55	4.71	4.41	4.59	4.60	4.52	4.48	4.79	4.84	4.84	
Calculated T (°C)																					
Bourdelle et al. (2013) ^e	116	307	352	306	509	360	312	335	259	175	223	490	186	321	326	272	251				
Tcorrected (>350°C) ^e			315		371	318						365									

1629

1632 **Table S3.** *In situ LA-ICP-MS trace element analysis (ppm) of 22 chlorite crystals from silicified samples.*

1633

Sample	195	195	195	195	155	155	155	155	155	155	155	218ab	218ab	218ab	218ab	218c	218c	218c	173	173	173
Clast vs matrix	clast	clast	clast	clast	clast	clast	matrix	matrix	clast	clast	matrix	clast	clast	matrix	matrix	clast	clast	matrix	matrix	matrix	matrix
Analysis #	Ch11	Ch12	Ch12-1	Ch13b	Ch11	Ch12	Ch13	Ch13-1	Ch14	Ch15	Ch16	Ch11	Ch12	Ch13	Ch14	Ch11	Ch12	Ch13	Ch11	Ch12	Ch13
Ti (47) ^a	47 ^b	5289	49	116	188	-	3816	384	144	110	218	248	13	29	28	66	215	bdl	23	25	17
Mn (55)	2837	2720	2383	1985	3340	2319	241	267	2734	2733	525	386	75	93	48	485	1725	45	278	317	281
Cr (53)	41	311	249	108	1022	689	124	92	40	55	231	169	30	69	56	44	746	15	720	1662	1107
Co (59)	34	33	33	40	103	72	bdl	bdl	150	146	36	bdl	bdl	bdl	bdl	30	93	bdl	166	69	84
Ni (60)	183	179	180	202	549	401	28	29	482	604	83	101	25	27	12	110	368	bdl	2639	1330	1689
Cu (63)	19	20	bdl	bdl	bdl	bdl	bdl	bdl	bdl	bdl	bdl	bdl	bdl	bdl	bdl	bdl	38	bdl	280	202	15
Zn (66)	207	172	159	152	225	161	16	14	198	180	40	29	bdl	bdl	bdl	25	108	bdl	1216	865	905
V (51)	172	241	156	134	473	405	45	18	209	164	35	39	bdl	bdl	bdl	66	198	bdl	29	29	26

1634 Analyses carried out at GeoRessources (Nancy, France) with a 193 nm GeoLas Pro ArF Excimer laser (Microlas, Göttingen, Germany) coupled with beam
 1635 homogenization optics. Analyzed with an Agilent 7500c Quadrupole ICP-MS (Agilent, Santa Clara, USA) equipped with an octopole reaction system with
 1636 enhanced sensitivity optional lenses (Cs type; Agilent). Internal standard: ²⁸Si, calibrated from the mean value of several chlorite microprobe analyses.

1637 ^a Element analyzed (isotope)

1638 ^b Concentrations in ppm calibrated against the NIST SRM 610 silica glass reference using values given in Pearce et al. (1997). Absolute concentrations (ppm)
 1639 calculated from equations in Longerich et al. (1996).

1640

1641

1642

1643

1644 **Table S4.** Temperature of chlorite formation calculated from composition (R^{2+} and Si) of chlorite in equilibrium with quartz, with the thermometer
 1645 of Bourdelle et al. (2013) for chlorites from matrix, clasts and both, in silicified samples.
 1646

T (°C) in matrix and clasts	195	155	218ab	218c	173
Mean T	250	265	291	294	276
Median T	244	273	303	301	257
Minimum T	156	113	152	234	140
Maximum T	350	492	402	349	452
Standard deviation	49	88	61	36	75
Number of analyses	46	40	36	22	14
T (°C) in matrix	195	155	218ab	218c	173
Mean T	244	275	269		287
Median T	236	272	284		234
Minimum T	156	175	152		223
Maximum T	350	365	340		452
Standard deviation	48	63	64		96
Number of analyses	37	11	9		5
T (°C) in clasts	195	155	218ab	218c	173
Mean T	272	262	298	294	270
Median T	269	273	313	301	258
Minimum T	197	113	194	234	140
Maximum T	332	492	402	349	361
Standard deviation	50	96	59	36	66
Number of analyses	9	29	27	22	9

1647